

**FOUNDATIONS OF TWO-POINT DOPPLER SONAR  
SIGNAL PROCESSING FOR RANGE-SPREAD TARGETS**

by

Stephen Kendall Pearce

B.S. Phys., Washington State University, 2006

THESIS SUBMITTED IN PARTIAL FULFILLMENT  
OF THE REQUIREMENTS FOR THE DEGREE OF

MASTER OF APPLIED SCIENCE

In the School  
of  
Engineering Science

© Stephen Kendall Pearce 2010  
SIMON FRASER UNIVERSITY  
Spring 2010

All rights reserved. However, in accordance with the *Copyright Act of Canada*, this work may be reproduced, without authorization, under the conditions for *Fair Dealing*. Therefore, limited reproduction of this work for the purposes of private study, research, criticism, review and news reporting is likely to be in accordance with the law, particularly if cited appropriately.

## APPROVAL

**Name:** Stephen Kendall Pearce  
**Degree:** Master of Applied Science  
**Title of thesis:** Foundations of Two-Point Doppler Sonar Signal Processing  
for Range-Spread Targets

**Examining Committee:** Dr. Ivan Bajic, Assistant Professor, Engineering Science  
Simon Fraser University  
Chair

---

Dr. John Bird, Professor, Engineering Science  
Simon Fraser University  
Senior Supervisor

---

Dr. Shawn Stapleton, Professor, Engineering Science  
Simon Fraser University  
Supervisor

---

Dr. Rodney Vaughan, Professor, Engineering Science  
Simon Fraser University  
SFU Examiner

**Date Approved:**

*April 8, 2010*

---



SIMON FRASER UNIVERSITY  
LIBRARY

## Declaration of Partial Copyright Licence

The author, whose copyright is declared on the title page of this work, has granted to Simon Fraser University the right to lend this thesis, project or extended essay to users of the Simon Fraser University Library, and to make partial or single copies only for such users or in response to a request from the library of any other university, or other educational institution, on its own behalf or for one of its users.

The author has further granted permission to Simon Fraser University to keep or make a digital copy for use in its circulating collection (currently available to the public at the "Institutional Repository" link of the SFU Library website <[www.lib.sfu.ca](http://www.lib.sfu.ca)> at: <<http://ir.lib.sfu.ca/handle/1892/112>>) and, without changing the content, to translate the thesis/project or extended essays, if technically possible, to any medium or format for the purpose of preservation of the digital work.

The author has further agreed that permission for multiple copying of this work for scholarly purposes may be granted by either the author or the Dean of Graduate Studies.

It is understood that copying or publication of this work for financial gain shall not be allowed without the author's written permission.

Permission for public performance, or limited permission for private scholarly use, of any multimedia materials forming part of this work, may have been granted by the author. This information may be found on the separately catalogued multimedia material and in the signed Partial Copyright Licence.

While licensing SFU to permit the above uses, the author retains copyright in the thesis, project or extended essays, including the right to change the work for subsequent purposes, including editing and publishing the work in whole or in part, and licensing other parties, as the author may desire.

The original Partial Copyright Licence attesting to these terms, and signed by this author, may be found in the original bound copy of this work, retained in the Simon Fraser University Archive.

Simon Fraser University Library  
Burnaby, BC, Canada

# Abstract

An important problem in sonar signal processing is the two-point estimation of the velocity of a range-spread target, such as the seafloor. This thesis provides a detailed mathematical foundation for the analysis of common velocity estimation methods, and supports this analysis through simulation and experimentation. A Gaussian model is assumed for both noise and signal, and covariance functions for range-spread targets are then derived. From these covariance functions, the Cramer-Rao lower bound is determined for the coherent estimation techniques, and a detailed discussion of how to minimize this bound is provided. Three-dimensional boat motion is seen to play a large role in determining the experimental performance of the estimators. The "micro-Doppler" method is introduced as a novel approach to underwater velocity estimation, facilitating both the estimation of small phase changes caused by micro velocities, and the detection of faster targets causing larger phase changes.

*To R. Wayne Meisinger*

*“Train up a fig-tree in the way it should go, and when you are old sit under the shade of it.”*

— *Charles Dickens*

# Acknowledgments

I would like to offer massive thanks to everyone who has helped me to complete the body of work which is contained herein.

First and foremost, I would like to thank my family - Chris, Chris, and Mike - for their endless love, support, and encouragement over the years.

My fellow researchers in the lab (Sabir, Julian, and Geoff) have also contributed heavily to my experience by not only helping me to learn relevant material, but also by helping me learn to "take it easy". Elaine contributed to this project by reading this thesis, and by suggesting corrections as appropriate. Much-needed financial support has been provided by Marport Canada, for which I am also grateful.

Finally, I would like to thank my supervisor, Dr. John Bird, for his continued patience throughout the entirety of my graduate studies at SFU. I am most grateful for his contributions to my professional development, and for his investment in me as a student.

# Contents

<b>Approval</b>	<b>ii</b>
<b>Abstract</b>	<b>iii</b>
<b>Dedication</b>	<b>iv</b>
<b>Quotation</b>	<b>v</b>
<b>Acknowledgments</b>	<b>vi</b>
<b>Contents</b>	<b>vii</b>
<b>List of Figures</b>	<b>x</b>
<b>1 Introduction</b>	<b>1</b>
1.1 Background . . . . .	4
1.1.1 Review of the URL Sonar System . . . . .	7
1.2 Velocity Estimation . . . . .	11
1.2.1 Introducing "Micro Doppler" . . . . .	14
1.3 Review of Current Literature and Contributions of the Thesis . . . . .	15
1.4 Thesis Organization . . . . .	17
<b>2 Theoretical Analysis</b>	<b>19</b>
2.1 Description of the Situation Which is to be Modeled . . . . .	20
2.2 Target Models . . . . .	24
2.2.1 Slowly Fluctuating Point Target . . . . .	25
2.2.2 Range-Spread Target . . . . .	32

2.3	Signal Models . . . . .	36
2.3.1	Monopulse Waveform . . . . .	38
2.3.2	Pulse Pair Waveform . . . . .	39
2.3.3	Noise . . . . .	44
2.3.4	Final Expressions for Covariance Functions . . . . .	47
2.4	Velocity Estimation Methods . . . . .	49
2.4.1	Monopulse Methods . . . . .	51
2.4.2	Pulse Pair Methods . . . . .	61
2.5	Performance Limitations . . . . .	64
2.5.1	Expressions for the Cramer-Rao Lower Bound . . . . .	64
2.5.2	Minimizing the Cramer-Rao Lower Bound . . . . .	67
2.5.3	Calculating the CRLB for the VEMs . . . . .	72
2.5.4	Estimator RMSE Compared to $\sqrt{CRLB_N}$ . . . . .	79
<b>3</b>	<b>Simulation</b>	<b>85</b>
3.1	Confirming Agreement With Theory . . . . .	86
3.1.1	Slowly Fluctuating Point Target . . . . .	86
3.1.2	Correlation Functions: Range-Spread Target . . . . .	95
3.2	Velocity Estimation . . . . .	100
3.2.1	Ping Pair Incoherent . . . . .	102
3.2.2	Single Ping Covariance . . . . .	103
3.2.3	Ping Pair Covariance . . . . .	108
3.2.4	Simulation and the VEM's: Concluding Remarks . . . . .	110
<b>4</b>	<b>Experimental Data</b>	<b>112</b>
4.1	Defining the Experiment . . . . .	112
4.2	Results . . . . .	113
4.2.1	Incoherent Processing . . . . .	114
4.2.2	Single Ping Covariance Processing . . . . .	114
4.2.3	Validation . . . . .	117
<b>5</b>	<b>Micro-Doppler</b>	<b>124</b>
5.1	Theory . . . . .	124
5.2	Experimentation . . . . .	127

5.3	Micro-Doppler: Summary . . . . .	130
<b>6</b>	<b>Conclusion</b>	<b>131</b>
6.1	Contributions of the Thesis . . . . .	131
6.2	Recommendations for Future Work . . . . .	133
<b>A</b>	<b>List of Symbols</b>	<b>134</b>
	<b>Bibliography</b>	<b>137</b>

# List of Figures

1.1	General block diagram of a sonar system. . . . .	3
1.2	Typical side-scan bathymetric boat-mounted sonar. . . . .	6
1.3	”Bird’s eye” view diagram of a typical URL transducer array. One transducer element is used for sound transmission, and another six elements are used for reception. . . . .	7
1.4	Narrow along-track beamwidth of URL transducer arrays. . . . .	9
1.5	Typical two-target scenario, with both targets existing at a common range. .	10
1.6	Forward-looking hull-mounted sonar system. . . . .	13
2.1	Transmit waveforms of interest to the URL: monopulse (top) and pulse pair (bottom). As pictured, the monopulse is 130 cycles of the carrier frequency in length. Each pulse in the pulse pair is 30 cycles in length with a separation between pulses of 35 cycles (of the carrier). . . . .	21
2.2	Basic model of sound transmission and reflection off of a point target. . . . .	22
2.3	Transmission of a monopulse by a forward-looking sonar system. . . . .	23
2.4	Transmission of a pulse pair by a forward-looking sonar system. . . . .	24
2.5	A rectangular function (top) is convolved with itself to yield a triangular function (bottom). The <i>rect</i> function is 130 time units wide, and is offset from symmetry about the y-axis by 20 time units. The corresponding <i>tri</i> function is 260 time units wide, and is offset from symmetry about the y-axis by 40 time units. . . . .	37

2.6	A pulse pair (top) centered about the y-axis is convolved with itself to yield a three-peaked triangular structure (bottom). The un-normalized <i>rect</i> functions composing the pulse pair are each 30 time units wide, and each of the corresponding <i>tri</i> functions are 60 time units wide, and are also centered about the y-axis. . . . .	43
2.7	The various velocity estimation methods (VEMs) which are under consideration in this thesis. . . . .	50
2.8	Incoherent cross covariance of two waveforms. The first waveform (top) is a random series of numbers (the signal) buried in additive noise, while the second waveform (middle) contains a shifted version of the first signal (shifted by 500 samples) plus five hundred new random samples (also buried in additive noise). The bottom graph represents the covariance of these two waveforms, with the peak at a value of $\approx 0.63$ , occurring at a lag of $k = 500$ . . . . .	53
2.9	Plot of the square root of the Cramer-Rao lower bound for phase angle estimates as a function of the lag $k$ which is used in estimation. Signal-to-thermal noise ratio $SNR_n$ is varied from 45 dB (bottom curve) to -5 dB (top curve), and $N = 5$ snapshots are used. A 150-cycle monopulse has been assumed, which causes $\sqrt{CRLB(\gamma)}$ to tend towards infinity when $k = 150$ . . . . .	68
2.10	Plot of the square root of the Cramer-Rao lower bound for velocity estimates as a function of the lag $k$ which is used in estimation. Signal-to-thermal noise ratio $SNR_n$ is varied from 45 dB (bottom curve) to -5 dB (top curve), and five snapshots are used. A 150-cycle monopulse has been assumed. . . . .	69
2.11	Plot of the square-root of the Cramer-Rao lower bound for velocity estimates as a function of the length of the time series (the number of samples) which is used for processing. The red curve represents the CRLB which is attained if the time series is used as a single long observation (in our case, a long pulse), and all subsequent curves represent the CRLB which is attained if the time series is divided into a smaller number of independent snapshots. . . . .	71

2.12	Plot of the square root of the 10-snapshot Cramer-Rao lower bound for ping pair covariance velocity estimates as a function of the $SNR_n$ when $T_p = .25$ s. Signal-to-thermal noise ratio $SNR_n$ is varied from 10 dB to 40 dB. A 130-cycle monopulse has been assumed, and $SNR_c = 24$ dB corresponding to the lowest value which we expect it to equal for this VEM (as limited by the maximum unambiguous target velocity) at this $T_p$ . . . . .	73
2.13	Plot of the square root of the Cramer-Rao lower bound for single ping covariance velocity estimates as a function of the $SNR_n$ for $N = 10$ snapshots. Signal-to-thermal noise ratio $SNR_n$ is varied from 10 dB to 40 dB. $SNR_c \approx 0$ dB as defined by the lag $k = 65$ used in estimation. . . . .	75
2.14	Plot of the square root of the Cramer-Rao lower bound for pulse pair covariance velocity estimates as a function of the $SNR_{n,wf}$ for two types of filtering. The top curve represents the bound on the estimator's RMSE which is attained if a wide frequency-domain filter is used, where the width of the filter is equal to $BW = 4f_c/k_p$ - four times the bandwidth of the pulse. The bottom curve represents the lower bound on the RMSE of the estimator which is attained if matched filtering is performed on the pulses, where the impulse response of the matched filter is "matched" to either one of the pulses (but not to the pair). Signal-to-thermal noise ratio $SNR_{n,wf}$ is varied from 10 dB to 40 dB, and $SNR_c = 0$ dB as defined by the lag $k = 65$ used in estimation. In this plot, it is assumed that $snr_{n,mf} = snr_{n,wf} \cdot 16/3$ , implying that $BW = 4/(kT_s)$ . . . . .	78
2.15	Ratio of the RMSE (for angle estimates) to $\sqrt{CRLB_N(\gamma)}$ versus $N$ , the number of snapshots used in pre-estimation averaging. From top to bottom, we see the different curves represent the case where $SNR_e$ is approximately 24 dB, 20 dB, 10 dB, 2 dB, and 0 dB, respectively. For each number of snapshots, 10,000 trials were performed. . . . .	80
2.16	Ratio of the RMSE of angle estimates to $\sqrt{CRLB_N(\gamma)}$ versus the number of snapshots used in pre-estimation averaging $N$ , for $SNR_e = 0$ dB. For each number of snapshots, 10,000 trials were performed. A phase angle of $\pi \cdot .357$ radians and a lag of $k = 65$ were assumed, corresponding to a 4-knot target. . . . .	82

2.17	Ratio of the RMSE of angle estimates to $\sqrt{CRLB(\gamma)}$ versus the number of snapshots used in pre-estimation averaging $N$ , for $SNR_e \approx 24$ dB. Black dots indicate the simulated results, and the green line indicates the theoretical prediction for any given $N$ value. For each number of snapshots 10,000 trials were performed. The angle which was being estimated was approximately zero degrees. . . . .	83
3.1	Diagram of a typical forward-looking sonar array mounted on a vessel. . . . .	87
3.2	Comparison of the received signal predicted by Van Trees' theoretical model [25] and monopulse simulation. A signal-to-thermal noise ratio of 40 dB is modeled. . . . .	90
3.3	Comparison of the received signal predicted by Van Trees' theoretical model [25] and pulse pair simulation. . . . .	91
3.4	Comparison of the received signal predicted by Van Trees' theoretical model [25] the received echo produced via simulation for a monopulse. A signal-to-thermal noise ratio of 40 dB is assumed, and the source is modeled to be moving at 10 knots towards the target. . . . .	93
3.5	Comparison of the received signal predicted by Van Trees' theoretical model [25] and simulation for a pulse pair. A signal-to-thermal noise ratio of 40 dB is assumed, and the source is modeled to be moving at 10 knots towards the target. . . . .	94
3.6	Comparison between theory and simulation for the autocovariance (top plot) and cross-covariance (bottom plot) functions, for a monopulse hitting a stationary target. Dashed lines represent the theoretical predictions (green representing the real component, and black representing the imaginary component) while solid lines represent the simulated covariance functions (red lines for the real component, and blue lines for the imaginary component). A signal-to-thermal noise ratio of 40 dB is assumed, and the source is modeled to be stationary relative to the target. 10000 samples of the received time series have been used to form these covariance functions in the simulator. . . . .	96

3.7	Comparison between the theoretically predicted autocovariance function (dashed lines) and the simulator-generated autocovariance function (solid lines) for a pulse pair incident upon a stationary target. A signal-to-thermal noise ratio of 40 dB is assumed, and the source is modeled to be stationary relative to the target. Again, 10000 samples of the received time series have been used to form this covariance function in the simulator. . . . .	97
3.8	Comparison between the theory and simulation for the autocovariance (top plot) and cross-covariance (bottom plot) functions, for a monopulse incident upon a 5-knot target. Dashed lines represent the theoretical predictions (green representing the real component, and black representing the imaginary component) while solid lines represent the simulated covariance functions (red lines for the real component, and blue lines for the imaginary component). A signal-to-thermal noise ratio of 40 dB is assumed, and the source is modeled to be stationary relative to the target. 10000 samples of the received time series have been used to form these covariance functions in the simulator. . .	98
3.9	Comparison between the theoretically predicted autocovariance function (dashed lines) and the simulator-generated autocovariance function (solid lines) for a pulse pair incident upon a 5-knot target. A signal-to-thermal noise ratio of 40 dB is assumed, and the source is modeled to be stationary relative to the target. Again, 10000 samples of the received time series have been used to form this covariance function in the simulator. . . . .	99
3.10	The ping pair incoherent VEM with boat speed held at 5 knots ( $\approx 2.57$ m/s) and an $SNR_n$ of 40 dB (at long range). A 150 cycle monopulse has been assumed, and averaging was performed across 1500 samples. . . . .	102
3.11	The monopulse single ping covariance VEM under high $SNR_n$ conditions. Boat speed was held at 5 knots ( $\approx 2.57$ m/s), and an $SNR_n$ of 40 dB (at long range) was simulated with the "primary simulator". The pulse was 130 cycles long, and estimation was performed at lag $k = 65$ . . . . .	105
3.12	The pulse pair single ping covariance VEM under high $SNR_n$ conditions. Boat speed was held at 5 knots ( $\approx 2.57$ m/s), and an $SNR_n$ of 40 dB (at long range) was simulated. Each pulse in the pair was $k_p = 30$ cycles long, and the pair was separated by $k_s = 35$ cycles of dead time. Estimation was performed at lag $k = 65$ . . . . .	107

3.13	The monopulse ping pair covariance VEM under high $SNR_n$ conditions. Boat speed was held at 0.00309 m/s (0.006 knots), and an $SNR_n$ of 40 dB (at long range) was simulated. The pulse was again 130 cycles long. . . . .	109
4.1	Incoherent velocity estimates corresponding to a boat with an earth-referenced velocity of 4 knots (2 m/s) plotted in color to denote the degree of correlation at each range. These data were taken in the Indian Arm fjord, and range bins of 1500 samples were used to incoherently process pings 15 and 16. Here, a dark copper color indicates a high degree of correlation, whereas lighter colors indicate lesser degrees of correlation. . . . .	115
4.2	Single ping covariance velocity estimates taken in Indian Arm, with the boat moving at 4 knots (approximately 2 m/s) relative to the seafloor. $N = 10$ snapshots were used, and $k = 38$ for this pulse. . . . .	116
4.3	Covariance (red dots) and incoherent (blue dots) velocity estimates taken in Indian Arm, with the boat moving an estimated 4 knots ( $\approx 2$ m/s) relative to the seafloor. Results from the previous two Figures have been superimposed to allow for easy comparison between the VEMs. . . . .	118
4.4	"Side-scan" image taken from pings 1 to 500 of the November 12th, 2009 data. Intensity is plotted for each ping number as a function of range, with dark colors representing low-intensity echoes and lighter colors representing more-intense echoes. The y-axis represents ping number, increasing from ping 1 to ping 500 from the lower left corner of the plot. The x-axis represents range, where range increases from 0 m towards 200 m, moving from left to right across the Figure. . . . .	120
4.5	Simulated reproduction of behavior shown in Figure 4.4, where trends in the ensonified seafloor are seen to approach the transducer array in subsequent pings. The resulting trend appears linear at long distance, but then gives way to a noticeable curve as the range approaches the depth of the seafloor. . . . .	121
5.1	Phase difference between pings 15 and 16 as a function of range. Range bins were 25 samples (or approximately 0.5 m) in size. . . . .	128

5.2 Phase observed at sample number 832 on transducer element 3 throughout the entire 50-ping data set. The red dots indicate the observed phase values, and the black line represents the extrapolated phase between observations. This extrapolated value is added to aid the reader in understanding the (assumed) trend in the data.  $SNR_n$  at this sample number is estimated to be approximately 40 dB throughout the data set. . . . . 129

# Chapter 1

## Introduction

Signal processing represents a crossroads between many disciplines which commonly include mathematics and statistics, physics, and engineering. In general terms, signal processing can be thought of as a field which is concerned with the generation, manipulation, and analysis of signals. The human brain provides an immediate example of an immensely powerful signal processing system, capable of processing many different types of signals simultaneously and converting those signals into information. The reader's eyes are presently converting optical signals from this text into electrical signals which are being interpreted by the brain and are, hopefully, soon to be converted into information about sonar signal processing. Human ears provide an acoustic window to the world by receiving acoustic signals, converting them to electrical signals, and relaying them to the brain for similar processing and interpretation.

Continuing with the example of the human brain, it is easy to imagine scenarios which illustrate its use of acoustic signal processing. Many readers will be able to recall a time when they ate dinner at a crowded restaurant and engaged in conversation with a group of friends or relatives. Crowded restaurants generally have many different people speaking at many different audiences simultaneously, resulting in a noisy environment full of many different acoustic signals. The voice of each speaker usually bears unique information relating to the topic of conversation, but with many speakers talking simultaneously there will be many acoustic signals being received simultaneously by a listener. A good listener is capable of filtering out all the signals from "outside" conversations and instead focusing upon the speech originating from the speaker within their own party. This act of filtering undesired acoustic signals from desired acoustic signals is an example of signal processing, and is performed on a daily basis by human beings the planet over.

Unfortunately, the human brain is not ideally suited for all types of signal processing. With the advent of digital computers and subsequent advances in computer technology which have significantly increased processing power, signal processing is now commonly performed digitally. DSP (digital signal processing) is increasingly common in a world which is increasingly reliant upon computer systems and the electronic transmission, acquisition, and interpretation of data. Seeking to represent signals (which can be optical, acoustic, or otherwise) as a series of numbers or symbols, DSP allows for complicated processing operations to be performed on large amounts of data in little time. This is desirable when many repeated observations or samples are required in order to characterize a given signal or system, and when systems such as the human brain are unable to cope with the magnitude of the operation(s). Returning to the analogy of the human brain processing acoustic signals, an example of such an unrealistic situation might be attempting to generate a plot of a friend's mood as a function of time for the past several decades based upon an interpretation of their speech during that time period. While it would surely be ridiculous to think that a human brain could store, accurately recall, or accurately process the amount of data which would be required for a precise plot of mood versus time over a number of decades, an operation of similar magnitude would be quite feasible for a modern computer.

By beginning with a solid mathematical foundation, the signal processor is able to theoretically define many complicated operations which are used in order to gather information about a given signal. With a knowledge of the physics involved in the system under investigation, the signal processor is able to apply any information gathered from the signal to learn about the environment from which it originated. A knowledge of statistics allows for the analysis of gathered information and the error in any estimates being made or the certainty with which a given conclusion can be made. With the development of modern computers, all of these operations can be performed quickly enough to greatly expand the scope of operations which are attempted.

Enter engineering: the field which allows for the application of DSP to interesting problems and brings DSP out of the laboratory and into "real life." Signal processing, residing at the confluence of so many different technical disciplines, can be used to provide profound information to Mankind and to provide solutions to many everyday problems. A exhaustive discussion of the disciplines in which DSP can be employed is surely beyond the scope of a single Masters thesis, and it is therefore now necessary to confine the scope of the present document to a more manageable level.

The exploration of marine environments such as the ocean represents one such complicated problem which is presently being addressed by the application of DSP. Due to the rapid absorption of light by water, large aqueous bodies are commonly explored by sound rather than by light. Traditionally, a system which acts in this function is known as a sonar system, and the focus of the present thesis will henceforth be limited to a discussion of DSP in the context of sonar systems.

The word "sonar" began as simply an acronym for "Sound Navigation and Ranging". The distinction "Underwater Acoustics" is perhaps more appropriate for present-day usage, as the field has matured to encompass far more than simply navigation and ranging, but the two terms are used interchangeably in much of the literature. Common modern-day applications can involve the use of sonar systems to create detailed maps of the seafloor (a process known as "bathymetry"), to detect the presence of targets which are suspended in the water (such as marine life, scuba divers, or submarines), and to estimate the velocity of a given target (such as water column targets, surface targets, or the velocity of the sonar system itself relative to the seafloor).

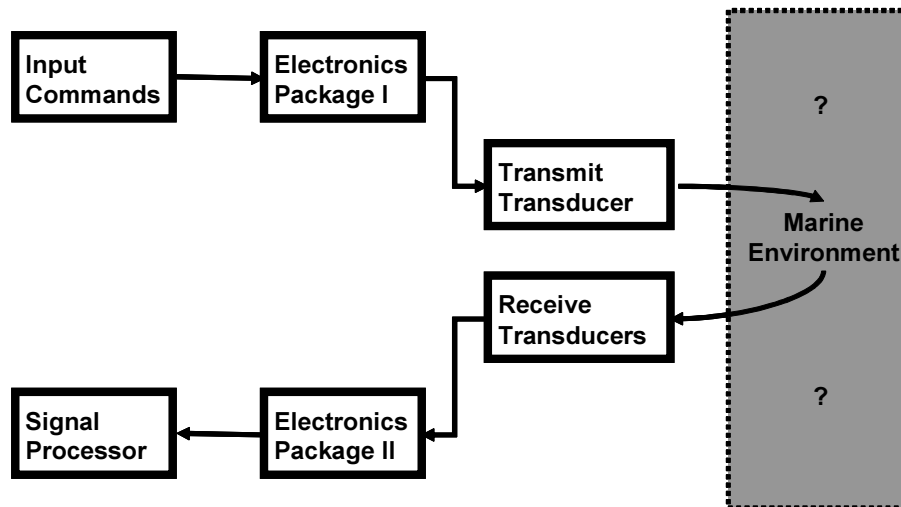


Figure 1.1: General block diagram of a sonar system.

The operation of a sonar system is indeed multifaceted, and depends upon the proper operation of many complicated components - many of which are well beyond the scope of a single thesis. Figure 1.1 provides a general block diagram of a sonar system such as

the one discussed in this thesis. The sonar system employed by the Underwater Research Laboratory (URL) begins its operation by taking user-defined inputs and modifying system parameters accordingly. Next, these parameters are sent to the first of two electronics packages which performs such functions as timing control and pulse generation. Electric signals generated by Electronics Package I are then converted into acoustic signals via the transmit transducer, and these acoustic signals then travel out into the as-of-yet unexplored marine environment. When these transmitted acoustic signals interact with objects in the marine environment, these objects - usually called "scatterers" - create an acoustic echo which has certain characteristics that depend upon the location and speed of the scatterer, among other attributes. In the bathymetric sonar system used by the URL, the returning echo is received by a group of transducers, then sent to a second electronics package for filtering and general "cleaning-up" prior to processing. Finally, after the acoustic signal has been created, transmitted, received and filtered, a DSP system is employed to examine the content of the returned signal.

The present thesis is primarily concerned with the study of acoustic signals (which are converted into electrical signals by the sonar system transducers) and the information that can be gained about the environment from which these signals originated. In this context, let us loosely refer to the practice of making inferences about an underwater environment based upon its echo signature as "Sonar Signal Processing." In particular, this thesis is concerned with the estimation of the velocity of sonar targets.

## 1.1 Background

Regardless of preferred name, the field of underwater acoustics can trace its origins all the way back to Leonardo da Vinci in the fifteenth century [7]. Da Vinci discovered that by placing one end of a tube in the water and the other end next to his ear, it was possible to hear boats from a great distance. Sonar technology saw significant advances during the First World War as Allied countries, namely Britain and France, sought to protect themselves against both an airborne and underwater threat. Primitive sonar systems used at the time involved little more than large acoustic horns and a stethoscope connected to the operator's ears, and some were employed outside of the water to detect the presence of enemy aircraft. Such a system would be characterized as "passive" because its operation is solely as a receiver (in other words, it listens to sounds but does not intentionally transmit

any sound itself). An "active" system is one which includes a device to create and transmit an acoustic signal as well as a receiver to listen to the echoes caused by this signal. The process of transmitting a signal and listening to the resulting echoes (before transmitting again) is called a "ping"; a data set from an active bathymetric sonar system may contain numerous pings. Passive acoustic systems cannot detect the presence of so-called "quiet" targets which transmit little or no sound themselves, such as rocks on the seafloor, while active systems can. In either case, however, an interpretation of the received signals is still required in order to characterize the objects which influenced them.

British and American researchers eventually employed the principles of wave interference (of the incoming acoustic signals) to estimate the location of underwater targets such as submarines. Interferometric sonar systems rely upon listening to acoustic signals at two or more closely-spaced locations and measuring phase differences between these locations. If it is discovered that incoming waves exhibit no phase difference between two receivers (located at an appropriate spacing based upon the wavelength of the incoming signal) then it is concluded that the receiving array is pointed directly at the target. If the receiving array is then turned slightly so that it no longer points directly at the source of these acoustic signals, then one of the receivers will now be located slightly closer to the target and the other receiver will be slightly further from the target. The resulting pathlength difference causes interference when the two received signals are compared.

Some WWI-era sonar systems which were used effectively to locate submarines bore a striking resemblance to da Vinci's design, and operated by lowering two independent acoustic horns (receivers) into the water and connecting the horn on the right or left side to the operator's corresponding right or left ear. To early sonar system operators who were quite literally "listening" for the sounds of submarines, a pathlength difference between receivers would sound like a beat frequency. If a beat frequency was heard, the operator would then physically rotate the receiving array until it was pointing directly at the source of the sound, which caused the pathlengths to the two receivers to be equivalent and the beat frequency to disappear. The presence and approximate bearing of a submarine were thus established.

Today, although technology has seen significant advances since the First World War, many sonar systems are based off of similar interferometric principles. Although submarine detection remains as an area of interest for the sonar community, many other applications have emerged which have served to expand the field. Modern sonar systems have seen

application in the creation of bathymetric seafloor profiles, the profiling of ocean currents near offshore structures, blood-flow monitoring in hospital patients, and the monitoring of industrial processes (such as impurity detection) while liquid flows through a pipe.

Confining the scope of the present thesis to a more manageable level, the focus is turned to sonar systems which are designed to profile the seafloor. Known as bathymetric sonar systems, these devices are usually towed by maritime vessels and use interferometry to locate, profile, and sometimes to characterize the "bottom". It is frequently the case that a bathymetric sonar system would be configured such that a forward-moving boat would proceed at a low speed, commonly on the order of a few knots, while the sonar system was pointed off of either the port or starboard side of the vessel (performing a "side scan").

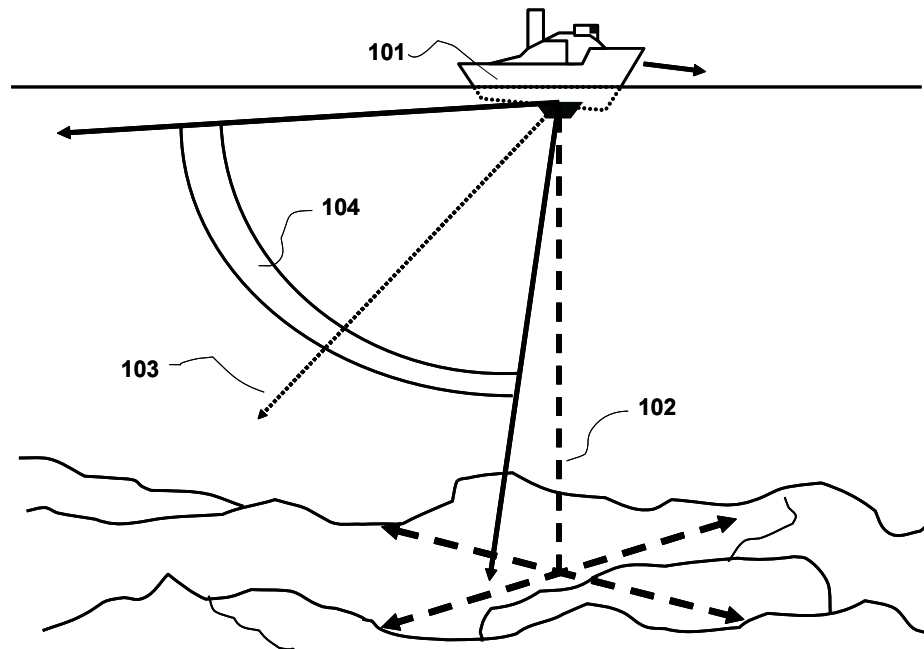


Figure 1.2: Typical side-scan bathymetric boat-mounted sonar.

This experimental setup is diagramed in Figure 1.2, where a boat (101) employs a hull-mounted sonar system to profile the seafloor. 102 shows the vertical axis of the sonar system projected on the seafloor, with 103 representing the direction in which the sonar system is pointed (commonly referred to as the "boresight"). The sonar system is seen to emit a single pulse (104) which travels away from the boat and eventually begins to echo off of the

seafloor. When the echoes arrive, they are only from the portion of the seafloor which was contained inside the sonar beam. As the beam is narrow in the direction of travel of the boat (the along-track) the process begins by profiling this narrow section of the seafloor, and then moving the boat ahead slightly and repeating the process again. These "slices" of seafloor profile are then joined into a single profile of the seafloor, creating a swath of profiled seafloor in the along-track of the boat. An excellent reference for this technology is [10].

### 1.1.1 Review of the URL Sonar System

The Underwater Research Laboratory (URL) at Simon Fraser University (SFU) has developed a bathymetric sonar system which uses interferometric principles. As with Figure 1.2, typical operation in the field involves aiming the sonar system off of one side of the boat and tilting it towards the seafloor such that the angle between the surface of the water and the boresight of the transducer array increases. It is the transducer array itself, however, which distinguishes the URL sonar system from other sonar modern sonar systems.

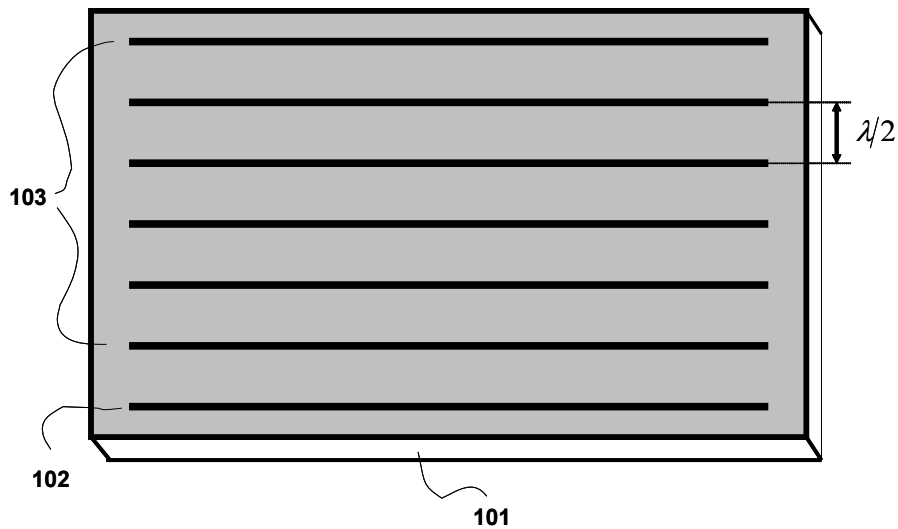


Figure 1.3: "Bird's eye" view diagram of a typical URL transducer array. One transducer element is used for sound transmission, and another six elements are used for reception.

Figure 1.3 provides a diagram of a typical transducer array used by the URL. The

transducer array (101) is composed of seven individual transducer elements: one transmit element (102) which is used to create each transmit signal, and six receive transducer elements (103) which are used to detect the echoes that result from the transmitted signal. All transducer elements are maintained at a spacing which is equal to half of the carrier wavelength  $\lambda_c/2$  from adjacent transducer elements. URL sonar systems usually operate in the 100 kHz to 300 kHz range, making the transducer element spacing typically in the range of approximately 7.5 mm to 2.5 mm, respectively.

For increased along-track resolution of the seafloor, it is desirable to keep the along-track beamwidth (of the sonar system) narrow. This narrowing of the beamwidth in the along-track dimension is achieved by lengthening the transducer elements in the along-track dimension while keeping the  $\lambda_c/2$  inter-element spacing constant. Figure 1.4 shows how all transducer elements (102) are long in one dimension which results in a narrow beamwidth in the same dimension. During data acquisition, the transducer array (101) would then be oriented such that this "long dimension" of the transducer elements is parallel to the along-track of the vessel. The spread of the beam in the along-track dimension (the beamwidth) is denoted by  $\delta$  and is measured in units of either degrees or radians. The precise value of this quantity is not of importance in the present thesis, but deserves mentioning as it serves to constrain the view of the sonar system.

As has been mentioned, many interferometric arrays only include two receive elements, for this is all that is necessary to estimate a single angle of arrival of a returning echo. However, many situations exist in which a sonar system might simultaneously receive echoes from multiple angles of arrival. Suppose that at a given instant in time the sonar system simultaneously receives echoes from two distinct water column scatterers (such as a pair of fish). These two signals are arriving from different locations but a common range, and thus require the simultaneous estimation of two angles of arrival (AOAs).

Consider Figure 1.5, in which two water column targets are located at a common range but at different locations. The first target, 101, is located at angle  $\phi_1$  relative to the transducer boresight 103. The second target, 102, is located at the same range as 101 but is instead at a different angle,  $\phi_2$ , relative to transducer boresight. An interferometric sonar system which employs two receive transducer elements would not be able to distinguish between the two targets and would not be capable of estimating both of their locations simultaneously. Being capable of only locating a single target at a time, such a sonar system would estimate that there exists a single target at this range and at an AOA somewhere

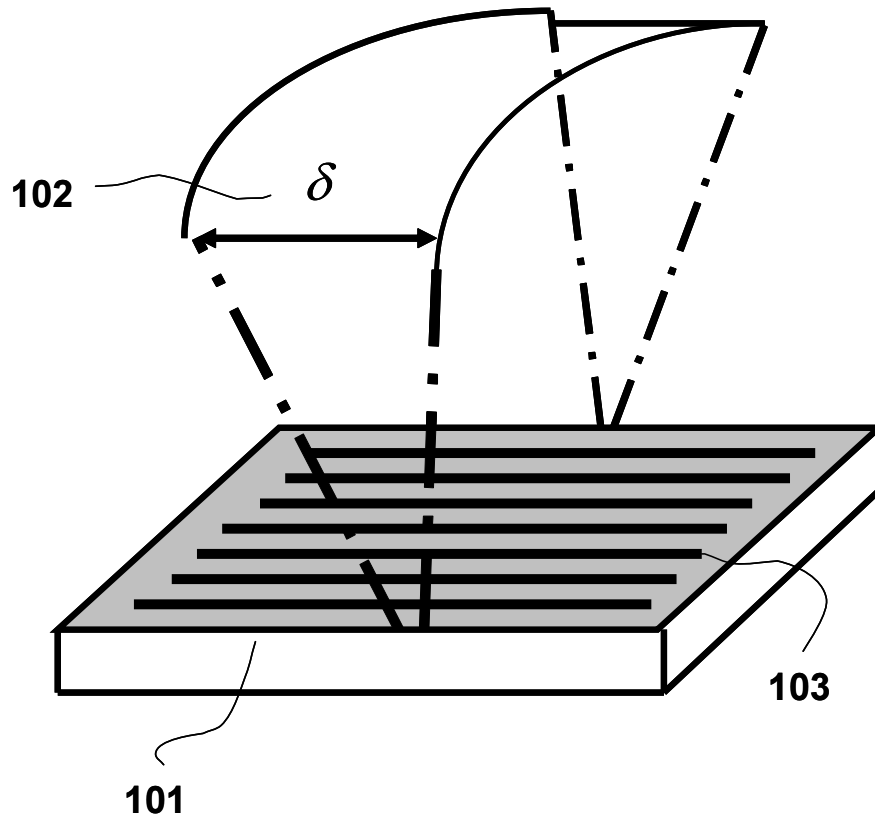


Figure 1.4: Narrow along-track beamwidth of URL transducer arrays.

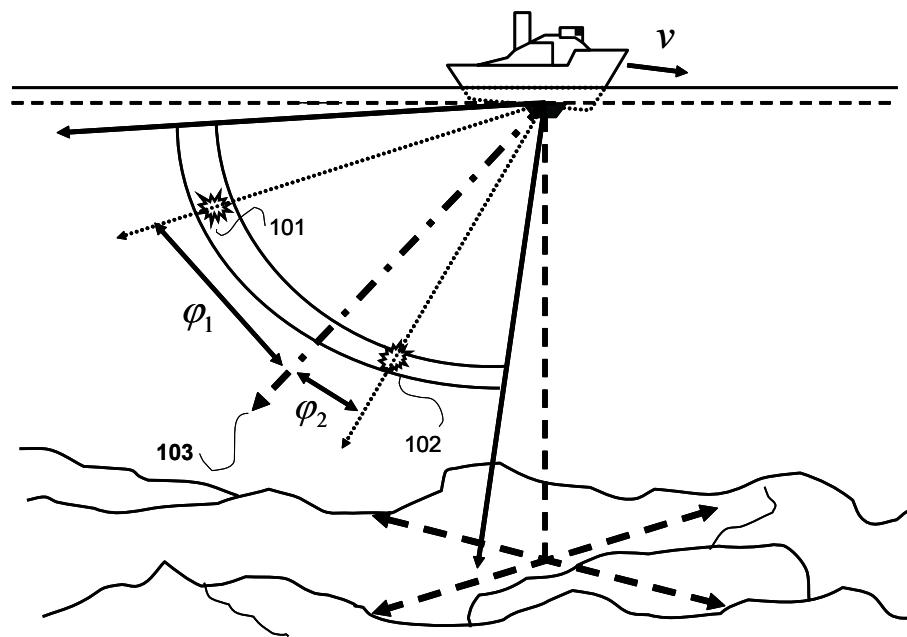


Figure 1.5: Typical two-target scenario, with both targets existing at a common range.

between  $\phi_1$  and  $\phi_2$ , biased towards AOA of the stronger of the two scatterers.

Because the URL transducer presently under consideration employs six receive transducer elements, it would be capable of resolving the two scatterers. Paul Kraeutner and John Bird invented the URL's sonar system, and have described its operation in [11]. However, the present thesis is concerned not with the construction of such a sonar system, but with its ability to estimate a target's velocity. We therefore omit a detailed discussion of the operation of bathymetric sonar systems, such as the URL's. The interested reader can refer to the literature which has already been published on this matter (such as [3] and [11]).

## 1.2 Velocity Estimation

Velocity estimation has started to play an increasingly important role in modern sonar systems. When combined with accurate estimates of the angle of arrival, such a system can be employed (among other uses) to track the earth-referenced velocity of a vessel in the water, to identify the velocity of an unknown target in the water column, to monitor the flow of oceanic or river currents [5, 12, 6], for use as a security system which detects the presence of moving targets, and for studying the flow of sand and heat through the bottom boundary layer in the ocean [13, 27, 30, 28, 21, 29, 14]. Velocity estimation is also important to the medical community, and sees frequent application in blood-flow monitoring systems. Frequently employed by radar systems as well, velocity estimation also plays a crucial role in such disciplines as meteorology (see [1], [31], and [2]). The applications of velocity estimation technology are far reaching indeed.

The Doppler effect was noticed by Christian Doppler in the mid-19th century, and was famously observed a few years later when many trumpet players were placed on a moving railway car and many more were placed in static positions on the ground next to the tracks. Both groups were told to hold the same note, and observers were strategically placed throughout the train and along the ground next to the tracks, listening to the groups of trumpet players. It was confirmed that the as trumpet players physically moved away from their observers (according to each observer's frame of reference) the frequency of the note heard by the static observers became lower.

Physically, this change in frequency results directly from a relative motion between the transmitter and the receiver (or observer). It does not matter whether it is the transmitter

or receiver that is moving; all that matters is that a relative motion exists. Speaking from the receiver's frame of reference, one can say that the transmitter is seen to be moving (and the receiver is perceived to be static) while the transmitter sends out the signal. If the transmitter is seen to approach the receiver, the waves emitted by the transmitter are seen to arrive in a more rapid succession than they would if the transmitter were not approaching the receiver. Because sound speed is taken to be constant, the increased frequency with which sound waves arrive at the receiver corresponds to a decreased wavelength (or distance between successive waves).

Mathematically, the Doppler effect is expressed as [24]:

$$f' = f_0 + \frac{f_0 v}{c} \quad (1.1)$$

$$f' - f_0 = \Delta f = \frac{f_0 v}{c} \quad (1.2)$$

where  $c$  is the speed of the wave in the medium,  $f_0$  is the transmitted frequency,  $f'$  is the observed frequency,  $\Delta f$  is the difference between these two frequencies, and  $v$  is the relative radial velocity between the source of the sound and the receiver. In defining the equations thusly, we have made the arbitrary designation that a positive  $v$  indicates that the distance between source and receiver is closing, which means that the received signal  $f'$  is greater than  $f_0$ .

For bathymetric side-scan sonar applications, however, the transmitter and receiver are located in essentially the same location (known as a monostatic sonar system [7]). In such a case, two Doppler shifts are observed, not just one. Suppose that a boat carrying a hull-mounted sonar system, such as in Figure 1.6, has aimed the sonar beam so that it points ahead of the vessel (101). The boresight (103) is aimed in front of the vessel at a downward angle, where vertical axis 102 is used to project the other axes onto the relatively flat seafloor. Suppose that the vessel is moving ahead some velocity  $v$  when it transmits a ping (104). The first Doppler shift occurs during transmission, and is directly analogous to the redshift effect known to astronomers and astrophysicists. This Doppler-shifted pulse then propagates through the medium (water) and interacts with the seafloor, returning to the receive transducer array where the second Doppler shift occurs during reception.

Mathematically, we now see that the received signal is not at frequency  $f'$  but at frequency  $f''$ , indicating that not one but two Doppler shifts have occurred. After the first

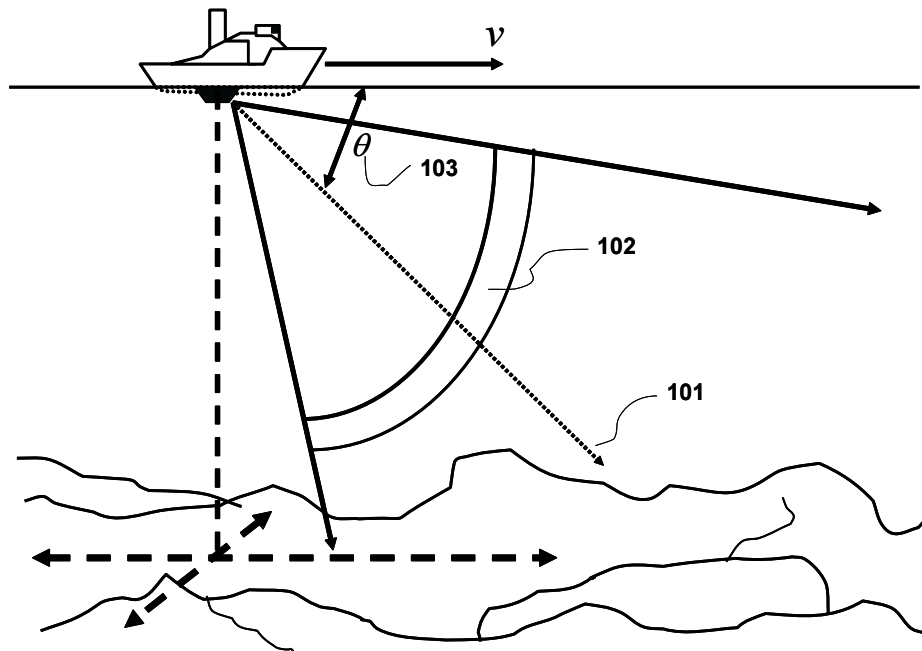


Figure 1.6: Forward-looking hull-mounted sonar system.

Doppler shift (immediately after transmission, in the present example) the signal has frequency  $f'$  as described by Equation 1.1. The second Doppler shift then occurs on this already shifted signal, such that:

$$f'' = f' + \frac{f'v}{c} = f' \left(1 + \frac{v}{c}\right) = f_0 \left(1 + \frac{v}{c}\right)^2 \quad (1.3)$$

which we expand, and then simplify if we assume that  $v \ll c$ :

$$f'' = f_0 \left(1 + \frac{2v}{c} + \frac{v^2}{c^2}\right) \approx f_0 \left(1 + \frac{2v}{c}\right). \quad (1.4)$$

Although some exceptions apply, many applications of bathymetric side-scan sonar systems do not involve targets (or sources) which are capable of speeds greater than 10 knots. For this reason, it is assumed that for the present thesis the simplification of Equation 1.4 is valid in the general case. We leave our discussion of frequency shifts here, because the present sonar system estimates target velocity based not in the frequency domain, but in the time domain via phase shifts. A detailed discussion of this procedure is given in the following Chapter.

### 1.2.1 Introducing "Micro Doppler"

In subsequent Chapters, much time is spent discussing some of the more "traditional" velocity estimation methods. These traditional methods include the ping to ping incoherent, the ping pair covariance, and the pulse pair covariance methods. Such methods rely - for the most part - upon a direct measurement of phase change between subsequent observations of the target(s), and from this phase measurement a target velocity is calculated.

The research which has been devoted to the study of these predominant methods has suggested an alternative means by which to detect a target (and to indirectly estimate its velocity): the "micro Doppler" method. A sonar system which is fastened to a relatively fixed object (such as a dock, or an oil rig) may utilize this micro Doppler method to estimate and compensate for any small motions of the sonar system (i.e. rocking with the waves, or water current) and to detect incoming targets. The concept of micro Doppler has been discussed in the literature [22] as a useful target identification tool in radar applications, where the fine movements or vibrations of a target can be used, for instance, to determine whether it is powered by a diesel or turbine engine. However, micro-Doppler has yet to be

used as a means to compensate for the own-motion of a semi-stationary transmit/receive sonar system, which also facilitates the detection of targets by the change in phase which their presence introduces to a particular region inside the transmit beam.

### 1.3 Review of Current Literature and Contributions of the Thesis

Two-point Doppler estimation, the focus of this thesis, is a common approach to velocity estimation. In simple terms, it is a process where an estimate of a target's velocity is generated after it has been "observed" twice. In sonar, observations of a target are generated by transmitting one or more pings and sampling the received echo. Multiple observations of a target may be collected inside of each ping, or across multiple pings. In the simplest sense, an observation of a target is a single sample of the echo which is returned by that target. A second observation may be the sampling of a later echo produced by that target, either inside the same ping or in a subsequent ping.

The covariance, or linear prediction, approach to velocity estimation is a very common approach in today's sonar community [12, 14, 21, 2]. Teledyne RD Instruments have successfully marketed - for years - a number of Doppler current profilers and Doppler velocity logs which are based on this approach to velocity estimation. Meteorologists have also relied upon the covariance approach to velocity estimation for years [1, 31, 2]. Two-point Doppler estimation is achieved in this sense by using two time samples to estimate the covariance function (either the autocovariance or cross covariance function, depending upon whether the single ping or ping pair covariance method is used) at a specific lag. It is also possible to estimate a much larger portion of the covariance function - more than estimating it at one specific lag - by correlating range bins rather than single samples, but this is no longer two-point Doppler estimation.

Two-point estimation is a less complicated - and perhaps more direct - approach to the velocity estimation problem. By learning the foundations of such a procedure, results can be applied or extended to treat more complicated cases which may arise in practice. Furthermore, by studying and probing the two-point estimation methods, we both apply and contribute to a great deal of theoretical work which pertains to velocity estimation.

However, there have existed a number of holes in the understanding of such two-point

methods. All the velocity estimation methods which are considered herein rely upon estimating some covariance function, and in practice the targets are frequently range-spread (as opposed to being point targets). To date, the auto- and cross-covariance functions for a moving range-spread target have yet to be developed mathematically - and the fundamental understanding of these common velocity estimation methods cannot be considered complete without such a step.

Furthermore, an in-depth analysis of their theoretical performance limitations is also presently lacking in the literature. While these methods are used on a daily basis to monitor current flow through rivers or estimate the motion of clouds, insufficient research has been conducted into probing the theory which describes their behavior and their performance limitations. Without such an understanding, it cannot be said that all current systems are being used in a way which allows them to approach their theoretical "best" performance, and in fact many such systems may suffer from unnecessarily poor performance.

It is the goal of this thesis to address these holes in the present-day understanding of two-point velocity estimation. Stated explicitly, this thesis concerns velocity estimation in the context of a bathymetric side-scan sonar system, and provides a foundational discussion of three velocity estimation methods and their theoretical performance limitations. The velocity estimation methods considered are: incoherent velocity estimation, ping pair covariance estimation, and pulse pair covariance estimation. This investigation assumes that two common types of transmit waveforms are used for velocity estimation: monopulse waveforms and pulse pair waveforms, and includes a detailed discussion of these envelopes.

A number of important contributions concerning velocity estimation in the context of a sonar system are presented herein. Firstly, auto- and cross-covariance functions for moving range-spread targets are derived, beginning from Van Trees' theory for stationary range-spread targets. The velocity estimation methods are then explicitly defined in terms of the covariance function upon which they are based, and these covariance functions are used to derive an expression for the Cramer-Rao lower bound (CRLB) for each of the coherent methods. The properties of the CRLB (for each method) are then explored, resulting in the discovery of the optimal lag  $k_0$  at which single ping covariance estimation should be performed. Through simulation, we develop values for the ratio of root mean-square error (RMSE) to the square root of the CRLB which we expect to observe in practice, given assumptions about the signal-to-noise ratio and number of independent snapshots which are used in estimation. Finally, the micro-Doppler method is introduced as a novel means

to compensate for the small-scale motions of the sonar system as it seeks to detect the presence of "new" targets inside the field of view.

When possible, certain equations developed in the Theoretical Analysis chapter are evaluated to provide the reader with a physically significant and numerical result. In such cases, assumptions about the sonar system are made which facilitate the numerical results (for instance, the sonar system is assumed to operate at a carrier frequency of 300 kHz). In simulation, the same carrier frequency is assumed - even though some URL transducers operate at other frequencies.

## 1.4 Thesis Organization

Following the Introduction, a discussion of the relevant theoretical concerns is given. The work of Harry Van Trees represents a massive theoretical contribution to the field of signal processing in the context of detection, estimation, and modulation theory. These theoretical contributions, having been widely accepted in this field and having been used extensively as the foundation of other theoretical developments, serve as an excellent foundation for the present investigation into sonar signal processing.

This discussion begins by reproducing Harry Van Trees' theory relating to slowly fluctuating point targets and to range spread targets [25], and extends his theoretical developments when appropriate. Covariance functions are developed in each case, representing the auto- and cross covariance between received signals which are returning from such targets. A noise model, used by Bird and Mullins in [3], is presented which provides a detailed way in which to describe the noise which can cause decorrelation between segments of the received time series. The velocity estimation methods are then described mathematically (in the context of both transmit waveforms) and their dependence upon the covariance functions for a range spread target is shown. Finally, the Cramer-Rao lower bound for each velocity estimator is developed from the covariance functions for a range spread target, and the theoretical performance bounds of the coherent estimators are compared.

Following the discussion of the relevant theory, attention is turned towards the simulators and estimation programs which have been created by the author. These simulators mimic the actual physical behavior which occurs in nature, and for this reason it is important to begin by showing agreement between the theory described in the preceding section and any simulation. Simulators model the transmission of a particular waveform and the scatterers

off of which it reflects, and create a time series composed of samples of the resulting received echo. Estimators (or rather, "estimation programs") are used to then take the simulated data and use it to generate a velocity profile. Once agreement has been established between theory and simulation, attention is then turned to the results yielded by each simulator and estimator for each corresponding VEM.

Next, experimental data are introduced to further evaluate the performance of the VEMs. All experimental data have been taken with a monopulse as the transmit waveform, and not with a pulse pair. Experimental data are therefore used to help evaluate the performance of each VEM which is coupled with a monopulse, and projections are made as to the anticipated experimental performance of a pulse pair.

Finally, the micro Doppler method is introduced. After presenting the relevant theoretical considerations, experimental data are used to demonstrate that this method is capable of tracking the minor phase variations which a semi-stationary sonar system observes between pings. It is concluded that this method has great potential to provide a novel means by which a semi-stationary sonar system can compensate for its own small-scale motion and accurately detect changes in the environment which it is observing (such as from water column targets).

## Chapter 2

# Theoretical Analysis

Let us begin our technical analysis by discussing the relevant theory behind sonar signal processing and velocity estimation. By beginning thusly, it is hoped that we can develop both a familiarity with the math and also an intuition for the related physical behavior. As this thesis does not concern the supporting electronics packages, and simply assumes their proper functionality, we begin our specific theoretical discussion with a description of the physical situation which is to be modeled. This initial discussion seeks to capture the "essence" of the physical situation which is of interest in this thesis: a signal is transmitted into the water, the signal scatters and an echo is formed which returns to the transducers, and then this echo is received and analyzed.

Once we have discussed these main concepts in broad terms, a mathematical description of both the signal and its target is presented. A discussion of the transmitted signal is important because this signal imposes certain constraints upon the system that are difficult - if not impossible - to overcome with any amount of signal processing. The target model allows us to determine what happens to the signal upon reflection, and it is used to help develop the theoretical foundation of this thesis. The foundation for both of the models which are to be used (a slowly-fluctuating point target, and a range spread target) have been developed by Harry Van Trees [25]. After beginning by reproducing these foundations, the models are extended and the correlation functions for the received signal returning from a range spread target (with Doppler) are developed.

A detailed noise model is then presented, which was developed by Bird and Mullins in [3]. This model accounts for not only thermal noise, but also develops the concept of "decorrelation noise". This concept is introduced to treat the case where two time samples

differ not only because of the presence of thermal noise, but also because the returning signals which contributed to each time sample are only partially similar (for instance, a particular set of scatterers contributed to one time sample, but this set of contributing scatterers was slightly different for the second time sample). While Bird and Mullins applied their noise model to describe the comparison of time samples across different transducer elements, in this thesis we apply the model to different time samples from the same transducer.

Finally, after describing the signals which are to be transmitted and after modeling the targets off of which these signals reflect, a discussion of the velocity estimation methods (VEMs) is given. With our definition that a "ping" is the process of transmitting a waveform (or waveforms) and then receiving the resultant echoes, we discuss the VEMs for each potential transmit waveform. Monopulse waveforms - one pulse transmitted in each ping - allow for the ping pair incoherent and covariance method to be employed, while for the pulse pair waveform - two distinct pulses transmitted in each ping - we only consider covariance processing. This terminology is described in greater detail later when the theory behind these estimation methods is described. The Cramer-Rao bound for the coherent velocity estimators is derived, and an in-depth analysis into the factors which influence the bound is then provided.

## 2.1 Description of the Situation Which is to be Modeled

We seek to develop a model for the transmission of a signal, the scattering of that signal, and the echo which results from that scattering. We assume that there may exist some relative motion between the transducer and the target (scatterer) during this time. A simplification of this process is the scattering of a signal off of a slowly fluctuating point target. However, because we seek to use the sonar system to develop a velocity profile as a function of range where the signal is scattering off of a continuous seafloor, we must extend this model to treat moving distributed targets rather than only moving point targets.

Adding another necessary level of complexity to this problem, we now define the waveforms which may be transmitted from the transducer. Two types of transmit waveforms are considered: the monopulse, and the pulse pair. These two waveforms are referred to frequently throughout this thesis, making it essential that they be well-defined. As has previously been mentioned, the primary difference between these two waveforms is the number of pulses which are transmitted in each ping. The reader will recall that a "ping" has been

defined as the process of creating some sound, and then ceasing transmission of that sound and beginning reception of the subsequent echoes. The next ping would begin after the last echo from the previous ping has been received (or rather, after the last *useful* echo has been received) and would involve creating a new sound and listening to the echoes caused by this second sound.

Figure 2.1 shows an ideal plot of the magnitude of these transmit waveforms as a function of arbitrary time units. The top figure is a magnitude plot of a monopulse, while the lower plot is of a pulse pair. Of primary importance here is the shape of each waveform, and not its amplitude or duration (which are plotted in arbitrary units). We seek only to compare the differences between these two waveforms: the monopulse is a single pulse while the pulse pair is a pair of pulses which are transmitted in the same ping and are separated from each other by some amount of dead time (which is usually measured in units of carrier frequency cycles).

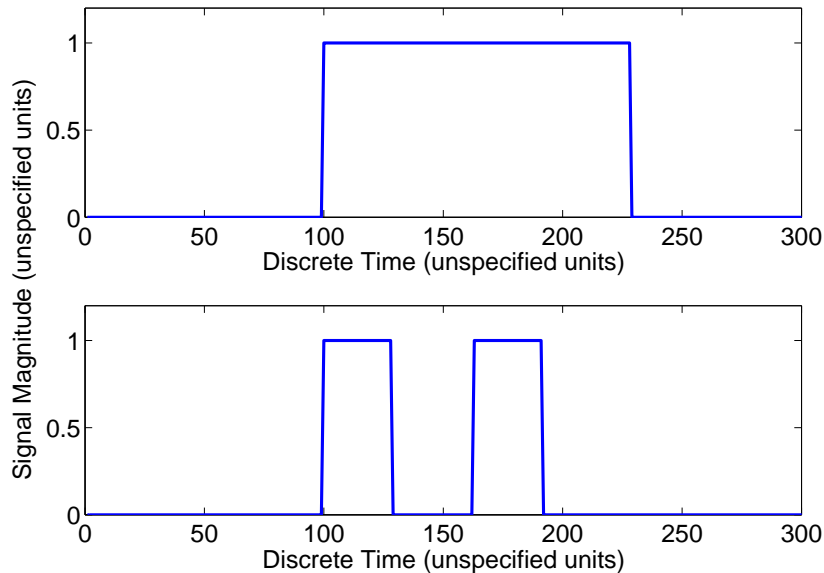


Figure 2.1: Transmit waveforms of interest to the URL: monopulse (top) and pulse pair (bottom). As pictured, the monopulse is 130 cycles of the carrier frequency in length. Each pulse in the pulse pair is 30 cycles in length with a separation between pulses of 35 cycles (of the carrier).

In determining the received echo resulting from the transmission of these waveforms, we begin developing our target model in the simplest sense: the transmission and reflection of some wave off of a single point target, which is moving at some velocity  $v$ . In this analysis it is not important whether it is the target which is moving or the transducer which is moving. Figure 2.2 shows the transducer (101) transmitting a wave (104) that gets reflected off of some point target (103) which moves with velocity  $v$ , and finally the echo (102) returning to the transducer. Once this simplistic model has been developed, we then develop a model for a range-spread target.

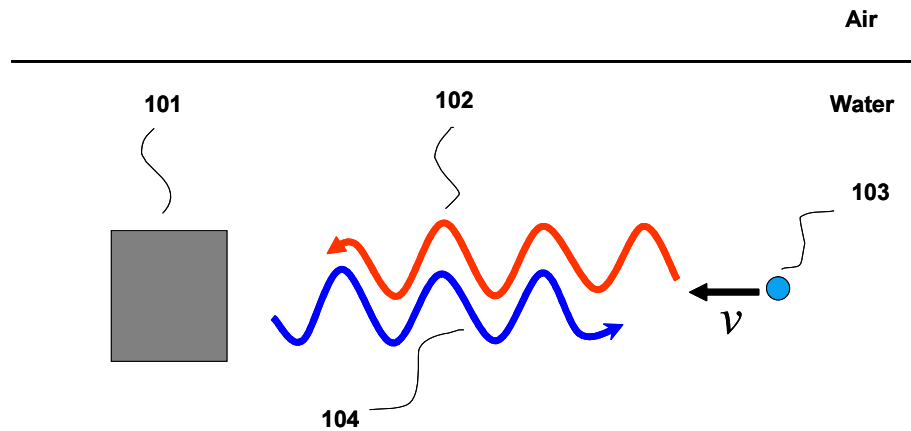


Figure 2.2: Basic model of sound transmission and reflection off of a point target.

Typically, the sonar system would be mounted on a boat. If this sonar system is facing forwards and if the boat is moving forwards, then a relative velocity between the ensonified bottom scatterers in front of the boat and the transducer array is present. Figure 2.3 shows the transmission of a monopulse by a forward-looking sonar system mounted on a forward-moving boat. The blue wave (representing the carrier signal generated by the sonar system) is confined within a single envelope.

Figure 2.4 is similar to Figure 2.3, except two distinct envelopes are transmitted rather than only one envelope. Both envelopes are of similar length (a certain number of cycles of the carrier frequency) and are separated by some amount of dead time. As these two pulses travel along the seafloor, echoes are simultaneously returning from both pulses. This simultaneous return of echoes from two different portions of the seafloor is a mixed blessing,

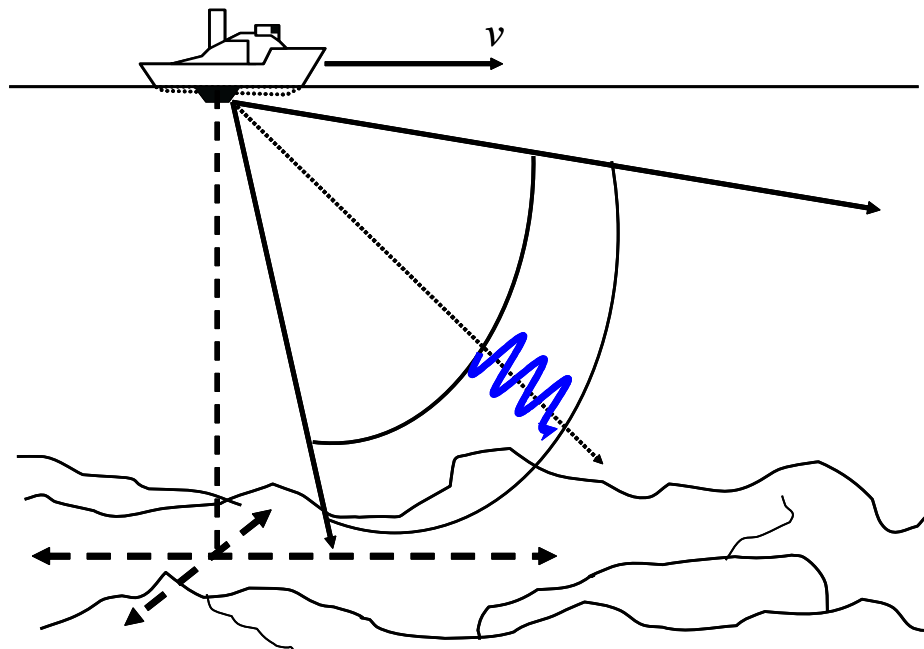


Figure 2.3: Transmission of a monopulse by a forward-looking sonar system.

allowing for two "measurements", or echoes, to be returned from each portion of seafloor in only a single ping, but also introducing a level of interference in each measurement (the echoes from one portion of the seafloor arrive at the same time as echoes from a completely different portion of the seafloor).

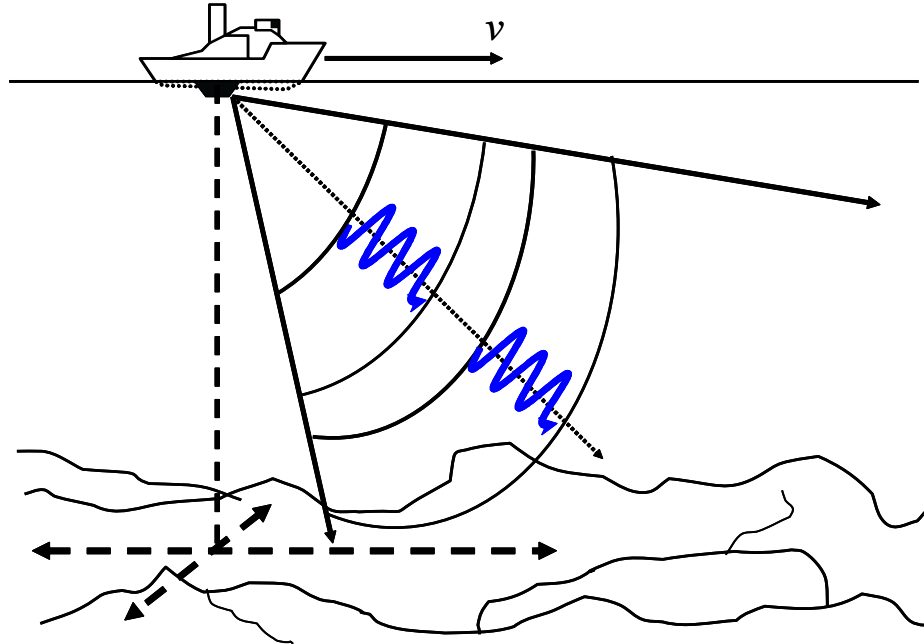


Figure 2.4: Transmission of a pulse pair by a forward-looking sonar system.

Since we seek to model the returns from a portion of the seafloor, a more descriptive target model is that of the range-spread target and not that of the point target. It is for this reason that after beginning with the simple case of a slowly fluctuating point target, we extend our target model to the case of a range-spread (or distributed) target.

## 2.2 Target Models

We shall proceed by introducing the theory which has been established by Van Trees to describe slowly fluctuating point targets [25]. The aim here is to first describe the targets which will be encountered by the sonar system in a simplistic manner (modeling them as

stationary point targets) which is later expanded (modeling the targets as moving range-spread targets), and then in subsequent sections to prove that the simulation created by the author acts in accordance with the behavior described by Van Trees. It should be noted that the bulk of the theoretical development immediately following is not the work of the author, but of Harry Van Trees. However, since Van Trees' models do not completely describe the system which we seek to model in the present thesis, certain changes and extensions have been made where noted.

The goal here is to describe the signal which returns from the target, and to then develop a mathematical model for how it correlates with itself or another such returning signal. In doing so, we seek greater insight into the velocity estimation methods - all of which (that are considered in this thesis) rely in some way upon the correlation of a returning signal or signals.

### 2.2.1 Slowly Fluctuating Point Target

Van Trees begins by establishing the signal model corresponding to a slowly fluctuating point target. We represent the transmitted signal  $s_t(t)$  as a cosine wave:

$$s_t(t) = \sqrt{2P_t} \cos w_c t = \sqrt{2P_t} \operatorname{Re} [e^{jw_c t}] \quad (2.1)$$

where  $P_t$  represents the transmitted power and where  $f_c$  and  $w_c = 2\pi f_c$  are the frequency of the carrier expressed in units of Hertz and radians per second, respectively. We model the received wave as:

$$s_r(t) = \sqrt{2} \operatorname{Re} \left[ \sqrt{P_t} \sum_{i=1}^k g_i e^{jw_c(t-\tau)+\theta_i} \right] \quad (2.2)$$

where the target has  $k$  reflecting surfaces,  $g_i$  represents the attenuation caused by path loss, antenna gain, and scattering.  $\theta_i$  is the random phase which is incurred by the signal upon scattering, and  $\tau = \frac{2R}{c}$  is the two-way travel time from transmission to reception when the target is at a constant range  $R$  and sound travels at speed  $c$ . By applying the central limit theorem, Van Trees seeks to represent the sum (in 2.2, which represents the reflections from a target composed of several reflecting surfaces) as a Gaussian random variable  $\tilde{b}$ . Van Trees makes the assumptions that  $k$  be large, that  $g_i$ 's have equal magnitude, and that  $\theta_i$ 's are statistically independent. He proceeds by assuming a relative target velocity of zero, which causes the expression for the received signal to become:

$$s_r(t) = \sqrt{2}Re \left[ \sqrt{P_t} \tilde{b} e^{jw_c(t-\tau)} \right] \quad (2.3)$$

where  $\tilde{b}$  is a complex Gaussian random variable with  $E\{\tilde{b}\tilde{b}^*\} = 2\sigma_b^2$ . Van Trees assumes that any reflection process is frequency-independent, namely:

$$s_t(t) = \sqrt{2}Re \left[ \sqrt{P_t} e^{jw_c t + jw t} \right] \quad (2.4)$$

results in

$$s_r(t) = \sqrt{2}Re \left[ \sqrt{P_t} \tilde{b} e^{j(w_c + w)(t-\tau)} \right]. \quad (2.5)$$

Next, Van Trees assumes that any reflection process is linear such that the transmitted signal  $s_t(t)$

$$s_t(t) = \sqrt{2}Re \left[ \sqrt{E_t} \tilde{f}(t) e^{jw_c t} \right] \quad (2.6)$$

$$= \sqrt{2}Re \left[ \sqrt{E_t} e^{jw_c t} \int_{-\infty}^{\infty} \tilde{F}(jw) e^{jw t} \frac{dw}{2\pi} \right] \quad (2.7)$$

and the received signal  $s_r(t)$  is:

$$\begin{aligned} s_r(t) &= \sqrt{2}Re \left[ \sqrt{E_t} \tilde{b} e^{jw_c(t-\tau)} \right. \\ &\quad \left. \cdot \int_{-\infty}^{\infty} \tilde{F}(jw) e^{jw(t-\tau)} \frac{dw}{2\pi} \right] \\ &= \sqrt{2}Re \left[ \sqrt{E_t} \tilde{b} e^{jw_c(t-\tau)} \tilde{f}(t-\tau) \right] \end{aligned} \quad (2.8)$$

but since we are treating  $\tilde{b}$  as a complex Gaussian random variable with uniform phase, we can absorb the term  $e^{-jw_c\tau}$  into it such that:

$$s_r(t) = \sqrt{2}Re \left[ \sqrt{E_t}\tilde{b}\tilde{f}(t - \tau)e^{jw_ct} \right]. \quad (2.9)$$

Van Trees adds the complex envelope  $\tilde{f}(t)$  of the transmitted signal  $s_t(t)$  at this point, no longer considering a continuous transmitted wave, and specifies that the envelope is normalized such that

$$\int_{-\infty}^{\infty} |\tilde{f}(t)|^2 dt = 1. \quad (2.10)$$

The preceding equations concern scenarios where there is zero-relative velocity between the transducer and the target. When this is no longer the case (when the target velocity  $v \neq 0$ ), Van Trees begins by stating that

$$R(t) = R_0 - vt \quad (2.11)$$

and that the received signal  $s_r(t)$  is

$$s_r(t) = \sqrt{2}Re \left[ \sqrt{E_t}\tilde{b}\tilde{f}(t - \tau(t))e^{jw_c(t - \tau(t))} \right] \quad (2.12)$$

where  $\tau(t)$  is the two-way travel time (expressed in Equation 2.14) from the transducer to the target and then back to the transducer. Van Trees defines  $R(t)$  as the instantaneous range to the target and  $R_0$  is the initial range to the target when  $t = 0$ , and continues by stating that a signal which is received at time  $t$  was reflected off of the target at time  $\left[ t - \frac{\tau(t)}{2} \right]$ . Therefore, at the time of reflection the target was at a range of

$$R \left( t - \frac{\tau(t)}{2} \right) = R_0 - v \cdot \left( t - \frac{\tau(t)}{2} \right) \quad (2.13)$$

and the two-way travel time  $\tau(t)$  is described by:

$$\tau(t) = 2 \frac{R \left( t - \frac{\tau(t)}{2} \right)}{c}. \quad (2.14)$$

Van Trees then states that for velocities of interest  $\frac{v}{c} \ll 1$ , and then plugs Equation 2.13 into Equation 2.14 to obtain

$$\tau(t) = \frac{2R_0}{c} - \frac{2vt}{c}. \quad (2.15)$$

If we then define the initial two-way travel time  $\tau_0 \equiv \frac{2R_0}{c}$  then we can make the substitution:

$$\tau(t) = \tau_0 - \frac{2vt}{c}. \quad (2.16)$$

Returning now to the expression for the returned signal  $s_r(t)$ , we substitute for  $\tau(t)$ :

$$s_r(t) = \sqrt{2} \operatorname{Re} \left[ \sqrt{E_t} \tilde{b} \tilde{f} \left( t - \tau_0 + \frac{2vt}{c} \right) e^{jw_c \left( t - \tau_0 + \frac{2vt}{c} \right)} \right] \quad (2.17)$$

$$= \sqrt{2} \operatorname{Re} \left[ \sqrt{E_t} \tilde{b} \tilde{f} \left( t - \tau_0 + \frac{2vt}{c} \right) e^{jw_c \left( t + \frac{2vt}{c} \right)} \right] \quad (2.18)$$

absorbing the  $e^{-jw_c \tau_0}$  term into  $\tilde{b}$ . Van Trees continues by stating that a non-zero velocity can affect the received signal in two ways: by lengthening or shortening the time scale of the envelope  $\tilde{f} \left( t - \tau_0 + \frac{2vt}{c} \right)$ , and by shifting the carrier frequency. The maximum change in the envelope is seen most easily when we let  $\frac{2vt}{c}$  go to its most extreme value, at the very end of the envelope when  $t = T_c$  (the envelope has a time-width of  $T_c$  seconds). For example, if choose a test pulse to be a 150-cycle monopulse at a carrier frequency of 300 kHz, then  $T_c = \frac{150}{300000} = 0.5$  ms. If  $v = 5$  m/s, which is approximately the greatest velocity that we are treating in this thesis, then the Doppler term in the envelope evaluates to  $\frac{2vT_c}{c} = \frac{2 \cdot 5 \cdot 0.0005}{1500} = 3.333 \cdot 10^{-6}$  seconds. In other words, the Doppler term compresses or enlarges the envelope by an amount less than 0.67% of  $T_c$ . We therefore neglect the Doppler shift term inside the envelope  $\tilde{f}$ . However, changes in the carrier frequency obey the Doppler relation  $w_D \equiv \frac{2v}{c} w_c$ , where small velocities now become important because they translate into large phase rotations. For instance, the same velocity of  $v = 5$  m/s results in a phase rotation of  $w_D = \frac{2 \cdot 5 \cdot 300000}{1500} = 2000$  radians, clearly enough to significantly affect  $s_r(t)$ . We now reach Van Trees' final expression for the received signal due to a reflection off of a slowly fluctuating point target:

$$s_r(t) = \sqrt{2} \operatorname{Re} \left[ \sqrt{E_t} \tilde{b} \tilde{f} \left( t - \tau_0 \right) e^{jw_c t + jw_D t} \right] \quad (2.19)$$

or in its analytic signal form:

$$\tilde{s}_r(t) = \sqrt{E_t} \tilde{b} \tilde{f}(t - \tau_0) e^{j w_D t}. \quad (2.20)$$

The interested reader could refer to either Burdic [7] or Mitchell [17] for supplementary information regarding the theory behind received sonar or radar signals.

Let us now expand upon Van Trees' work and develop expressions for the correlation between two received sonar signals. In doing so, an understanding of the velocity estimation methods (all of which rely upon some sort of correlation between received signals) is obtained. At this point, it is necessary to add a thermal noise term  $\tilde{n}(t)$  into our expression for the received signal.

Recalling the definition of a ping as being the process of transmitting the chosen waveform and listening to the resulting echoes, we seek to develop an expression for the signals received from subsequent pings. The analytic signal which is received from our slowly-fluctuating point target on pings 1 and 2 looks like this:

$$\tilde{s}_{r1}(t) = \sqrt{E_t} \tilde{b}_1 \tilde{f}(t - \tau_1) e^{j(w_D t - w_c \tau_1)} + \tilde{n}_1(t) \quad (2.21)$$

and

$$\tilde{s}_{r2}(t) = \sqrt{E_t} \tilde{b}_2 \tilde{f}(t - \tau_2) e^{j(w_D t - w_c \tau_2)} + \tilde{n}_2(t) \quad (2.22)$$

respectively, where  $\tilde{b}_1$  and  $\tilde{b}_2$  are the complex Gaussian random variables which model the collection of echoes returning from the individual point targets composing the seafloor,  $\tilde{f}$  is the transmitted envelope,  $\tau_1$  represents the two-way travel time to the target at the start of ping 1, and  $\tilde{n}_2(t)$  is the additive white Gaussian noise term for ping 2. Note that in Equation 2.18 we absorbed the exponential term  $e^{-j w_c \tau}$  into  $\tilde{b}$ , but must now take it back out because the two way travel time  $\tau$  will not be constant between pings if there is a relative velocity between the target and receiver. Also important is the time scale which is used: while both pings start at time  $t = 0$ , they were not taken at the same absolute time. Instead, we use time  $t$  as a relative time, referenced against the absolute time at which the ping was started. Once a ping has finished,  $t$  is reset and begins again from zero at the start of the next ping.

Notice also that we are assuming that the transmitted envelope does not change shape from one ping to the next. Since we have already assumed perfectly rectangular pulses (a common assumption, although not entirely accurate because of physical limitations on the

sonar system) it is reasonable to expect that  $\tilde{f}_1 = \tilde{f}_2$  since we are also assuming complete control over the number of cycles in each pulse. Again, we are assuming additive white Gaussian noise  $\tilde{n}(t)$  which is commonly used to model thermal noise in devices such as antennas or transducers.

The covariance for two random processes is defined as:

$$K_{xy} = E\{(x - E\{x\})(y - E\{y\})^*\} \quad (2.23)$$

where  $E\{x\}$  is defined as the ensemble expectation of  $x$ . In our case, we are modeling the seafloor using zero-mean Gaussian random variables, which means that the autocovariance

$$K_{\tilde{s}_1 \tilde{s}_1}(t, u) = E\{s_1(t)s_1^*(u) + n_1(t)s_1^*(u) + s_1(t)n_1^*(u) + n_1(t)n_1^*(u)\} \quad (2.24)$$

can be simplified because the signal and the noise are independent:  $E\{\tilde{s}(t)\tilde{n}^*(u)\} = 0$ . Recall that when introducing the complex Gaussian random variable,  $\tilde{b}$ , which represents the collection of point targets which contribute to the signal, we have already defined the variance to be  $E\{\tilde{b}\tilde{b}^*\} = 2\sigma_b^2$ . For the noise, let us assume that a wide bandpass filter is applied to the received signal such that the pulses (the signals) are essentially unaffected, but that the noise is bandlimited. A rectangular filter in the frequency domain  $rect\left(\frac{f}{2 \cdot BW}\right)$ , where the baseband signal is sent through a filter with width  $2 \cdot BW$ , corresponds to a *sinc* function in the correlation domain such that

$$E\{\tilde{n}_i(t)\tilde{n}_i^*(u)\} = 2N_0 \cdot BW \cdot sinc(2(t - u) \cdot BW). \quad (2.25)$$

We have taken the noise level to be  $N_0$ , and have taken  $2\sigma_n^2 = 2N_0 \cdot BW$ . We return to this noise term later, as we develop the correlation functions for the returning signal. Our autocovariance equation becomes:

$$K_{\tilde{s}_1 \tilde{s}_1}(t, u) = E\{s_1(t)s_1^*(u)\} + 2\sigma_n^2 \cdot sinc(2(t - u) \cdot BW) \quad (2.26)$$

$$\begin{aligned} &= E_t \tilde{f}(t - \tau_1) \tilde{f}^*(u - \tau_1) e^{j(w_D t - w_c \tau_1)} e^{-j(w_D u - w_c \tau_1)} E\{\tilde{b}\tilde{b}^*\} \\ &\quad + 2\sigma_n^2 \cdot sinc(2(t - u) \cdot BW) \end{aligned} \quad (2.27)$$

$$= 2E_t \sigma_b^2 \tilde{f}(t - \tau_1) \tilde{f}^*(u - \tau_1) e^{jw_D(t - u)} + 2\sigma_n^2 \cdot sinc(2(t - u) \cdot BW). \quad (2.28)$$

This expression implies that all the Doppler information for a slowly fluctuating point target contained in the autocovariance expression is in the exponential term  $e^{jw_D(t - u)}$ , where  $t - u$  represents the time shift between the signals that are being correlated.

If we instead cross-correlate the received time series from two separate pings (again, where our sole target is a point target) a different result is obtained. This time,

$$K_{\tilde{s}_1\tilde{s}_2}(t, u) = E \{s_1(t)s_2^*(u) + n_1(t)s_2^*(u) + s_1(t)n_2^*(u) + n_1(t)n_2^*(u)\} \quad (2.29)$$

which, because we are assuming additive white Gaussian noise and

$$E\{\tilde{n}_i(t)\tilde{n}_j^*(u)\} = 0 \quad (2.30)$$

for all  $i \neq j$ , allows us to express the covariance as:

$$K_{\tilde{s}_1\tilde{s}_2}(t, u) = E \{s_1(t)s_2^*(u)\} \quad (2.31)$$

$$= E_t \tilde{f}(t - \tau_1) \tilde{f}^*(u - \tau_2) e^{j(w_D t - w_c \tau_1)} e^{-j(w_D u - w_c \tau_2)} E\{\tilde{b}\tilde{b}^*\} \quad (2.32)$$

$$= 2E_t \sigma_b^2 \tilde{f}(t - \tau_1) \tilde{f}^*(u - \tau_2) e^{jw_D(t-u)} e^{jw_c(\tau_2 - \tau_1)}. \quad (2.33)$$

Let us call  $\tau_2 - \tau_1 = \Delta\tau$ , and note that it represents the difference in the two-way travel time experienced by the signal between pings 2 and 1. If  $\Delta\tau$  is multiplied by  $c$ , the speed of sound in water, the result represents twice the distance that the target has moved between pings. Mathematically, this relation is:

$$\frac{\Delta\tau c}{2} = -T_p v \quad (2.34)$$

where  $T_p$  is the time between pings, and  $v$  is the target's radial velocity (here we are taking a closing target to have a positive velocity). Therefore,

$$(\tau_2 - \tau_1) = \Delta\tau = -\frac{2v}{c} T_p. \quad (2.35)$$

We substitute this equation into 2.33 and recall our Doppler relation,  $w_D = w_c \frac{2v}{c}$ , to obtain:

$$K_{\tilde{s}_1\tilde{s}_2}(t, u) = 2E_t \sigma_b^2 \tilde{f}(t - \tau_1) \tilde{f}^*(u - \tau_2) e^{jw_D(t-u-T_p)}. \quad (2.36)$$

For easy comparison, let us now restate the two results for the auto and cross covariances between the received time series of echoes resulting from a point target:

$$K_{\tilde{s}_1\tilde{s}_1}(t, u) = 2E_t \sigma_b^2 \tilde{f}(t - \tau_1) \tilde{f}^*(u - \tau_1) e^{jw_D(t-u)} + 2\sigma_n^2 \cdot \text{sinc}(2(t-u) \cdot BW)$$

$$K_{\tilde{s}_1\tilde{s}_2}(t, u) = 2E_t \sigma_b^2 \tilde{f}(t - \tau_1) \tilde{f}^*(u - \tau_1 + \frac{2v}{c} T_p) e^{jw_D(t-u-T_p)}.$$

This comparison shows that we expect the covariance of separate pings to be more sensitive to motion than an autocovariance. At a fixed value of  $t - u$ , the covariance of  $\tilde{s}_1(t)$  and  $\tilde{s}_2(u)$  has a smaller "correlation window" where the two envelopes overlap and substantial correlation occurs, and has a greater phase difference from the exponential term.

### 2.2.2 Range-Spread Target

Now that we have finished developing our simplistic model of the target, let us develop a more realistic model through a similar procedure. Beginning with Van Trees' [25] model for range-spread targets which are not moving, we note that the received signal differs from that of a point target:

$$\tilde{s}(t) = \sqrt{E_t} \int_{L_0}^{L_1} \tilde{f}(t - \lambda) \tilde{b}_R(\lambda) d\lambda + \tilde{n}(t) \quad (2.37)$$

where the complex Gaussian random variable  $\tilde{b}(\lambda)$ , corresponding to scatterer amplitude and phase, is now a function of  $\lambda$ . We also note the addition of a thermal noise term  $\tilde{n}(t)$ . Van Trees has essentially divided an arbitrary range-spread target into tiny "scattering intervals" of  $d\lambda$ , with the returning signal being an integral over the length of the range-spread target (from  $L_0$  to  $L_1$ ). Essentially, we are summing up a large number of individual point targets of the sort described in the preceding Section. Note that both  $\lambda$  and  $L$  have units of seconds, but can be converted into meters by multiplying by the speed of sound.

Let us now extend the signal model to include range-spread targets which are moving. We write the expression for the return from a range-spread target as:

$$\tilde{s}(t) = \sqrt{E_t} \int_{L_0}^{L_1} \tilde{f}(t - \lambda) \tilde{b}_R(\lambda) e^{j(w_D t - w_c \lambda)} d\lambda + \tilde{n}(t) \quad (2.38)$$

where  $\lambda$  corresponds to the (time) location of each of the target's "scattering intervals" during the first ping. Here we have added an exponential term which includes the now non-zero Doppler term, as well as the term  $e^{-jw_c \lambda}$  which has been pulled out of  $\tilde{b}$  because a moving target is characterized by a  $\lambda$  which is a function of time, and cannot therefore be treated as a constant across pings. In other words, the location of each scattering interval on ping 1 is not necessarily the same as the location of each corresponding scattering interval on ping 2.

The autocovariance of two signals from the first ping is:

$$K_{\tilde{s}_1\tilde{s}_1}(t, u) = E \left[ E_t \int_{\Omega_L} d\lambda \tilde{f}(t - \lambda) \tilde{b}_R(\lambda) e^{j(w_D t - w_c \lambda)} \cdot \int_{\Omega_L} d\lambda_1 \tilde{f}^*(u - \lambda_1) \tilde{b}_R^*(\lambda_1) e^{-j(w_D u - w_c \lambda_1)} \right] + 2\sigma_n^2 \cdot \text{sinc}(2(t - u) \cdot BW). \quad (2.39)$$

The covariance of  $\tilde{b}_R$  is defined as  $\tilde{K}_{\tilde{b}_R}(\lambda, \lambda_1) = \delta(\lambda - \lambda_1) E[\tilde{b}_R(\lambda) \tilde{b}_R^*(\lambda_1)]$ , and we define the range-scattering function as  $S_R(\lambda) \equiv E[\tilde{b}_R(\lambda) \tilde{b}_R^*(\lambda)]$ . Physically, this means that we assume the scatterers at location  $\lambda$  to be uncorrelated with the scatterers at location  $\lambda_1$  if  $\lambda \neq \lambda_1$ , and that  $S_R(\lambda)$  represents the scattering strength of the scatterer(s) at location  $\lambda$ . We can use these relations to simplify 2.39 since the autocovariance for the received signals is non-zero (excluding thermal noise) only when  $\lambda = \lambda_1$ , and we therefore write:

$$K_{\tilde{s}_1\tilde{s}_1}(t, u) = E_t e^{jw_D(t-u)} \int_{-\infty}^{\infty} d\lambda \tilde{f}(t - \lambda) \tilde{S}_R(\lambda) \tilde{f}^*(u - \lambda) + 2\sigma_n^2 \cdot \text{sinc}(2(t - u) \cdot BW). \quad (2.40)$$

Since we have assumed that scattering strength is not a function of range,  $S_R(\lambda)$  is constant with respect to  $\lambda$ . We now have no more use for  $\lambda$ , so let us find a way to write our covariance function in terms of time  $t$  rather than in terms of  $\lambda$ . It is useful to introduce a couple of new terms at this time: the unitless integer  $k$  which represents a specific lag in the correlation function (for discrete signals), and the quantity  $kT_k = t - u$  which represents the time difference associated with that lag  $k$  and where  $T_k = 1/f_s$  is the inverse of the sampling frequency. In our case, the sampling frequency is equal to the carrier frequency  $f_c$ , but we'll avoid making this substitution at present. Our expression for the autocovariance is

$$K_{\tilde{s}_1\tilde{s}_1}(kT_k) = E_t S_R e^{jw_D(kT_k)} \int_{-\infty}^{\infty} d\lambda \tilde{f}(t - \lambda) \tilde{f}^*(t - kT_k - \lambda) + 2\sigma_n^2 \cdot \text{sinc}(2kT_k \cdot BW) \quad (2.41)$$

but we can simplify this further via substitution by setting  $z = t - \lambda$ . In doing so, we see that  $\frac{dz}{d\lambda} = -1$  and that  $d\lambda = -dz$ , and we can rewrite the expression for the autocovariance in terms of  $z$  rather than  $\lambda$ :

$$K_{\tilde{s}_1\tilde{s}_1}(kT_k) = -E_t S_R e^{jw_D kT_k} \int_{\infty}^{-\infty} dz \tilde{f}(z) \tilde{f}^*(z - kT_k) + 2\sigma_n^2 \cdot \text{sinc}(2kT_k \cdot BW). \quad (2.42)$$

Let us now switch the bounds on the integral, set  $z = t$ , and write our expression for the autocovariance in terms of the lag  $kT_k$ :

$$K_{\tilde{s}_1\tilde{s}_1}(kT_k) = E_t S_R e^{jw_D kT_k} \int_{-\infty}^{\infty} dt \tilde{f}(t) \tilde{f}^*(t - kT_k) + 2\sigma_n^2 \cdot \text{sinc}(2kT_k \cdot BW). \quad (2.43)$$

We have now found an expression for the autocovariance of the received signals which exposes all the information that is relevant to this analysis. The Doppler information, used to form velocity estimates, is seen to be contained in the exponential term alone - the phase of the autocovariance function is therefore a means by which to gather information about the velocity. The transmitted envelopes are seen to affect the amplitude of the received signal, and this integral is evaluated later to provide further details based on the transmit waveforms which are presently under consideration. Finally, thermal noise has been bandlimited in the frequency domain, which results in a *sinc* function in the time domain, implying that the contribution of noise to this covariance function is strongly lag-dependent.

We now switch our attention to finding the covariance between two separate pings for a range-spread target, extending Van Trees' theoretical foundations for our use. Now, instead of dealing with only  $\tilde{s}_1(t)$ , we are dealing with  $\tilde{s}_1(t)$  and  $\tilde{s}_2(t)$ :

$$K_{\tilde{s}_1\tilde{s}_2}(t, u) = E \left[ E_t \int_{\Omega_L} d\lambda \tilde{f}(t - \lambda) \tilde{b}_R(\lambda) e^{j(w_D t - w_c \lambda)} \cdot \int_{\Omega_L} d\lambda_1 \tilde{f}^*(u - \lambda_1) \tilde{B}_R^*(\lambda_1) e^{-j(w_D u - w_c \lambda_1)} \right]. \quad (2.44)$$

We are using the capital  $B$  to indicate that the second ping might come from scatterers which are in no way related to those of the first ping. Before we can simplify this equation further, we must find an expression for  $\lambda_1$  in terms of  $\lambda$ . As one may suspect, the relation we are after is indeed similar to 2.34:

$$\lambda_1 = \lambda - \frac{2v}{c} T_p. \quad (2.45)$$

Since  $\tilde{b}_R$  and  $\tilde{B}_R$  are the only random variables in the equation, and since Equation 2.44 is equal to zero when the arguments of  $\tilde{b}_R$  and  $\tilde{B}_R$  are not equal, by asserting 2.45 we may collapse this expression to a single integral and evaluate the expected value operation to

yield:

$$K_{\tilde{s}_1 \tilde{s}_2}(t, u) = E_t e^{j(w_D t - w_c \lambda)} e^{-j(w_D u - w_c \lambda + w_c \frac{2v}{c} T_p)} \cdot \int_{-\infty}^{\infty} d\lambda \tilde{f}(t - \lambda) S_R(\lambda) \tilde{f}^*(u - \lambda + \frac{2v}{c} T_p) \quad (2.46)$$

$$= E_t e^{j w_D (t - u - T_p)} \int_{-\infty}^{\infty} d\lambda \tilde{f}(t - \lambda) S_R(\lambda) \tilde{f}^*(u - \lambda + \frac{2v}{c} T_p). \quad (2.47)$$

Simplifying this expression further, by assuming that  $S_R(\lambda)$  is constant with respect to  $\lambda$ , and by then expressing the cross covariance as a function of lag we arrive at our final expression:

$$K_{\tilde{s}_1 \tilde{s}_2}(kT_k) = E_t S_R e^{j w_D (kT_k - T_p)} \int_{-\infty}^{\infty} dt \tilde{f}(t) \tilde{f}^*(t - kT_k + \frac{2v}{c} T_p). \quad (2.48)$$

As before, it is now convenient to restate our results for the auto- and cross-covariances between pings for a range-spread target:

$$K_{\tilde{s}_1 \tilde{s}_1}(kT_k) = E_t S_R e^{j w_D kT_k} \int_{-\infty}^{\infty} dt \tilde{f}(t) \tilde{f}^*(t - kT_k) + 2\sigma_n^2 \cdot \text{sinc}(2kT_k \cdot BW)$$

$$K_{\tilde{s}_1 \tilde{s}_2}(kT_k) = E_t S_R e^{j w_D (kT_k - T_p)} \int_{-\infty}^{\infty} dt \tilde{f}(t) \tilde{f}^*(t - kT_k + \frac{2v}{c} T_p).$$

Let us return now to discuss the thermal noise term which is included in the expression for the autocovariance. If we set the width of our rectangular filter to be quite wide (in the frequency domain), say a width of  $2 \cdot BW = 300000$  Hz, then we have bandlimited the noise. In fact, when we return to the *sinc* function in the correlation domain, we note that it has its first zero when  $2kT_k \cdot BW = \pm 1$ , or when  $k = \pm 1$ . Beyond this lag, the contribution from the thermal noise to the autocovariance will henceforth be neglected. The signal, represented as a *sinc* function in the frequency domain, has a width of approximately 50000 Hz - and passes through this filter essentially unaltered. The width of this filter has been arbitrarily chosen, and is used simply to establish that it is possible to bandlimit the noise in such a way as to leave the signal essentially unaffected while neglecting the contribution of noise to the covariance function past a lag of 1.

## 2.3 Signal Models

Our objective is the estimation of target velocity, and we have just captured the "essence" of this problem in the covariance functions, but our discussion would not be complete without considering the nature of the transmitted envelopes. A more detailed discussion of these envelopes - and the approximation that they are rectangular in nature - must now be presented.

Although in "real life" the transmitted envelopes are not rectangular, and have rising/falling edges which are not infinitely steep, it is nonetheless a reasonable approximation to consider these pulses to be rectangular for the present thesis. This is because we can still consider all of the fundamental aspects of the problem without needing to add the additional complexity of precisely defining the pulses. Modeling our transmitted pulses as rectangular does not affect our ability to discuss the effectiveness of these VEMs at accomplishing their goals (velocity estimation) - however, attempting to describe these pulses in infinite detail would add layers of complexity to the problem while not substantially affecting the end result.

Making the assumption that all transmitted pulses are rectangular in nature, we proceed to describe the envelope function  $\tilde{f}(t)$  in general terms which can then be used to define both the monopulse and pulse pair waveforms. Let us first define the *rect* function as

$$\text{rect}\left(\frac{t}{\beta}\right) \equiv u\left(t + \frac{\beta}{2}\right) - u\left(t - \frac{\beta}{2}\right) \quad (2.49)$$

and

$$\text{rect}\left(\frac{t-t'}{\beta}\right) = u\left(t-t' + \frac{\beta}{2}\right) - u\left(t-t' - \frac{\beta}{2}\right) \quad (2.50)$$

where  $u(t)$  is the Heaviside step function,  $\beta$  is the time-width of the pulse, and  $t'$  serves to offset (or time-shift) the *rect* function from symmetry about time  $t = 0$ .

Let us now define the triangular function as the convolution of two scaled rectangular functions

$$\text{tri}\left(\frac{t}{\beta}\right) \equiv \frac{1}{\beta} \cdot \left( \text{rect}\left(\frac{t}{\beta}\right) \otimes \text{rect}\left(\frac{t}{\beta}\right) \right) \quad (2.51)$$

$$= \begin{cases} 1 - \frac{|t|}{\beta} & |t| \leq \beta \\ 0 & |t| > \beta \end{cases} \quad (2.52)$$

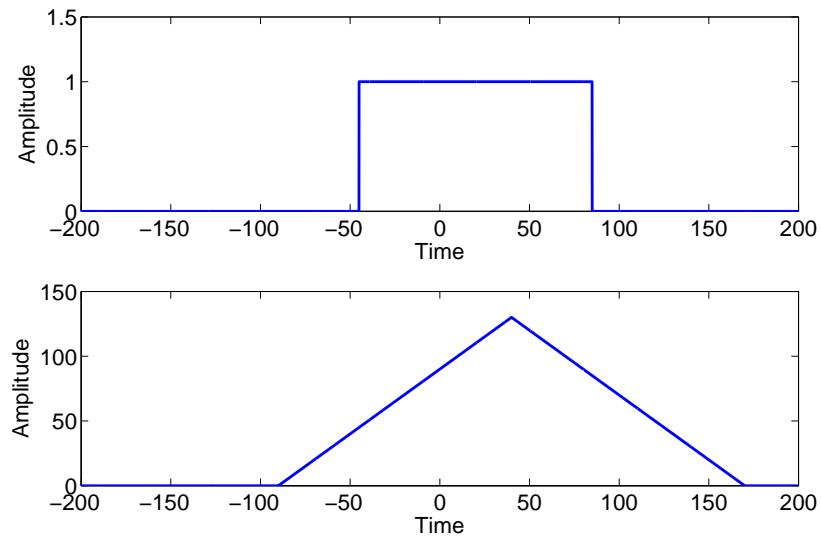


Figure 2.5: A rectangular function (top) is convolved with itself to yield a triangular function (bottom). The *rect* function is 130 time units wide, and is offset from symmetry about the y-axis by 20 time units. The corresponding *tri* function is 260 time units wide, and is offset from symmetry about the y-axis by 40 time units.

such that our definition is in agreement with the accepted standard (also discussed in [8]). The reader will note that since the rectangular envelopes are equal to their conjugate images (in other words,  $f(t - kT_k) = f^*(kT_k - t)$ ) the terms "correlation" and "convolution" may be used interchangeably. Furthermore, the tilde may henceforth be dropped from the  $f(t)$  term because we define our envelopes in terms of *rect* functions, which are not complex.

Figure 2.5 shows a rectangular function (top plot) of time-width  $\beta = 130$  units centered about time  $t' = 20$  units. When convolved with itself, this *rect* function yields a *tri* function (bottom plot) centered about  $t' = 40$  units, and of time-width  $2\beta = 260$  units. At its peak, the amplitude of the *tri* function is equal to  $\beta = 130$  because the *rect* functions are not scaled. Recall that we have already assumed (Equation 2.10) that

$$\int_{-\infty}^{\infty} |\tilde{f}(t)|^2 dt = 1,$$

so our first task after defining the monopulse and pulse pair is to introduce the correct normalization factors for each pulse. This normalization is dealt with in the following Subsections, for the monopulse and pulse pair individually. Once we have found the normalized envelope functions for both waveforms, we take these expressions and find solutions to the integrals in Equations 2.43 and 2.48.

In practice, we will be considering the discrete correlation of these envelope functions, and for that reason we express  $tri(kT_k)$  in terms of the lag  $k$  and sampling period  $T_k$ . If the envelopes are stretched by  $k_p T_s = \beta$ , corresponding to the number of cycles in each pulse  $k_p$  multiplied by the period of the carrier  $T_s$  then our *tri* function assumes the form

$$tri\left(\frac{kT_k}{k_p T_s}\right) = \left[ \frac{1}{\sqrt{k_p T_s}} rect\left(\frac{kT_k}{k_p T_s}\right) \right] \otimes \left[ \frac{1}{\sqrt{k_p T_s}} rect\left(\frac{kT_k}{k_p T_s}\right) \right] \quad (2.53)$$

$$= \left(1 - \frac{|kT_k|}{k_p T_s}\right) rect\left(\frac{kT_k}{2k_p T_s}\right) \quad (2.54)$$

We may now use these tools to describe the monopulse and pulse pair transmit waveforms.

### 2.3.1 Monopulse Waveform

Let us first consider the case of a monopulse as the transmitted waveform. The aforementioned *rect* function is stretched or compressed by constant  $\beta$ , and can be offset from symmetry about time  $t = 0$  by constant  $t'$  if desired. We define the un-normalized envelope

function for a monopulse be

$$f_m(t) = \text{rect}\left(\frac{t}{\beta}\right), \quad (2.55)$$

and when we evaluate the integral

$$\int_{-\infty}^{\infty} |f_m(t)|^2 dt = \int_{-\infty}^{\infty} \left| \text{rect}\left(\frac{t}{\beta}\right) \right|^2 dt = \beta \quad (2.56)$$

we observe that an envelope normalization factor of  $\frac{1}{\sqrt{\beta}}$  is required. A normalized monopulse envelope function is therefore

$$f_m(t) = \frac{1}{\sqrt{\beta}} \cdot \text{rect}\left(\frac{t}{\beta}\right). \quad (2.57)$$

Solving the integral in Equation 2.43, we see that

$$\int_{-\infty}^{\infty} dt f(t) f^*(t - kT_k) = \frac{1}{k_p T_s} \cdot \int_{-\infty}^{\infty} \text{rect}\left(\frac{t}{k_p T_s}\right) \text{rect}\left(\frac{t - kT_k}{k_p T_s}\right) dt \quad (2.58)$$

$$= \text{tri}\left(\frac{kT_k}{k_p T_s}\right) \quad (2.59)$$

$$= \left(1 - \frac{|kT_k|}{k_p T_s}\right) \text{rect}\left(\frac{kT_k}{2k_p T_s}\right) \quad (2.60)$$

If we instead cross correlate two separate pings, as in Equation 2.48, the solution would be:

$$\int_{-\infty}^{\infty} dt f(t) f^*(t - kT_k + \frac{2v}{c} T_p) = \frac{1}{k_p T_s} \cdot \int_{-\infty}^{\infty} \text{rect}\left(\frac{t}{k_p T_s}\right) \text{rect}\left(\frac{t - kT_k + \frac{2v}{c} T_p}{k_p T_s}\right) dt \quad (2.61)$$

$$= \text{tri}\left(\frac{kT_k + \frac{2v}{c} T_p}{k_p T_s}\right) \quad (2.62)$$

$$= \left(1 - \frac{|kT_k + \frac{2v}{c} T_p|}{k_p T_s}\right) \text{rect}\left(\frac{kT_k + \frac{2v}{c} T_p}{2k_p T_s}\right). \quad (2.63)$$

### 2.3.2 Pulse Pair Waveform

In the case of a pulse pair, we transmit two *rect* functions in the single ping. Recall that  $\beta$  symbolizes the length of each pulse, and is not necessarily the same for a monopulse as for a pulse pair. In this thesis, our test pulse pair is such that  $\beta = 30$  time units so each pulse is 30 cycles long. Furthermore, recall that for the pulse pair we have previously introduced

the terms  $\beta = k_p T_s$  (time-length of each pulse) and  $k_s T_s$  (the dead time between pulses). These terms combine to yield the total time separation between the head of the first pulse and the head of the second pulse:  $k_p T_s + k_s T_s$ . Let us adjust  $t'$  such that our expression for the total envelope (two pulses) is centered about zero, rather than just having the first pulse be centered around zero. We therefore set  $t' = (k_p T_s + k_s T_s)/2$ .

An un-normalized pulse pair is therefore mathematically described by

$$f_{pp}(t) = f\left(\frac{t-t'}{\beta}\right) + f\left(\frac{t+t'}{\beta}\right) \quad (2.64)$$

$$= \text{rect}\left(\frac{t-t'}{\beta}\right) + \text{rect}\left(\frac{t+t'}{\beta}\right). \quad (2.65)$$

Applying the normalization condition (Equation 2.10) and evaluating the integral

$$\int_{-\infty}^{\infty} |f_{pp}(t)|^2 dt = \int_{-\infty}^{\infty} \left| \text{rect}\left(\frac{t-t'}{\beta}\right) + \text{rect}\left(\frac{t+t'}{\beta}\right) \right|^2 dt = 2\beta \quad (2.66)$$

we see that we must normalize  $f_{pp}(t)$  by a factor of  $\frac{1}{\sqrt{2\beta}}$  in order to meet the normalization condition. The normalized pulse pair envelope function is therefore

$$f_{pp}(t) = \frac{1}{\sqrt{2\beta}} \cdot \left( \text{rect}\left(\frac{t-t'}{\beta}\right) + \text{rect}\left(\frac{t+t'}{\beta}\right) \right). \quad (2.67)$$

The normalized envelope functions for the monopulse and pulse pair waveforms are restated here for easy comparison:

$$f_m(t) = \frac{1}{\sqrt{\beta}} \cdot \text{rect}\left(\frac{t}{\beta}\right)$$

$$f_{pp}(t) = \frac{1}{\sqrt{2\beta}} \cdot \left( \text{rect}\left(\frac{t-t'}{\beta}\right) + \text{rect}\left(\frac{t+t'}{\beta}\right) \right).$$

It is important to remember that  $\beta$  is not necessarily the same when the above normalization formulas are applied; we should not assume that the monopulse will have the same time-length as each pulse in the pulse pair.

Continuing, we find the integral in Equation 2.43 for the pulse pair to be:

$$\begin{aligned} \int_{-\infty}^{\infty} dt f(t) f^*(t - kT_k) &= \frac{1}{2k_p T_s} \cdot \int_{-\infty}^{\infty} \left[ \text{rect} \left( \frac{t - (k_p T_s + k_s T_s)/2}{k_p T_s} \right) \right. \\ &\quad \left. + \text{rect} \left( \frac{t + (k_p T_s + k_s T_s)/2}{k_p T_s} \right) \right] \\ &\quad \cdot \left[ \text{rect} \left( \frac{t - (k_p T_s + k_s T_s)/2 - kT_k}{k_p T_s} \right) \right. \\ &\quad \left. + \text{rect} \left( \frac{t + (k_p T_s + k_s T_s)/2 - kT_k}{k_p T_s} \right) \right] dt \end{aligned} \quad (2.68)$$

$$\begin{aligned} &= \left[ \frac{1}{2} \cdot \text{tri} \left( \frac{kT_k + k_p T_s + k_s T_s}{k_p T_s} \right) \right. \\ &\quad \left. + \text{tri} \left( \frac{kT_k}{k_p T_s} \right) \right. \\ &\quad \left. + \frac{1}{2} \cdot \text{tri} \left( \frac{kT_k - k_p T_s - k_s T_s}{k_p T_s} \right) \right]. \end{aligned} \quad (2.69)$$

This implies a three-peaked structure, where the side peaks are located at  $\pm 2 \cdot t' = \pm(k_p T_s + k_s T_s)$  and are  $2 \cdot \beta = 2k_p T_s$  in width. If instead we find the cross covariance between two pings, we would expect a similar three-peaked structure, but would observe that the entire structure were translated by an amount corresponding to the time between pings  $T_p$  and

the velocity  $v$  of the target. Solving the integral in Equation 2.48 we obtain the solution:

$$\begin{aligned}
\int_{-\infty}^{\infty} dt f(t) f^*(t - kT_k + \frac{2v}{c}T_p) &= \frac{1}{2k_p T_s} \cdot \int_{-\infty}^{\infty} \left[ \text{rect} \left( \frac{t - (k_p T_s + k_s T_s)/2}{k_p T_s} \right) \right. \\
&\quad \left. + \text{rect} \left( \frac{t + (k_p T_s + k_s T_s)/2}{k_p T_s} \right) \right] \\
&\quad \cdot \left[ \text{rect} \left( \frac{t - (k_p T_s + k_s T_s)/2 - kT_k + \frac{2v}{c}T_p}{k_p T_s} \right) \right. \\
&\quad \left. + \text{rect} \left( \frac{t + (k_p T_s + k_s T_s)/2 - kT_k + \frac{2v}{c}T_p}{k_p T_s} \right) \right] dt \quad (2.70) \\
&= \left[ \frac{1}{2} \cdot \text{tri} \left( \frac{kT_k + \frac{2v}{c}T_p + k_p T_s + k_s T_s}{k_p T_s} \right) \right. \\
&\quad \left. + \text{tri} \left( \frac{kT_k + \frac{2v}{c}T_p}{k_p T_s} \right) \right. \\
&\quad \left. + \frac{1}{2} \cdot \text{tri} \left( \frac{kT_k + \frac{2v}{c}T_p - k_p T_s - k_s T_s}{k_p T_s} \right) \right]. \quad (2.71)
\end{aligned}$$

Figure 2.6 shows a pulse pair (top) composed to two rectangular functions and centered about the  $y$ -axis convolved with itself to yield a three-peaked structure (bottom). The *rect* functions, each 30 time units in length and separated from each other by 35 units of dead time, give way to *tri* functions as a result of their correlation. Each *tri* function is twice as wide as either of the *rect* functions, with the side peaks being centered about  $\pm 65$  time units - twice that of the *rect* functions. The central peak results from the correlation of the un-normalized *rect* functions in the pulse pair, and is seen to have a maximum height at time  $t = 0$  of 60, equal to twice the width of each *rect* function. The side peaks result from the correlation of only one set of the un-normalized pulses in the pair, thus the side peaks have a maximum height of half this value.

Let us restate our solutions to the integrals in Equations 2.43 and 2.48, which may now be substituted directly into the covariance functions. If a normalized monopulse is

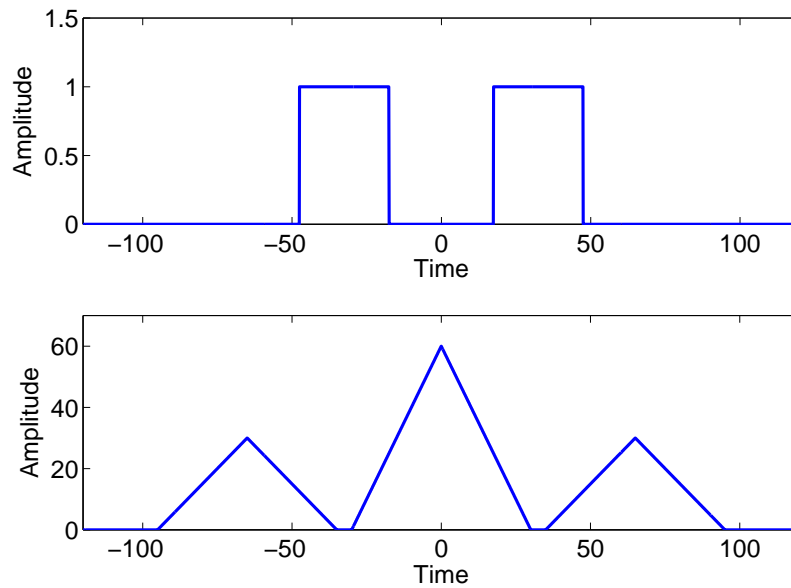


Figure 2.6: A pulse pair (top) centered about the  $y$ -axis is convolved with itself to yield a three-peaked triangular structure (bottom). The un-normalized *rect* functions composing the pulse pair are each 30 time units wide, and each of the corresponding *tri* functions are 60 time units wide, and are also centered about the  $y$ -axis.

transmitted, we observe the solutions

$$f_m(t) \otimes f_m(t) = \text{tri} \left( \frac{kT_k}{k_p T_s} \right)$$

$$f_m(t) \otimes f_m\left(t + \frac{2v}{c} T_p\right) = \text{tri} \left( \frac{kT_k + \frac{2v}{c} T_p}{k_p T_s} \right)$$

for an autocorrelation and cross correlation, respectively. Similarly, for the normalized pulse pair, we observe the following solutions:

$$\begin{aligned} f_{pp}(t) \otimes f_{pp}(t) &= \left[ \frac{1}{2} \cdot \text{tri} \left( \frac{kT_k + k_p T_s + k_s T_s}{k_p T_s} \right) \right. \\ &\quad + \text{tri} \left( \frac{kT_k}{k_p T_s} \right) \\ &\quad \left. + \frac{1}{2} \cdot \text{tri} \left( \frac{kT_k - k_p T_s - k_s T_s}{k_p T_s} \right) \right] \end{aligned}$$

$$\begin{aligned} f_{pp}(t) \otimes f_{pp}\left(t + \frac{2v}{s} T_p\right) &= \left[ \frac{1}{2} \cdot \text{tri} \left( \frac{kT_k + \frac{2v}{c} T_p + k_p T_s + k_s T_s}{k_p T_s} \right) \right. \\ &\quad + \text{tri} \left( \frac{kT_k + \frac{2v}{c} T_p}{k_p T_s} \right) \\ &\quad \left. + \frac{1}{2} \cdot \text{tri} \left( \frac{kT_k + \frac{2v}{c} T_p - k_p T_s - k_s T_s}{k_p T_s} \right) \right]. \end{aligned}$$

### 2.3.3 Noise

Let us explore further the nature of the noise which exists in our received signal. We seek to expand our description of the covariance functions at a specific lag in terms of signal and noise, which will later assist with our calculation of the Cramer-Rao lower bound (CRLB). Although the development of the CRLB is left for later in this Chapter, the development of the signal model is completed presently.

So far, we have only considered the contribution of thermal noise which can lead to a decorrelation of signals between samples. However, thermal noise alone cannot explain all

of the decorrelation which can occur between two samples of a signal. We seek to develop our signal model slightly, by decomposing the returning signal into a correlated component and an uncorrelated component, in addition to the already present additive thermal noise term. With this more descriptive signal model, we also introduce new models for the signal to noise ratio. The following development is taken from Bird and Mullins [3].

We are considering the case where two separate time samples are correlated, and where there exists a component of each signal which is common between samples. Let the received signals from these two time samples be modeled as

$$\tilde{s}_1 = \tilde{s}_c + \tilde{N}_1 + \tilde{n}_1 \quad (2.72)$$

and

$$\tilde{s}_2 = \tilde{s}_c + \tilde{N}_2 + \tilde{n}_2 \quad (2.73)$$

where  $\tilde{s}_c$  represents the portion of returning signal which is correlated between samples, where  $\tilde{N}$  represents the portion of returning signal which is uncorrelated between samples (resulting from different footprints) and where  $\tilde{n}$  represents the additive noise, which is independent from the transmitted signal. If we seek to find the power ratio of the returning signal which is *correlated* between samples to the returning signal which is *uncorrelated* between samples, then it is simply

$$snr_c = \frac{2\sigma_{sc}^2}{2\sigma_N^2}. \quad (2.74)$$

or, expressed in units of dB:

$$SNR_c = 10 \cdot \log(snr_c). \quad (2.75)$$

Likewise, the ratio of returning signal power to thermal noise power is then

$$snr_n = \frac{2\sigma_{sc}^2 + 2\sigma_N^2}{2\sigma_n^2} = \frac{2\sigma_s^2}{2\sigma_n^2} \quad (2.76)$$

where  $2\sigma_s^2 = E_t S_R$  is the total power of the signal. We can also calculate the associated correlation coefficients as

$$\rho_c = \frac{snr_c}{1 + snr_c} \quad (2.77)$$

and

$$\rho_n = \frac{snr_n}{1 + snr_n}. \quad (2.78)$$

Here,  $\rho_c$  represents the correlation coefficient associated with the signal in the absence of noise, and  $\rho_n$  represents the correlation coefficient associated with the total signal (both the correlated and uncorrelated components) with respect to the thermal noise. These are taken from the correlation functions, and are given further consideration when the discussion of the CRLB is presented.

Because  $\rho_c$  and  $\rho_n$  have some dependence upon the time separation between the two samples which are being correlated, we may choose to express them both as a function of lag  $\rho(kT_k)$ . The concept of an effective SNR is now convenient to introduce, which takes into account both of the potential sources of decorrelation (thermal noise, and "decorrelation noise" or interference from the portion of the returning signal which is uncorrelated). The correlation functions may be represented as the product of the aforementioned correlation coefficients (plus a phase term, see [3]) after some manipulation. We therefore define the effective correlation coefficient as

$$\rho_e \equiv \rho_n(kT_k) \cdot \rho_c(kT_k) \quad (2.79)$$

and the effective SNR is

$$snr_e = \frac{\rho_e}{1 - \rho_e} \quad (2.80)$$

from which it is easy to obtain the general expression in terms of  $snr_n$  and  $snr_c$ :

$$snr_e = \frac{snr_n(kT_k) \cdot snr_c(kT_k)}{1 + snr_n(kT_k) + snr_c(kT_k)}. \quad (2.81)$$

This relatively simple mathematical development helps us to gain some insight into the factors which influence decorrelation between samples. We see that the effective SNR (taking into account both thermal noise and any noise which results from a replacement of scatterers) is going to be dominated by whichever SNR is the lower. We can conclude that having a good velocity estimate depends not only on having one SNR high, but upon having both SNRs as high as possible.

Having developed our mathematical models for the auto-and cross-covariance of pings from a range-spread target moving at velocity  $v$  relative to the transducer, and having

developed more in-depth models of both the transmitted signal and the noise inherent in the system, we first summarize the correlation functions that have been developed thusly, and then turn our attention to the velocity estimation methods.

### 2.3.4 Final Expressions for Covariance Functions

We may now employ the results of the preceding developments to substitute triangular functions in place of the integrals in Equations 2.43 and 2.48, or to express the covariance functions more generally in terms of correlation coefficients. Specifically, if a monopulse is transmitted we can expect the auto- and cross covariance functions, respectively, to be:

$$K_{\tilde{s}_1\tilde{s}_1}(kT_k) = E_t S_R e^{jw_D kT_k} \text{tri}\left(\frac{kT_k}{k_p T_s}\right) + 2\sigma_n^2 \cdot \text{sinc}(2kT_k \cdot BW) \quad (2.82)$$

$$K_{\tilde{s}_1\tilde{s}_2}(kT_k) = E_t S_R e^{jw_D(kT_k - T_p)} \text{tri}\left(\frac{kT_k + \frac{2v}{c} T_p}{k_p T_s}\right). \quad (2.83)$$

Here we can easily note the differences between single ping and ping pair monopulse velocity estimate methods. When only a single ping is used, the triangle in the autocovariance function is centered at zero and has zero phase at this center, plus additive white Gaussian noise. If two pings are used as a pair, then the location of the triangle moves away from zero-lag depending upon the target's velocity - and may very well have a non-zero phase at its center, but due to the uncorrelated nature of thermal noise across pings there is no additive noise present in the (theoretical) covariance.

If a pulse pair were transmitted, then the resulting auto and cross covariance functions

contain three triangular functions rather than only one:

$$\begin{aligned}
K_{\tilde{s}_1\tilde{s}_1}(kT_k) &= E_t S_R e^{jw_D kT_k} \\
&\cdot \left[ \frac{1}{2} \text{tri} \left( \frac{kT_k + k_s T_s + k_p T_s}{k_p T_s} \right) + \text{tri} \left( \frac{kT_k}{k_p T_s} \right) \right. \\
&\left. + \frac{1}{2} \text{tri} \left( \frac{kT_k - k_s T_s - k_p T_s}{k_p T_s} \right) \right] + 2\sigma_n^2 \cdot \text{sinc}(2kT_k \cdot BW)
\end{aligned} \tag{2.84}$$

for the autocovariance, and

$$\begin{aligned}
K_{\tilde{s}_1\tilde{s}_2}(kT_k) &= E_t S_R e^{jw_D(kT_k - T_p)} \\
&\cdot \left[ \frac{1}{2} \text{tri} \left( \frac{kT_k + k_s T_s + k_p T_s + \frac{2v}{c} T_p}{k_p T_s} \right) + \text{tri} \left( \frac{kT_k + \frac{2v}{c} T_p}{k_p T_s} \right) \right. \\
&\left. + \frac{1}{2} \text{tri} \left( \frac{kT_k - k_s T_s - k_p T_s + \frac{2v}{c} T_p}{k_p T_s} \right) \right]
\end{aligned} \tag{2.85}$$

for the cross covariance. As with the monopulse, a non-zero target velocity shifts the location of the peaks in the cross covariance function. Once again, we see that the phase in the center of the autocovariance function is zero regardless of target velocity (and excluding any effects caused by thermal noise) but that the phase in the side peaks of the autocovariance function is non-zero if the target is moving at a non-zero velocity. These differences between covariance functions are discussed later, as we investigate the VEMs themselves and seek to compare them to one-another.

Let us set  $\rho_{c,a}(kT_k)$  equal to the *tri* function in the autocovariance, set  $\rho_{c,c}(kT_k)$  equal to the *tri* function for the cross covariance, and set  $\rho_n(kT_k)$  equal to  $\text{sinc}(2kT_k \cdot BW)$ . We

may now express the monopulse covariance functions as

$$K_{\tilde{s}_1 \tilde{s}_1}(kT_k) = E_t S_R \rho_{c,a}(kT_k) e^{jw_D kT_k} + 2\sigma_n^2 \cdot \rho_n(kT_k) \quad (2.86)$$

$$K_{\tilde{s}_1 \tilde{s}_2}(kT_k) = E_t S_R \rho_{c,c}(kT_k) e^{jw_D(kT_k - T_p)}. \quad (2.87)$$

This procedure could be repeated for the pulse pair, but the only difference in the answer would be that we would use different subscripts to denote that  $\rho_c(kT_k)$  now represents the sum of *tri* functions for either the auto or cross covariances. For this reason, we omit this development.

The more condensed correlation functions developed above become useful when calculating the CRLB. However, due to their less explicit nature (not precisely stating the result of the covariance of the envelope functions), we revert back to the more explicit forms of these covariance functions for the following Section. We now turn our attention to the velocity estimation methods themselves, and attempt to describe them in terms of the covariance functions.

## 2.4 Velocity Estimation Methods

Having now described the waveforms which are transmitted by the sonar system, and then describing the targets off of which they reflect, it is time to describe in detail the methods by which velocity estimates are obtained. The performance of these velocity estimation methods (VEMs) has some dependence upon the transmit waveform with which they are coupled, and for this reason many permutations (waveform/VEM pairs) must be considered. The methods to be considered are the ping pair incoherent method, the ping pair covariance method, and the single ping covariance method.

Figure 2.7 provides a diagram of the VEMs which are about to be described mathematically, and how they relate to their respective transmit waveforms. The first such transmit waveform, the monopulse, produces velocity estimates using either a single ping or a ping pair. If a single ping is to be used in processing, then covariance processing is used to produce the velocity estimates. If a ping pair is to be used in processing, then we may choose

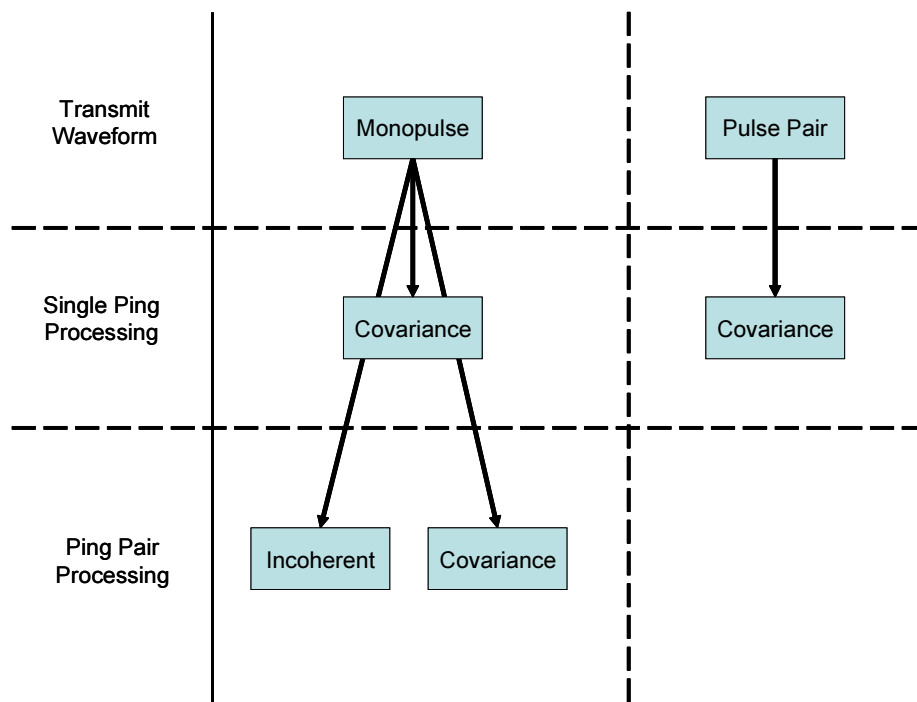


Figure 2.7: The various velocity estimation methods (VEMs) which are under consideration in this thesis.

between processing the returns incoherently, or to use the covariance (coherent) method instead. If a pulse pair is the transmitted waveform, then we are only considering single ping covariance processing as the means by which to obtain velocity estimates.

### 2.4.1 Monopulse Methods

For a monopulse as the transmit waveform, two of the estimation methods under consideration require that at least two pings be used before a single velocity profile is made. These methods are the ping pair incoherent, and ping pair covariance VEM. In general terms, most VEMs operate by making a number of observations of some target and then comparing changes in these observations; two-point estimation is where two such observations are compared. Single-ping VEMs take these multiple observations from within only one ping (such as the single ping covariance method), but in the case of the incoherent and the ping pair covariance method this is not the case - the two observations are taken from separate pings. Once each VEM has been described, attention is then turned towards evaluating the theoretical limits on estimator performance by developing the Cramer-Rao lower bound (CRLB) for each waveform.

#### Ping Pair Incoherent

The first VEM which is under consideration is an "older" technique, which does not require the sonar system to be ping to ping coherent. Ping to ping incoherent velocity estimation is essentially the process of correlating the magnitude of the time series of received signals from the first ping with the magnitude of the time series of received signals in the second ping, and does not use phase information to produce a velocity estimate. In the case where the relative velocity between the boat and scatterer is zero and where noise levels are low, the covariance between one ping and a subsequent ping is high at any given range bin because the reflection involves returns produced by the same scatterers in both pings. The shape of the covariance function in this case is a triangle centered at zero lag (for a square pulse, and no relative velocity between target and receiver). In the case where the velocity is non-zero, this triangle is offset to a non-zero lag which corresponds to the mean relative velocity of the scatterer(s).

Note also that this method works best when the aspect angle with respect to the scatterers is fairly constant. If the boat is traveling too quickly over the seafloor, then the

transducer is "looking down" at each scatterer from a different aspect angle, and from a different angle each scatterer may produce a different return. This method eventually begins to break down as the aspect angle changes too quickly with high boat speeds or unfavorable geometries.

Before estimates are obtained, the system operator must first specify the range bin size, or equivalently the number of time samples. The terms "range bin size" and "number of time samples" may be used interchangeably in this case, because the specification of some interval within the received time series corresponds to a physical range interval. It is easy to understand that under ideal conditions any stationary (non-moving) scatterer which becomes ensonified should contribute an echo which has a duration equal to the duration of the envelope.

Let us now describe this method mathematically, in terms of the covariance function. We seek to cross correlate the magnitudes of two received time series

$$K_{|\tilde{s}_1||\tilde{s}_2|}(t, u) = E \left\{ E_t \left| \int_{\Omega_L} d\lambda \tilde{f}(t - \lambda) \tilde{b}_R(\lambda) \right| \cdot \left| \int_{\Omega_L} d\lambda_1 \tilde{f}^*(u - \lambda_1) \tilde{B}_R^*(\lambda_1) \right| \right\}. \quad (2.88)$$

where  $\lambda_1$  is being used here to signify that the spatial location of the target is not the same in ping 2 as it was in ping 1. This equation is difficult to manipulate, and is left in its present form.

It is plain to see that the evaluation of this expression is non-trivial, however it is still possible to consider the behavior of this covariance function by employing our knowledge of the more well-behaved covariance functions. We know that when we correlate two *rect* functions the result is a *tri* function, so the final answer assumes a form similar to that of a triangle. As usual, this covariance function is normalized to 1, and it attains this value only when a complete "amplitude overlap" is found between a portion of the reference signal  $|\tilde{s}_1(t)|$  with a corresponding portion of  $|\tilde{s}_2(t)|$ .

Figure 2.8 shows this basic idea with two sample waveforms. The top plot is a random series of numbers (normally distributed) representing  $|\tilde{s}_1(t)|$ , while the middle plot contains a shifted version of the first waveform plus five-hundred new random samples and represents  $|\tilde{s}_2(t)|$ . Additive Gaussian noise is added in both cases (note that the noise is independent between these two waveforms). The lower plot is the covariance of these two waveforms, with a peak occurring at a lag of  $k = 500$  and reaching a value of  $\approx 0.63$ . Both signals have

been convolved with a 5-cycle square pulse, which allows for a clearly-defined peak to be formed at the point of greatest correlation.

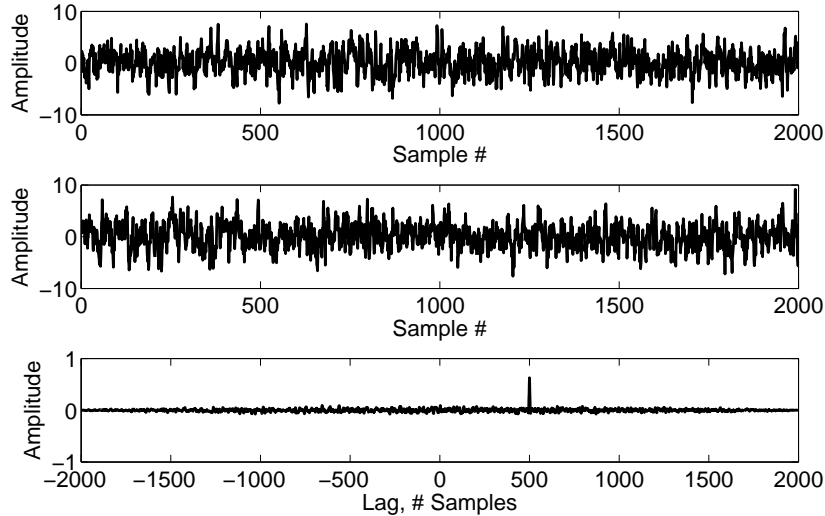


Figure 2.8: Incoherent cross covariance of two waveforms. The first waveform (top) is a random series of numbers (the signal) buried in additive noise, while the second waveform (middle) contains a shifted version of the first signal (shifted by 500 samples) plus five hundred new random samples (also buried in additive noise). The bottom graph represents the covariance of these two waveforms, with the peak at a value of  $\approx 0.63$ , occurring at a lag of  $k = 500$ .

Assuming that a high correlation exists between the two pings, such as in Figure 2.8, the first step of the velocity estimation method is to locate the position (the lag  $k$ ) which maximizes the covariance function. We expect that the peak of the covariance function occurs when the two envelopes overlap the most, or when  $kT_k = \frac{2v}{c}T_p$ . Solving for  $v$ , we can now calculate the target's velocity based on the estimate of its motion between pings (the lag at which the peak in the covariance function occurs) and the time between pings:

$$\hat{v} = \frac{kT_k c}{2T_p}. \quad (2.89)$$

It is common in practice to not seek a single velocity estimate per ping, but rather a velocity profile. As one might expect, there are trade-offs associated with the size of an averaging interval (the number of samples which are fed into the covariance function).

By increasing the averaging interval, it is commonly the case that the covariance function assumes a more smooth and well-defined shape. However, increasing the averaging interval also means that the echoes from a wider range of scatterers are being correlated, and if the radial velocity of these scatterers is distributed rather than sharply defined (i.e. not all scatterers are of a common velocity) then the covariance peak may blur and result in a poor velocity estimate. In other words, a small averaging interval results in good range resolution but may rob the covariance function of additional important data, which then may lead to poor velocity resolution. In the case of a large averaging interval, the velocity resolution improves until the range bins include a (potentially) wide distribution of scatterer velocities, at which point velocity estimate accuracy would degrade. One major advantage to this VEM is that there is no ambiguous velocity, as there is with the phase-based methods. The concept of ambiguous velocity is discussed later in more detail.

### Ping Pair Covariance

The ping pair covariance method is similar to the incoherent method in that echoes from one ping are correlated with echoes from the next ping, but is different because the present method assumes coherence and uses phase - not magnitude - to determine target velocity. The trade-off in this case is summarized simply by stating that the use of phase for velocity estimation allows for greater accuracy and precision, but can come at the expense of a lowered velocity tolerance.

Let us restate Equation 2.83 so that we can see the mathematical structure of this velocity estimation method:

$$K_{\tilde{s}_1\tilde{s}_2}(kT_k) = E_t S_R e^{jw_D(kT_k - T_p)} \text{tri} \left( \frac{kT_k + \frac{2v}{c}T_p}{k_p T_s} \right).$$

We seek to determine the phase change between pings, which arises from the  $e^{-jw_D T_p}$  term. An easy way to isolate this exponential term is to measure the phase at the center of the covariance function, when  $k = 0$ . (It will soon become apparent why the center of the covariance function is still essentially located at  $k = 0$  when tolerable target velocities are taken into account.) This approach is simple in its implementation and is highly accurate at determining small-scale motions, but runs into problems very quickly due to phase wrapping.

Assuming that phase is measured at zero lag, we are considering the term  $e^{-jw_c \frac{2v}{c} T_p}$ . Let us numerically evaluate this term so that we have an idea what sort of velocities this

VEM can tolerate. In typical URL applications, the carrier frequency is around 300 kHz, or  $w_c = 2\pi f_c = 1.885 * 10^6$  radians per second. At this frequency, we assume that significant echoes return to the transducer from ranges up to approximately 150 m (a two-way travel distance of 300 m). If the speed of sound in water is 1500 m/s, the the first ping is completed after  $t = 300/1500 = .2$  s. Let us suppose, therefore, that  $T_p = .25$  s to account for any delays which arise from electronics issues. Our exponential now evaluates to  $e^{-j200\pi v}$ . The maximum target speed that we can therefore tolerate is  $v = \pm 1/200$  m/s, beyond which speed we observe phase wrapping in the exponential term. The shift in the center of the covariance function which is brought about by this non-ambiguous target velocity is therefore negligible, as it contributes a shift of  $\frac{2v}{c}T_p = \frac{2}{4*200*1500} = \frac{1}{6000}$  lags.

For the cases where no phase wrapping has occurred, velocity estimates are easy to obtain. Because the phase shift at the center of the covariance function results from the term  $e^{-jw_c \frac{2v}{c}T_p}$ , our velocity estimates are simply

$$\hat{v} = \frac{\hat{\gamma}c}{4\pi T_p f_s} \quad (2.90)$$

where  $\hat{\gamma}$  is the estimate of the phase shift at lag zero, and  $f_s$  is the sampling frequency, which in our case is equal to the carrier frequency  $f_c$ . Notice that the expression which we are using to calculate velocity estimates is obtained by simply labeling the argument of the exponential function (without the  $j$ ) as  $\hat{\gamma}$  and then solving for  $v$ .

This VEM is particularly accurate because it is resistant to both of the main sources of decorrelation: thermal noise, and footprint shift (physically, this is simply the translation of scatterers between pings) as were described in 2.3.3. We choose to constrain the system to be such that it causes no phase wrapping which would frustrate our simplistic processing technique, which means that we have constrained the system to *not* be capable of replacing many scatterers between pings, thus mitigating any decorrelation arising from the  $\tilde{N}$  terms. Mathematically, this means that our  $snr_c$  remains very high.

Let us illustrate this point via another simplistic calculation. A 150 cycle monopulse at a carrier frequency of 300 kHz (wavelength of approximately 5 mm) has a pulse length of 0.75 m in the water. At long distance, when the pulse has its smallest projection on the seafloor, echoes are received at any particular moment in time from a footprint which is 0.375 m long. If our time between pings is again 0.25 s, and our target (the seafloor) is moving at  $v = 1/200$  m/s, then it moves 0.00125 m between pings. If we assume that seafloor scatterers have a uniform density of 100 scatterers per meter, then the original footprint

had 37.5 scatterers inside it. The new footprint, which has been shifted by 0.00125 m from the previous footprint, will have introduced 1/8 of a new scatterer into the resulting echo. This is not a substantial contribution, and therefore we expect the  $\tilde{N}$  terms to have little effect on our effective SNR, which remains dominated by the thermal noise contribution.

### Single Ping Covariance

The single ping covariance approach, as the name would suggest, produces velocity estimates without requiring multiple pings. Immediately, we note that the increased data rate comes at a price: since we are no longer cross-correlating two separate pings, but are taking the autocovariance of a single ping, our thermal noise terms may now be correlated and may potentially degrade the performance of our estimator. Not only that, but we may run into additional decorrelation in the form of the  $\tilde{N}$  term because we are using one time sample to predict a later time sample inside the same ping - and we know that even if the target is not moving very quickly, sound still travels at the same speed in water - so we cannot expect one time sample to have many scatterers in common with later time samples.

Before we begin our discussion of this method, it must first be mentioned that the single ping covariance approach is really a special case of linear prediction. When using linear prediction to estimate a target's velocity, the user may choose how many degrees of freedom he or she wishes to allow in the estimation procedure. In essence, we are asking the question "How many targets do I expect to be present in each range bin?" If only a single target is present, then a single degree of freedom is sufficient to estimate this single velocity. If multiple targets (with multiple velocities) are present in each range bin, then multiple degrees of freedom can be allowed such that multiple velocity estimates are produced, and not a single estimate which represents an average of all target velocities within the range bin.

The single ping covariance approach is equivalent to using linear prediction with only a single degree of freedom. This fact becomes easier to see after the math behind the linear prediction method has been presented, but deserves noting before our analysis. We proceed through our mathematical discussion of this velocity estimation method as though the similarity between the covariance and linear prediction approaches is already accepted, and justify this claim using the math which is to follow.

### One Degree of Freedom

Let us examine how linear prediction looks in the context of our sonar system, beginning with a simple case and adding complexity on top of it. The URL sonar system which relates to this thesis is a 6-element receive array, and each transducer channel records a time series of observations. Our received time series therefore looks like this:

$$\begin{pmatrix} \tilde{s}_{1,1} & \tilde{s}_{1,2} & \dots & \tilde{s}_{1,n} \\ \tilde{s}_{2,1} & \tilde{s}_{2,2} & \dots & \tilde{s}_{2,n} \\ \tilde{s}_{3,1} & \tilde{s}_{3,2} & \dots & \tilde{s}_{3,n} \\ \tilde{s}_{4,1} & \tilde{s}_{4,2} & \dots & \tilde{s}_{4,n} \\ \tilde{s}_{5,1} & \tilde{s}_{5,2} & \dots & \tilde{s}_{5,n} \\ \tilde{s}_{6,1} & \tilde{s}_{6,2} & \dots & \tilde{s}_{6,n} \end{pmatrix}. \quad (2.91)$$

Here, we are using  $\tilde{s}_{4,2}$  to signify the second time sample which was received by the fourth transducer element. We seek to use earlier time samples to predict later time samples, and in doing so determine the phase change which has occurred in this interval. To accomplish our goals, prediction must be performed across individual transducer channels - thereby avoiding phase changes which may result when switching from element to element.

In the most simple case, we would take a single time sample from a single transducer channel and use it to predict a later time sample from that same channel:

$$\tilde{s}_{1,3} = \tilde{s}_{1,2}\hat{w}. \quad (2.92)$$

By finding  $\hat{w}$  we have found the value that transforms  $\tilde{s}_{1,2}$  into  $\tilde{s}_{1,3}$ , and it represents our estimate of any amplitude and phase changes which occurred to the signal from time  $t = 2$  to time  $t = 3$ . Our problem is to solve the general equation  $d = xw$ . If we define signals  $\tilde{s}_{1,2}$  and  $\tilde{s}_{1,3}$  as

$$\tilde{s}_{1,2} = a_2 e^{j\theta_2} \quad (2.93)$$

$$\tilde{s}_{1,3} = a_3 e^{j\theta_3} \quad (2.94)$$

then our solution  $\hat{w}$  looks like this:

$$\hat{w} = \frac{a_3 e^{j\theta_3}}{a_2 e^{j\theta_2}} \quad (2.95)$$

where  $\theta$  represents the phase angle at our respective samples and  $a$  represents their respective amplitudes.

A more complicated example employs some pre-estimation averaging to improve the quality of our estimate of the phase change between samples. Again, we seek only to solve the equation  $\vec{d} = \vec{x}w$ , except now we are dealing with vectors of observations  $\vec{d}$  and  $\vec{x}$ . Let us now take multiple time samples from multiple transducer elements and use them to predict the subsequent time samples via the weight estimate  $\hat{w}$ :

$$\vec{d} = \vec{x}\hat{w} \quad (2.96)$$

$$\begin{pmatrix} \tilde{s}_{1,3} \\ \vdots \\ \tilde{s}_{6,3} \end{pmatrix} = \begin{pmatrix} \tilde{s}_{1,2} \\ \vdots \\ \tilde{s}_{6,2} \end{pmatrix} \hat{w}. \quad (2.97)$$

The solution for  $\hat{w}$  is then

$$(\vec{x}^H \vec{x}) \hat{w} = \vec{x}^H \vec{d} \quad (2.98)$$

$$\hat{w} = (\vec{x}^H \vec{x})^{-1} \vec{x}^H \vec{d} \quad (2.99)$$

where  $H$  signifies the Hermitian transpose (complex conjugate *and* transpose). Equation 2.99 takes the form of a discrete correlation over  $m$  samples when written out explicitly:

$$\hat{w} = \frac{\sum_{i=1}^m \tilde{s}_{i,2}^* \tilde{s}_{i,3}}{\sum_{i=1}^m \tilde{s}_{i,2}^* \tilde{s}_{i,2}} \quad (2.100)$$

$$= \hat{\rho} e^{j\hat{\theta}_w} \quad (2.101)$$

where we are using the  $m$  samples to estimate the theoretical correlation  $E\{\tilde{s}_{i,2}^* \tilde{s}_{i,3}\}$ . In our simple case, we have only six transducer elements so  $m = 6$ . Note that the theoretical correlation function is independent of  $i$ ; it assumes the same form regardless.

If we wanted to incorporate additional snapshots from other time samples, we would augment vectors  $\vec{x}$  and  $\vec{d}$ . Suppose that we wished to augment the vectors in Equation 2.97 with another set of time samples at times  $j$  and  $j + 1$  from each transducer channel: we would simply write

$$\begin{pmatrix} \tilde{s}_{1,i+1} \\ \vdots \\ \tilde{s}_{6,i+1} \\ \tilde{s}_{1,j+1} \\ \vdots \\ \tilde{s}_{6,j+1} \end{pmatrix} = \begin{pmatrix} \tilde{s}_{1,i} \\ \vdots \\ \tilde{s}_{6,i} \\ \tilde{s}_{1,j} \\ \vdots \\ \tilde{s}_{6,j} \end{pmatrix} \hat{w} \quad (2.102)$$

and then solve for  $\hat{w}$  as outlined in Equations 2.99 and 2.100 by forming estimates of the covariance function.

Since estimates are formed from within a single ping, the linear prediction VEM is seen to rely upon the autocovariance function. Equation 2.82 describes this autocovariance, and it is restated presently for the reader's convenience:

$$K_{\tilde{s}_1\tilde{s}_1}(kT_k) = E_t S_R e^{jw_D k T_k t r i} \left( \frac{k T_k}{k_p T_s} \right) + 2\sigma_n^2 \cdot \text{sinc}(2kT_k \cdot BW).$$

One subtle difference in notation must be stated: until now the third time sample from the  $i$ th transducer element was referred to as  $\tilde{s}_{i,3}$  and it was assumed that these samples came from within the same ping. However, when referring to the covariance function, it is necessary to return to our "old" notation of using subscripts to signify ping number, rather than sample number or transducer number.

We conclude that when using monopulse linear prediction, the estimator is estimating the theoretical autocovariance given by Equation 2.82. Once the weight  $\hat{w}$  has been found, we have essentially "predicted" the phase at time sample  $\tilde{s}_3$  from time sample  $\tilde{s}_2$ , with the angle of our weight  $\hat{w}$  representing our estimate of the phase change between samples,  $\angle \hat{w} = \hat{\gamma}$ . From our autocovariance function, we can see that any phase results from the exponential term. By evaluating the argument of the exponential and solving for  $v$  we arrive at the equation which transforms phase change estimates into velocity estimates::

$$\hat{v} = \frac{\hat{\gamma}c}{4\pi f_s k T_k} = \frac{\hat{\gamma}c}{4\pi k}$$

since (in our case)  $T_k = 1/f_s$ .

Examining the behavior of this estimator in terms of the signal model which was developed in Section 2.3.3, we see that as  $k$  moves away from zero the amplitude of the autocovariance function decreases. Physically, this results from a replacement of scatterers between time samples, causing decorrelation. However, at these greater  $k$  values (when  $k > 3$ ) the influence of thermal noise in the correlation functions goes towards zero (this transition depends upon the width of the filter  $p$ ). Likewise, when  $k$  is close to zero, decorrelation caused by footprint shift (the  $\tilde{N}$  term) grows less important while decorrelation caused by thermal noise (the  $\tilde{n}$  term) grows more dominant. When using the linear prediction algorithm, one must endeavor to find the optimal lag  $k$  where the influences of both noise terms  $\tilde{N}$  and  $\tilde{n}$  are minimized such that the CRLB is minimized.

Note that this method, as with the ping pair covariance method, also suffers from a maximum unambiguous velocity requirement. However, since subsequent observations of the target are made in much more rapid succession with the single ping covariance method (as opposed to the ping pair covariance method) this maximum unambiguous velocity is much higher. In the present case, instead of working with the exponential term  $e^{jw_D T_p}$  in the cross covariance function, we are working with the exponential term  $e^{jw_D k T_k}$  in the autocovariance function. If we choose our estimation to be performed at a lag of  $k = 65$  time samples, then the subsequent maximum unambiguous velocity would be approximately 5.77 m/s, or just over 11 knots.

### Multiple Degrees of Freedom

This VEM has a unique property which is now discussed in greater detail. We have seen how to obtain a single velocity estimate by estimating the autocovariance function, but it is possible to use this VEM to simultaneously estimate multiple velocities. Mathematically, this translates into allowing multiple degrees of freedom when solving for the weight  $\hat{w}$  [4].

Suppose that we wish to allow two degrees of freedom, and that we wish to average all six transducer channels together (pre-estimating averaging, that is). We must now include additional time samples in the matrix  $\mathbf{x}$  which is used to predict  $\vec{d}$ , such that:

$$\begin{pmatrix} \tilde{s}_{1,3} \\ \vdots \\ \tilde{s}_{6,3} \end{pmatrix} = \begin{pmatrix} \tilde{s}_{1,1} & \tilde{s}_{1,2} \\ \vdots & \vdots \\ \tilde{s}_{6,1} & \tilde{s}_{6,2} \end{pmatrix} \hat{w}. \quad (2.103)$$

Note that  $\hat{w}$  is now a vector,  $\hat{w} = \begin{pmatrix} \hat{w}_1 \\ \hat{w}_2 \end{pmatrix}$ . Our solution for  $\hat{w}$  is not as simple now as it was in the case of only one degree of freedom. We seek to employ the solution to the classic least-squares problem, and the interested reader may learn about this in greater detail by referring to [20]. The vector  $\hat{w}$  is obtained by solving

$$\hat{w} = (\mathbf{x}^* \mathbf{x})^{-1} \cdot \mathbf{x}^* \vec{d}. \quad (2.104)$$

$\hat{w}$  is converted into  $\hat{\gamma}$  by first forming an augmented weight vector,  $\vec{w}_a$ :

$$\vec{w}_a = \begin{pmatrix} 1 \\ -w_2 \\ -w_1 \end{pmatrix} \quad (2.105)$$

where we have reversed the order and negated the signs of our original  $\hat{w}$  vector. Next, we use  $\vec{w}_a$  to define the coefficients of a complex polynomial, and calculate the roots. The angle(s) of the roots represent  $\hat{\gamma}$ , which is the solution to the  $n$ th order polynomial defined by  $w_a$ . If four degrees of freedom are allowed, we would have a fifth-order polynomial and four roots, which represent four estimates of the phase change(s) between samples. Note that this is no longer two-point velocity estimation, however.

### Covariance Estimation as a Special Case of Linear Prediction

We now conclude that single ping covariance estimation is a special case of linear prediction. The solution, 2.104, is the general form - while 2.99 is a special case of the solution to the least squares problem. When solving the classic least squares problem and using vectors - rather than matrices - as input variable  $x$ , it is the theoretical autocovariance function which both estimators are trying to estimate.

Physically, the usage of matrices rather than vectors translates into allowing more degrees of freedom when characterizing the system. This implies that although these two methods are highly related, the linear prediction VEM is a more general procedure than the covariance approach. By allowing additional (more than 1) degrees of freedom with which to characterize the system, we are making allowances for multiple targets which are moving at separate velocities to exist within a common range cell. Such scenarios are easy to envision, such as when two fish which are in close proximity but are traveling in different directions. Throughout this thesis, the term "single ping covariance" is used in place of "linear prediction" because it is more specific (it specifies a single degree of freedom) and because the term "covariance" is used widely in the literature.

#### 2.4.2 Pulse Pair Methods

When transmitting a pulse pair rather than a monopulse (recall Figure 2.1), each estimator behaves differently due to the different nature of the wave which is "collecting" information about the marine environment. Now that two distinct pulses are transmitted inside each ping, it is possible to "observe" some targets twice per ping. Returns at a given time are simultaneously composed of echoes from the first pulse and from the second pulse - meaning that we create "self noise" in the system. In other words, returns which arrive from the first pulse are indistinguishable from returns which arrive from the second pulse. A number of

differences between monopulse VEMs and pulse pair VEMs therefore need to be discussed.

### **Methods We Won't Consider**

It is possible to carry out ping pair covariance processing while transmitting a pulse pair by simply processing these echo returns exactly as was discussed in Section 2.4.1. One need only consider the differences in the waveforms to decide that the monopulse waveform is superior for this sort of processing. Imagine two waveforms which have a total length of 150 cycles of the carrier frequency. The first waveform is a monopulse, where the envelope shares the length of the pulse (150 cycles). The second waveform is a pulse pair, where the two smaller envelopes compose the ping (and where total pulse length is 150 cycles from the head of the first pulse to the tail of the second pulse). If each of these smaller envelopes is 75 cycles in length, then there could be no dead time between them and they would combine for a total envelope size of 150 cycles, and we'd be left with a monopulse. However, a pulse pair has been defined as a waveform where there is a non-zero amount of dead time between these two envelopes. If there are 300 scatterers inside the 150-cycle monopulse at a given time, then there cannot - by definition - be as many scatterers inside a pulse pair of the same size (150 cycles from the head of the first pulse to the tail of the second pulse). For this reason, further consideration of ping pair processing (either coherent or incoherent) with a pulse pair waveform is not given in the present document.

Another form of incoherent processing may be attempted with pulse pair waveforms, but meets with absolutely no success. It is a simple endeavor to show that echoes from a single ping of a pulse pair waveform cannot be processed incoherently to form velocity estimates. Consider once more a single slowly fluctuating point target at an arbitrary range. We expect the autocovariance of the received time series to be a three-peaked structure. The main peak is of magnitude 1 and is centered at a lag of zero, while the side peaks have an amplitude of 0.5 and are located at lags corresponding to the the peak-to-peak separation of the two transmitted pulses (a lag of 65 cycles, in this case). This structure is independent of target velocity, and therefore cannot be used to form velocity estimates.

### **Pulse Pair Covariance**

The pulse pair covariance method is, like the other methods, easy to describe in simple mathematical terms. Proceeding with the simplistic description, this VEM relies upon an

autocovariance of intervals of the received time series to generate its velocity estimates. The autocovariance of such a time series (assuming low noise) is a three-peaked structure, as described by 2.84 which is restated here:

$$\begin{aligned}
K_{\tilde{s}_1\tilde{s}_1}(kT_k) &= E_t S_R e^{jw_D kT_k} \\
&\cdot \left[ \frac{1}{2} \text{tri} \left( \frac{kT_k + k_s T_s + k_p T_s}{k_p T_s} \right) + \text{tri} \left( \frac{kT_k}{k_p T_s} \right) \right. \\
&\quad \left. + \frac{1}{2} \text{tri} \left( \frac{kT_k - k_s T_s - k_p T_s}{k_p T_s} \right) \right] + 2\sigma_n^2 \cdot \text{sinc}(2kT_k \cdot BW) \quad (2.106)
\end{aligned}$$

While the central peak represents a correlation of both the leading and trailing pulses with themselves, respectively, the side peaks do not. At the side peaks, we are instead observing a correlation between the signal returned when the leading pulse interacted with scatterers that were later interacted with by the trailing pulse. In other words, we are correlating the returns of the first pulse with the returns of the second pulse at some other time.

It is the phase of the autocovariance at these side peaks which is of interest. Since these side peaks represent, mathematically, the process of searching for similarity between the first and second times a given set of scatterers were hit, any non-zero phase at the side peak corresponds to physical motion. If there is no motion between measurements, then there is no pathlength difference between the first and second observations - and thus, no phase difference (in an ideal world). Mathematically, this is seen by setting  $v = 0$  and evaluating the exponential term at a lag corresponding to either side peak (note that lag is irrelevant to this exponential term if  $v = 0$ ).

When working with pulse pair waveforms, instead of correlating Pings 1 and 2 to get our velocity estimate we find the autocovariance of Ping 1 alone. Finally, we invoke

$$\hat{v} = \frac{\hat{\gamma}c}{4\pi f_s kT_k}$$

to arrive at our velocity estimate. This equation has a familiar form, and we set  $k = 65$  which corresponds to the number of cycles of the carrier separating the head of the first pulse from the head of the second pulse in our test waveform. With monopulse linear prediction,  $k$  is not constrained to be equal to any particular value, and can be adjusted at the whim of the signal processor. Although we are now working with an autocorrelation instead of a cross-correlation between pings, we still do not have to worry about the contribution of thermal noise (to the theoretical covariance function) if we make the bandpass filter sufficiently wide.

## 2.5 Performance Limitations

The Cramer-Rao lower bound (CRLB) represents the lowest variance which unbiased estimators can attain. Excellent discussions of the CRLB are found in [3, 18, 23, 26], and the interested reader is referred there for questions relating to its application to MASB sonar systems or its derivation. The present document uses a method similar to that used in [3] for calculation of the CRLB in the context of angle of arrival estimation, but instead calculates the CRLB for velocity estimates.

We seek now to bound the performance of the estimators which are to be tested, using the CRLB to predict their lowest achievable error (measured in root mean-squared error, or RMSE, the bound of which is  $\sqrt{CRLB}$ ). Coherent methods, which use all of the information available (including phase) represent a potentially more precise means by which to produce velocity estimates. Since we seek to find optimal performance expectations and to compare these with simulated and real data, the bounds on coherent VEMs prove to be sufficient for our purposes, without necessitating investigation into the performance bound of the incoherent method.

After deriving a general expression for the applicable CRLB, we explore the behavior of the bound as we change certain parameters. In particular, we probe the behavior of the bound (when transmitting a monopulse) as we vary the lag  $k$  at which estimation is performed, and we determine whether it is more beneficial to increase the number of independent snapshots or to increase pulse length when seeking to lower the CRLB. We also compare the CRLB for a monopulse to the CRLB for a pulse pair (when single ping covariance processing is used with each waveform) in the case where  $snr_c$  is the same for both estimators, and then we examine the pulse pair CRLB and its potential for improvement when "matched" filtering is performed. Finally, we determine (for each of the coherent VEMs) the simulated ratio of the velocity estimate RMSE to the square-root of the CRLB (for velocity estimates).

### 2.5.1 Expressions for the Cramer-Rao Lower Bound

Because we have assumed a Gaussian model for both our signal and our noise, the time samples in our received time series are also Gaussian in nature. One of the parameters in these samples is the phase angle, and it is related to the parameter which we wish to estimate: target velocity. For Gaussian random variables, the CRLB can be obtained from

the covariance matrix - and because one of the parameters of these random variables (phase angle) is related to target velocity, we may therefore express the CRLB in terms of target velocity. Much of the groundwork for this derivation was developed by Van Trees [26], but Bird and Mullins [3] also provide a general framework and a number of convenient approximations which allow for the following derivation to be expedited. The present thesis draws heavily from both sources in this theoretical development.

Assuming a zero-mean complex Gaussian model for both signal and noise, we express the CRLB in terms of the covariance function (which, in our case, is equivalent to the correlation function):

$$\mathbf{J}_{ik} = N \cdot \text{trace} \left\{ \mathbf{K}^{-1} \frac{\partial \mathbf{K}}{\partial u_i} \mathbf{K}^{-1} \frac{\partial \mathbf{K}}{\partial u_k} \right\} \quad (2.107)$$

where  $\mathbf{J}_{ik}$  is the Fisher information matrix,  $\mathbf{K}$  is the covariance matrix,  $\mu$  is a parameter to be estimated, and  $N$  is the number of independent snapshots. For this analysis, we are using the covariance function described in Equation 2.86.

If we assume that the phase angle is the only unknown parameter, then the Fisher information matrix becomes a scalar, related to the CRLB thusly:

$$CRLB(\gamma) = \frac{1}{J} \quad (2.108)$$

and the Fisher information is calculated from:

$$J = N \text{trace} \left\{ \mathbf{K}^{-1} \frac{\partial \mathbf{K}}{\partial \gamma} \mathbf{K}^{-1} \frac{\partial \mathbf{K}}{\partial \gamma} \right\}. \quad (2.109)$$

Next, it is important to define the correlation (or in our case, the covariance) matrix. Since we are interested in using two time samples to estimate target velocity, we begin by invoking Equation 2.86 and see that the covariance matrix  $\mathbf{K}$  is a  $2 \times 2$  matrix for our two-point estimation:

$$\mathbf{K} = \begin{pmatrix} E[s_i s_i^*] & E[s_i s_{i+j}^*] \\ E[s_{i+j} s_i^*] & E[s_{i+j} s_{i+j}^*] \end{pmatrix} \quad (2.110)$$

$$= \begin{pmatrix} 2\sigma_s^2 + 2\sigma_n^2 & 2\sigma_s^2 \rho_{c,a}(kT_k) e^{jw_D kT_k} \\ 2\sigma_s^2 \rho_{c,a}(kT_k) e^{-jw_D kT_k} & 2\sigma_s^2 + 2\sigma_n^2 \end{pmatrix} \quad (2.111)$$

if we assume that sample  $s_{i+j}$  is sufficiently far removed from sample  $s_i$  that the thermal noise terms are uncorrelated. For our purposes, this assumption is valid for all coherent

VEMs which we are considering, assuming that the filter is sufficiently wide in the frequency domain to allow the signal through essentially unaffected.

By setting  $\gamma = w_d k T_k$  and then substituting Equation 2.111 into Equation 2.109, one obtains the solution

$$J = N \frac{2\rho_n^2(kT_k)\rho_c^2(kT_k)}{1 - \rho_n^2(kT_k)\rho_c^2(kT_k)} = \frac{1}{CRLB_N(\gamma)}. \quad (2.112)$$

By applying Equations 2.79 and 2.80, we arrive at the general expression for the N-snapshot Cramer-Rao lower bound for phase angle estimates for a single-ping VEM:

$$CRLB_N(\gamma) = \frac{1}{N} \left[ \frac{1}{snr_e} + \frac{1}{2snr_e^2} \right]. \quad (2.113)$$

Since our true interest lies in the Cramer-Rao bound on velocity estimates, we need to translate this result into  $CRLB_N(v)$ , giving us a performance bound on velocity estimates. Van Trees [26] derived a general means by which to translate the  $CRLB(\theta)$  into the  $CRLB(\phi)$ , where  $\theta = f(\phi)$ . Having calculated one scalar CRLB, translation to another scalar CRLB is performed through the relation:

$$CRLB(\phi) = G^{-T} CRLB(\theta) G^{-1} \quad (2.114)$$

where

$$G = \frac{d\theta}{d\phi}. \quad (2.115)$$

If single ping covariance processing is used to generate velocity estimates, whether the transmit waveform was a monopulse or pulse pair, the functional relationship that we seek has already been described:

$$v = \frac{c}{4\pi f_c k T_k} \Delta\phi = C\Delta\phi = C\gamma \quad (2.116)$$

which means that the phase angle  $\gamma = \Delta\phi$  is a function of the velocity as such:

$$\gamma = \frac{v}{C}. \quad (2.117)$$

We can translate this from the CRLB of an phase angle to the CRLB of the corresponding target velocity via:

$$CRLB(v) = C \cdot CRLB(\gamma) \cdot C = C^2 \cdot CRLB(\gamma). \quad (2.118)$$

Since we want to determine the RMSE bound for our estimators, we take the square root of this quantity to obtain the relation

$$\sqrt{CRLB_N(v)} = \frac{c}{4\pi f_c k T_k} \sqrt{CRLB_N(\gamma)} \quad (2.119)$$

$$= \frac{c}{4\pi f_c k T_k} \sqrt{\frac{1}{N} \left( \frac{1}{snr_e} + \frac{1}{2snr_e^2} \right)} \quad (2.120)$$

which applies to the single ping covariance VEMs (both the monopulse, and pulse pair). If we are using a monopulse ping pair in conjunction with covariance estimation, then the different functional relationship yields

$$\sqrt{CRLB_N(v)} = \frac{\lambda}{4\pi T_p} \sqrt{\frac{1}{N} \left( \frac{1}{snr_e} + \frac{1}{2snr_e^2} \right)}. \quad (2.121)$$

### 2.5.2 Minimizing the Cramer-Rao Lower Bound

In an effort to achieve the theoretically "best" two-point velocity estimates possible (i.e. those with the lowest RMSE) a further investigation into the CRLB is now conducted. Parameters such as thermal signal-to-noise ratio do influence the CRLB, but such parameters cannot always be controlled by the system operator. Other parameters, such as the number of snapshots  $N$  which are used in processing or the number of carrier cycles in the transmitted pulse  $k_p$  are much more readily user-controlled, and may also influence the CRLB. We seek to explore these user-controlled relationships.

This investigation also serves as a gentle transition into the Simulation Chapter of this thesis, where an ensemble of bottom scatterers is created and then employed to test the various VEMs. However at this intermediate stage, we seek to use simulation of a more simplistic sort to probe the CRLB: the present investigation focuses on exploring the CRLB in the context of generic time samples and not in the context of a simulated seafloor.

#### Finding the Optimal Lag

One parameter that affects the CRLB is the lag  $k$  at which estimation is performed. This parameter is easily user-controlled, and can be varied after data collection and during processing. Note that for the ping-to-ping processing discussed in this thesis (monopulse ping

pair covariance processing or incoherent processing) the user does not vary  $k$ , so this discussion applies to the (monopulse) single ping covariance processing method.

If one is simply estimating phase angles (and not target velocity) then  $CRLB_N(\gamma)$  applies, as described in Equation 2.113. Figure 2.9 shows the relationship between the lag  $k$  used in estimation and the  $\sqrt{CRLB_5(\gamma)}$ , where five snapshots have been chosen (this selection is arbitrary, and is inconsequential to the present discussion). It is clear to see that for any  $SNR_n$  it is desirable to minimize  $k$  in order to achieve the tightest bound on phase angle estimates. However, such is not the case when the user desires velocity estimates rather than phase angle estimates.

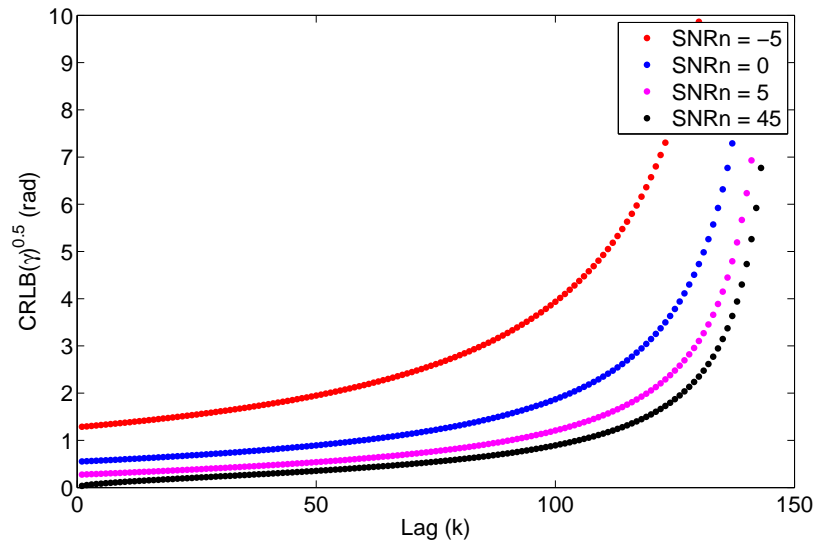


Figure 2.9: Plot of the square root of the Cramer-Rao lower bound for phase angle estimates as a function of the lag  $k$  which is used in estimation. Signal-to-thermal noise ratio  $SNR_n$  is varied from 45 dB (bottom curve) to -5 dB (top curve), and  $N = 5$  snapshots are used. A 150-cycle monopulse has been assumed, which causes  $\sqrt{CRLB(\gamma)}$  to tend towards infinity when  $k = 150$ .

Figure 2.10 displays the value of  $\sqrt{CRLB_5(v)}$  as a function of  $k$ . Recalling the relation given in Equation 2.120, we see that when  $k$  tends towards zero that the Cramer-Rao bound tends towards infinity, meaning that the minimum RMSE for velocity estimates becomes infinite. Likewise, when  $k$  tends towards  $k_p$  (the length of the transmitted pulse) then the bound also tends towards infinity because we have effectively minimized  $SNR_c$  and are

attempting to produce velocity estimates via a correlation of uncorrelated time samples.

The obvious next step is to determine the value  $k_0$  which minimizes  $\sqrt{CRLB(v)}$ . In practical situations, we expect  $SNR_c \ll SNR_n$  because of the many unavoidable sources of decorrelation (such as boat motion between (or during) pings, or the use of a non-zero lag  $k$  in estimation). Under this condition, we say that  $SNR_e \approx SNR_c$ , and by taking the partial derivative of  $CRLB(v)$  the setting the answer equal to zero and solving the quadratic equation, one obtains the solution

$$k_0 = k_p \left( \frac{3 - \sqrt{5}}{2} \right) \quad (2.122)$$

$$\approx 0.382k_p. \quad (2.123)$$

For a 150-cycle monopulse with one sample per cycle,  $k_0 \approx 57$ . This assumes that the received signal is sampled once per cycle - if such is not the case, then  $k_0$  would be scaled accordingly:  $k_0 \approx 0.382k_p \frac{f_s}{f_c}$ .

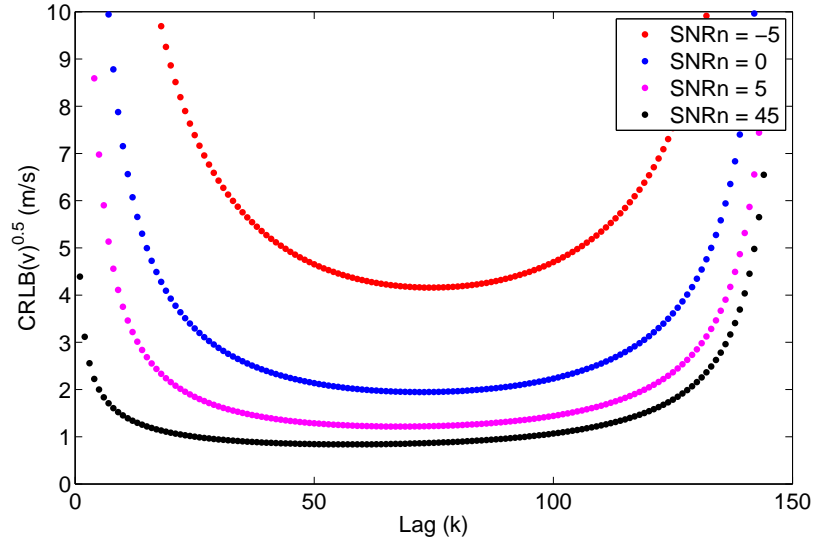


Figure 2.10: Plot of the square root of the Cramer-Rao lower bound for velocity estimates as a function of the lag  $k$  which is used in estimation. Signal-to-thermal noise ratio  $SNR_n$  is varied from 45 dB (bottom curve) to -5 dB (top curve), and five snapshots are used. A 150-cycle monopulse has been assumed.

### More Snapshots, or a Longer Pulse?

Assuming that the sonar system conducts a measurement of finite duration, one may ask whether it is better to perform a single long observation, or whether it is desirable to perform a series of shorter - and independent - observations. In [3] it was shown that when estimating the phase difference between time samples from two different transducer channels, the standard deviation of the estimator (for high  $SNR_e$ ) approaches the  $\sqrt{CRLB_N(\gamma)}$  quickly as more independent snapshots are used in estimation. In fact, Bird and Mullins concluded that most of the improvement in the estimator performance occurs in the first 5 additional (independent) snapshots. This result also applies to estimating the phase change between time samples of the same transducer, but in this case there are additional considerations which need to be taken into account.

First, one must recall that the N-snapshot CRLB depends upon the number of  $N$  *independent* snapshots. For example, if a pulse of length  $k_p$  is transmitted, and time samples 1 and 20 are used in estimation for the first snapshot, then the next *independent* snapshot must be obtained after time sample  $20 + k_p$ .

Let us assume that for whatever the length of the pulse, estimation is always performed when using the optimal lag  $k_0$ . Figure 2.11 shows that when estimation is performed at  $k_0$ , it is superior to have a longer pulse than to have a shorter pulse with more independent snapshots. If we consider the point on the x-axis corresponding to 1500 time samples, we see that if we divide that quantity of information into 25 independent snapshots that the  $\sqrt{CRLB(v)}$  is at a much higher value than if we had transmitted a 1500-cycle long pulse (bottom curve). This implies that maximizing  $k_p$  has a greater impact than maximizing  $N$ , and that if one must choose between increasing either one or the other, increasing  $k_p$  is more effective at minimizing the CRLB. If we refer to Equation 2.120, we can easily see that such is the case because  $\sqrt{CRLB_N(v)} \propto 1/\sqrt{N}$ , but we can see that there exists a much stronger relationship to lag:  $\sqrt{CRLB_N(v)} \propto 1/k$ . We note from Figure 2.11 that the differences brought about by pulse length and the number  $N$  independent snapshots are most pronounced when fewer data are used in estimation, and that as more of the time series is used for estimation it becomes less important whether or not the data were taken by a long monopulse or a large number of independent snapshots.

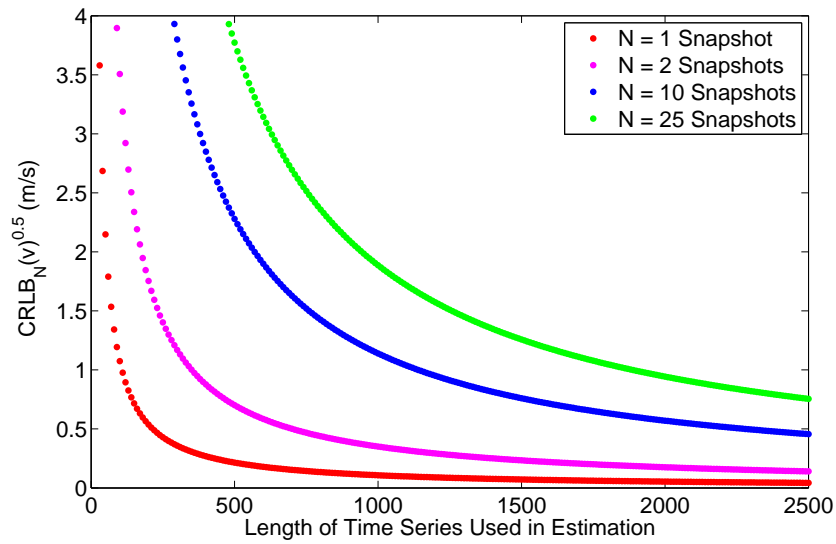


Figure 2.11: Plot of the square-root of the Cramer-Rao lower bound for velocity estimates as a function of the length of the time series (the number of samples) which is used for processing. The red curve represents the CRLB which is attained if the time series is used as a single long observation (in our case, a long pulse), and all subsequent curves represent the CRLB which is attained if the time series is divided into a smaller number of independent snapshots.

### 2.5.3 Calculating the CRLB for the VEMs

We now seek to determine the theoretical performance limitations of our estimators. By choosing to express these performance limitations in terms of RMSE instead of a quantity such as the variance, our answer is expressed in units of meters per second - a more physically meaningful quantity than an answer expressed in  $m^2/s^2$ . Anytime a numerical calculation is performed, we are referring to the envelope correlation functions which have been specified in Equations 2.82 through 2.85.

#### Ping Pair Covariance

In the case of the ping pair covariance method, a cross-covariance across two pings is used to produce velocity estimates. Because we are not considering any ping pair covariance processing performed with a pulse pair waveform, this method is considered for the monopulse only. We seek to obtain a numerical solution which bounds the performance of this estimator, given an assumption about  $SNR_c$ . Specifically, we assume that covariance processing is performed when target velocities are below our previously-specified maximum velocity of 1/200 m/s. The reader will recall that we have previously assumed all echoes from any given ping will have been received within the (assumed) time between pings:  $T_p = .25$  seconds. With estimation performed at  $k = 0$  lag and with a test monopulse of 130 cycles, the coherent correlation coefficient  $\rho_c(0)$  is greater than or equal to  $\rho_c \geq 1 - \frac{kT_k + 2vT_p/c}{k_p T_s} = 0.996$ , which implies that the "correlated" signal to noise ratio  $snr_c$  is equal to or greater than  $snr_c \geq 249$  and that  $SNR_c \geq 24$  dB.

From this result, we may now calculate the N-snapshot CRLB for velocity estimation in the context of ping pair covariance estimation after determining the value of  $N$ . We assume that  $N = 10$  snapshots are used to form a given velocity estimate. By choosing to use so many snapshots we have decreased our range resolution, but we have improved our velocity resolution.

The 10-snapshot  $\sqrt{CRLB}$  for monopulse covariance velocity estimates can then be calculated as:

$$\sqrt{CRLB_{10}(v)} = \frac{\lambda}{4\pi T_p} \sqrt{\frac{1}{10} \left[ \frac{1}{243} + \frac{1}{2 \cdot 243^2} \right]} \quad (2.124)$$

$$\approx 3.23 \cdot 10^{-5} m/s \quad (2.125)$$

when  $SNR_n = 40$  dB. This value represents the minimum root mean-squared error which we can expect to obtain when using this method to produce velocity estimates - and it is quite low indeed, even though we are constrained to estimate velocities which are lower than  $1/200 = 5 \cdot 10^{-3}$  m/s.

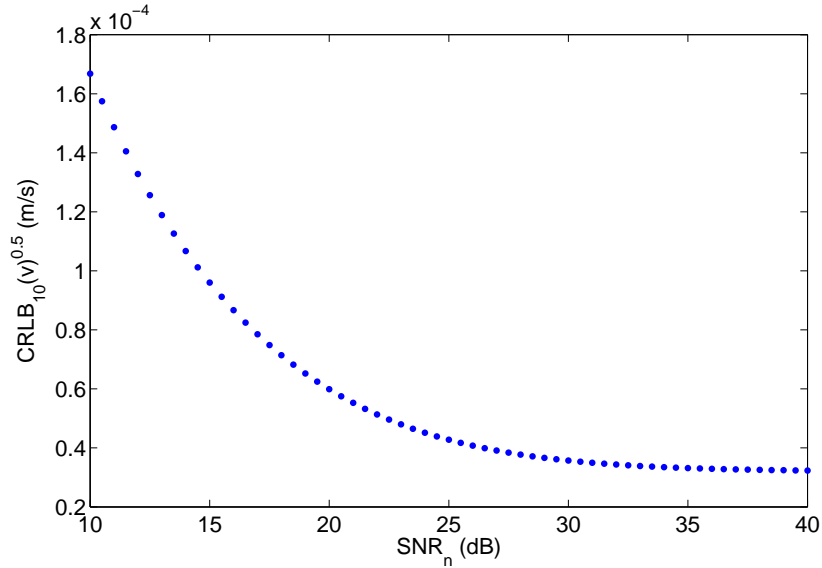


Figure 2.12: Plot of the square root of the 10-snapshot Cramer-Rao lower bound for ping pair covariance velocity estimates as a function of the  $SNR_n$  when  $T_p = .25$  s. Signal-to-thermal noise ratio  $SNR_n$  is varied from 10 dB to 40 dB. A 130-cycle monopulse has been assumed, and  $SNR_c = 24$  dB corresponding to the lowest value which we expect it to equal for this VEM (as limited by the maximum unambiguous target velocity) at this  $T_p$ .

Figure 2.12 shows a plot of  $\sqrt{CRLB_{10}(v)}$  versus the signal-to-thermal noise ratio  $SNR_n$  for the ping pair covariance method. From this plot we can see that as  $SNR_n$  increases,  $\sqrt{CRLB_{10}(v)}$  decreases noticeably. Due to the low values of  $\sqrt{CRLB_{10}(v)}$  throughout the range of  $SNR_n$ , we can also conclude that although thermal noise levels have a definite impact on this VEM, this VEM achieves such a low  $\sqrt{CRLB_{10}(v)}$  because  $SNR_c$  remains high.

### Single Ping Covariance

Let us now compare the Cramer-Rao lower bound for the single ping covariance VEMs, for both the monopulse and pulse pair. It is assumed that the linear prediction algorithm is working in the simplistic case and only allowing a single degree of freedom. This assumption is consistent with the processing techniques reported in subsequent Chapters which have been employed on both simulated and real data. Let us assume that the monopulse is  $k_p = 130$  cycles of the carrier in length and the delay between samples used in linear prediction is  $k = 65$  cycles of the carrier. By setting  $k$  thusly,  $snr_c = 1$  is the same between both the monopulse and the pulse pair single ping VEMs. The optimal lag for the monopulse would have been  $k_0 \approx 50$  for a pulse of length  $k_p = 130$ , so we expect sub-optimal performance from this estimator. This sub-optimal performance is almost negligible, however, as the  $\sqrt{CRLB_{10}(v)}$  will increase to  $\approx 0.71$  m/s from an optimal value of  $\approx 0.68$  m/s. Referring back to Figure 2.10, we can see that as long as  $k \approx k_0$ , the resulting  $CRLB(v)$  remains essentially unchanged from its lowest value.

Throughout this and subsequent CRLB calculations,  $snr_n$  holds the same value:  $snr_n = 10000$  or  $SNR_n = 40$  dB. This implies that  $snr_e \approx 1$  ( $SNR_e \approx 0$  dB) for both the monopulse and pulse pair VEMs. Since it is not  $SNR_n$ , but rather  $SNR_c$  which limits the CRLB for this estimator, it makes an almost negligible difference if  $SNR_n$  increases beyond approximately 40 dB. We note that the CRLB is the same for both of the single ping covariance estimators, and is calculated as:

$$\sqrt{CRLB_{10}(v)} = \frac{1500}{4\pi 65} \sqrt{\frac{1}{10} \left[ \frac{1}{1} + \frac{1}{2(1)^2} \right]} \approx 0.71 m/s. \quad (2.126)$$

Figure 2.13 shows the behavior of the  $\sqrt{CRLB_{10}(v)}$  for single ping covariance velocity estimates for either the  $k_p = 30$  and  $k_s = 35$  pulse pair, or for the  $k_p = 130$  monopulse. Unlike the ping pair covariance method, even with the addition of more snapshots the  $\sqrt{CRLB_{10}(v)}$  for this estimator is still orders of magnitude higher than the bound for the ping pair covariance monopulse estimator. This discrepancy is explained by the difference in  $SNR_c$  between these two estimators; in the case of the ping pair,  $SNR_c = 24$  dB while in the present case,  $SNR_c \approx 0$  dB.

Averaging across multiple transducer channels can decrease the CRLB, but also comes with certain inherent risks. With this (and other coherent estimators) if a single channel is used to form velocity estimates and phase wrapping occurs, it is easy for the operator

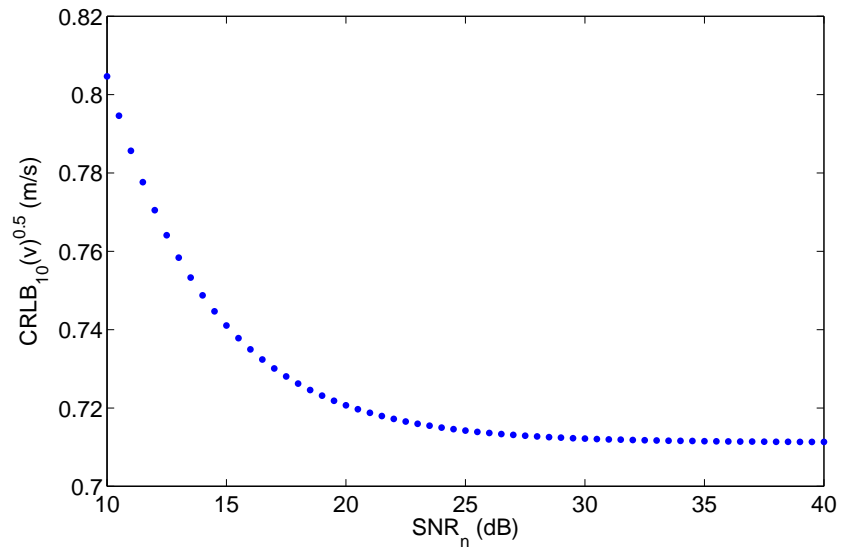


Figure 2.13: Plot of the square root of the Cramer-Rao lower bound for single ping covariance velocity estimates as a function of the  $SNR_n$  for  $N = 10$  snapshots. Signal-to-thermal noise ratio  $SNR_n$  is varied from 10 dB to 40 dB.  $SNR_c \approx 0$  dB as defined by the lag  $k = 65$  used in estimation.

to notice the problem. If two channels are averaged together and only one of them yields velocity estimates which are phase-wrapped, then the average of the two channels is close to zero. A velocity profile from these two elements may have a grouping of estimates near the correct velocity value, another grouping at the negative of that value, and then one final grouping between those two values at  $v = 0$ . As the number of channels averaged increases, and if phase wrapping is to be expected, then this can lead to many more such "groupings" forming between  $\pm v$ , and can confuse the user as to the true nature of the velocity estimates. Some considerations which need to be taken into account are the expected maximum speed of the target(s), and the maximum unambiguous velocity of associated with the transmit waveform.

Furthermore, there may exist a correlation between the received signals across different transducer elements at a common time. If such is the case, then averaging across multiple transducer channels would not introduce more *independent* snapshots. The CRLB for this case would then need to be determined, as the old bound would no longer apply. For these reasons, the decision to average across different transducer channels in forming velocity estimates is a decision which requires careful consideration.

### Filtering, and the Pulse Pair Waveform

When transmitting a pulse pair, it is possible to boost  $SNR_n$  by adjusting the shape of the filter. If the two pulses are separated by  $k_s \geq k_p$ , then by "matched filtering" the returning echo it is possible to boost  $SNR_n$  at the side peaks without introducing correlated noise between the two time samples. Recall that the lag  $k$  at which estimation is performed represents a time difference between the samples in our two-point estimation method, and for the pulse pair is set to  $k = k_p + k_s$ .

Previously, we have discussed filtering the received signals with a wide filter (a wide rectangular filter in the frequency domain), such that we bandlimit the thermal noise while leaving the signal essentially unaffected. In this case, we assume that we have bandlimited the thermal noise to a rectangular shape in the frequency domain, where the noise level  $N_0$  and bandwidth of the bandpass filter is  $2 \cdot BW$  (where  $BW$  is the extent of the filter over positive frequencies). It is easy to calculate that the noise power is equal to  $2\sigma_n^2 = 2N_0 \cdot BW$  while the signal, passing essentially unaffected through the filter, has a power level of  $2\sigma_s^2 =$

$E_t S_R$ . The signal to noise ratio for the case of a wide filter (wf) is then be calculated as

$$snr_{n,wf} = \frac{2\sigma_s^2}{2\sigma_n^2} = \frac{E_t S_R}{2N_0 \cdot BW}. \quad (2.127)$$

Suppose, instead, that we filter the received signals through a filter which is "matched" to one of these pulses such that

$$h[kT_k] = \sqrt{\frac{2}{k_p T_k}} \text{rect}\left(\frac{kT_k}{k_p T_k}\right) \quad (2.128)$$

represents the impulse response of our filter. Assuming a linear system, the discrete-time output of the filter  $y$  when the input is equal to the signal (just the pulses, no additive noise) is the pulse pair convolved with  $h$ . This output,  $y$ , is a function composed to two triangles, each with height 1, width  $2 * k_p T_k$ , and separated by original pulse separation  $k_p + k_s$ . Correlated with itself to yield  $K_y(kT_k)$ , the autocovariance of the output of our linear system (when the signal is the input) is another three peaked structure representing the convolution of triangles. The height of the main peak, representing the power in the signal, is calculated to be  $2\sigma_s^2 = \frac{4}{3}k_p T_k E_t S_R$  and the height of either side peak is half that value.

To determine the filter output when thermal noise is the input, it is easiest to refer to linear systems theory, namely that:

$$K_y(kT_k) = h^*[-kT_k] * h[kT_k] * K_x(kT_k) \quad (2.129)$$

where  $K_x(kT_k)$  is the autocovariance of the thermal noise, in this case. We know that the autocovariance of the noise is a delta function, and can conclude that the resulting autocovariance of the output from the filter,  $K_y(kT_k)$ , is a triangle centered at zero lag with a peak height of  $2\sigma_n^2 = 2N_0$ , representing the power of the thermal noise which contributes to the received echo. For matched filtering, the signal to noise ratio is equal to

$$snr_{n,mf} = \frac{2\sigma_s^2}{2\sigma_n^2} = \frac{4k_p T_k E_t S_R}{6N_0}. \quad (2.130)$$

If we take the ratio  $\frac{snr_{n,mf}}{snr_{n,wf}}$  we calculate that

$$\frac{snr_{n,mf}}{snr_{n,wf}} = \frac{4k_p T_k \cdot BW}{3}. \quad (2.131)$$

Supposing that the wide filter has a bandwidth of  $BW = 4f_c/k_p$ , or four times the bandwidth of the pulse, then matched filtering would result in a received signal where  $snr_n$  which is

16/3 higher than the wide filter case. We can therefore conclude that by widening the pulse length, lowering the sampling period, or widening the bandwidth of the wide rectangular filter in the frequency domain, an increase in the ratio  $\frac{snr_{n,mf}}{snr_{n,wf}}$  is seen.

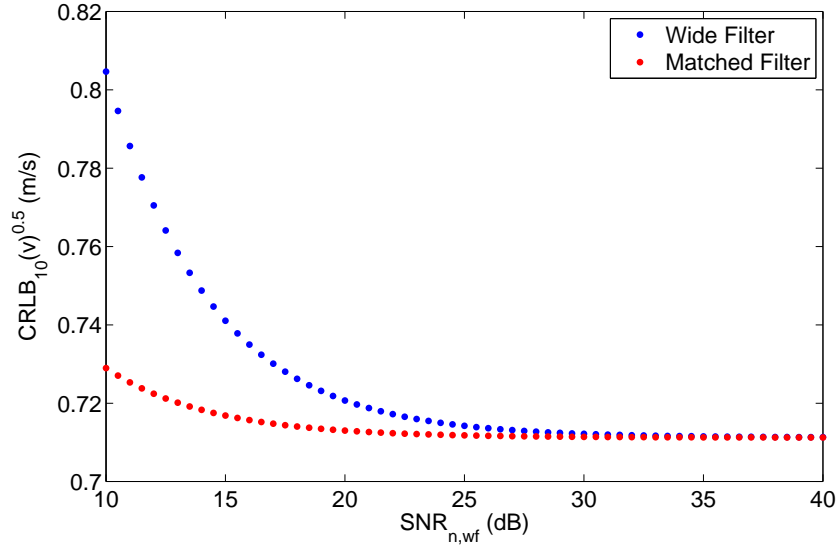


Figure 2.14: Plot of the square root of the Cramer-Rao lower bound for pulse pair covariance velocity estimates as a function of the  $SNR_{n,wf}$  for two types of filtering. The top curve represents the bound on the estimator's RMSE which is attained if a wide frequency-domain filter is used, where the width of the filter is equal to  $BW = 4f_c/k_p$  - four times the bandwidth of the pulse. The bottom curve represents the lower bound on the RMSE of the estimator which is attained if matched filtering is performed on the pulses, where the impulse response of the matched filter is "matched" to either one of the pulses (but not to the pair). Signal-to-thermal noise ratio  $SNR_{n,wf}$  is varied from 10 dB to 40 dB, and  $SNR_c = 0$  dB as defined by the lag  $k = 65$  used in estimation. In this plot, it is assumed that  $snr_{n,mf} = snr_{n,wf} \cdot 16/3$ , implying that  $BW = 4/(kT_s)$ .

Figure 2.14 shows the improvements which are made by employing matched filtering (as described previously) on the pulse pair. Here, we are assuming that estimation is performed at lag  $k = 65$  and that the bandwidth  $BW$  of the wide filter is equal to  $BW = 4/(kT_s)$ , which makes  $snr_{n,mf}$  16 times greater than  $snr_{n,wf}$ . The upper curve represents the  $\sqrt{CRLB_{10}(v)}$  which is attained if a wide filter is applied to the received echoes, while the lower curve represents the  $\sqrt{CRLB_{10}(v)}$  which is attained if matched filtering is performed. This plot shows that under high signal to noise conditions, it is unimportant which filtering scheme is

used. However, at low signal to noise ratios, it is clear that such is not the case - the filtering scheme chosen is highly important. This behavior is expected because as  $snr_{n,wf}$  increases,  $snr_e$  is influenced more by  $snr_c$  than by thermal noise. When the signal-to-thermal noise ratio is high, we therefore expect the matched filtered waveform to perform only slightly better than the wide-filtered waveform. Similarly, as  $snr_{n,wf}$  is lowered we expect it to become a more influential term in determining  $snr_e$ . Such behavior is clearly seen in Figure 2.14.

#### 2.5.4 Estimator RMSE Compared to $\sqrt{CRLB_N}$

Bird and Mullins [3] showed that for a high effective signal to noise ratio, the  $\sqrt{CRLB_N(\gamma)}$  was rapidly approached as the number of independent snapshots  $N$  increased. However, it is frequently the case in velocity estimation problems that  $SNR_e \leq 20$  dB, and therefore the results provided by Bird and Mullins may not always apply. As we have seen, for typical velocity estimation problems  $SNR_e$  is as low as 0 dB, such as when a pulse pair is transmitted and estimation is performed at a side peak. We seek now to explore the behavior of the ratio  $RMSE/\sqrt{CRLB_N(\gamma)}$  as we vary  $SNR_e$ . Note that the present discussion concerns the estimation of phase angles which are then converted into velocity estimates; considering  $\sqrt{CRLB_N(v)}$  rather than  $\sqrt{CRLB_N(\gamma)}$  makes no difference on the ratio which we are calculating. As such, we proceed through the present discussion considering only  $\sqrt{CRLB_N(\gamma)}$ , because it directly concerns the angle estimates which experience the behavior that is to be discussed.

Figure 2.15 shows a plot of the ratio between RMSE (of the angle estimate) and the  $\sqrt{CRLB_N(\gamma)}$  for varying  $SNR_e$ s as a function of the number  $N$  independent snapshots used in estimation. On this Figure, the solid lines have been placed between the actual data points (at integer numbers of  $N$ ) to aid the reader in determining the behavior for each of the cases plotted. Pseudo-random numbers have been generated to form the signal and independent noise terms which were used to generate this Figure. While the noise terms are not only independent of the signal, they are also independent between the two time series (each time series has its own unique noise contribution). The signal present in the second time series is equal to the signal that is present in the first time series, except it is phase-shifted by  $0.03 \cdot \pi$  radians - a very small phase shift. Note that as we change this phase angle, we expect to see a different result for the plot shown in Figure 2.15, because as the angle approaches  $\pm\pi$  and as noise levels increase, phase wrapping becomes more likely

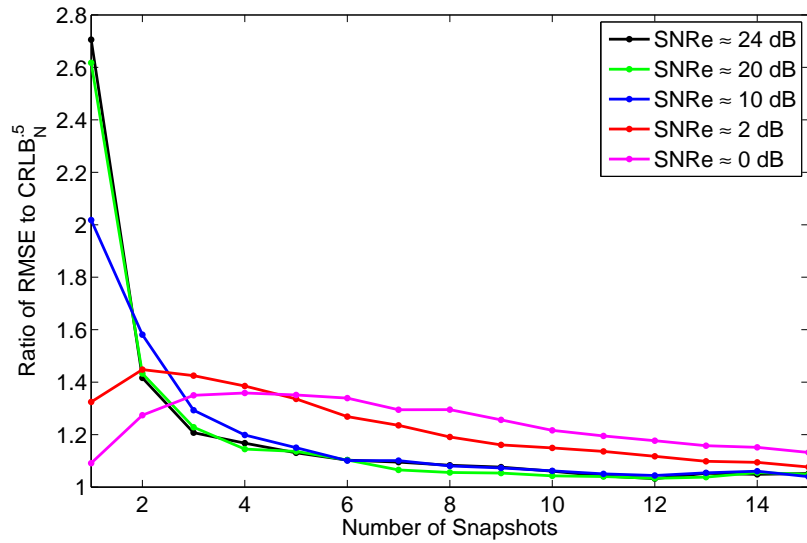


Figure 2.15: Ratio of the RMSE (for angle estimates) to  $\sqrt{CRLB_N(\gamma)}$  versus  $N$ , the number of snapshots used in pre-estimation averaging. From top to bottom, we see the different curves represent the case where  $SNR_e$  is approximately 24 dB, 20 dB, 10 dB, 2 dB, and 0 dB, respectively. For each number of snapshots, 10,000 trials were performed.

to occur. Were we to instead pick a greater phase angle, such as  $\pm 2\pi/3$ , each of the curves will require more snapshots ( $N$ ) than they do at this small phase angle in order to flatten out.

When  $SNR_e = 20$  dB the results calculated by Bird and Mullins are yielded. As  $SNR_e$  lowers, however, different behavior is seen. At first glance it may appear as though superior estimates may be obtained by reducing  $SNR_e$  and only using a single snapshot - but this is not the case. The CRLB represents the theoretical lower limit on the variance of an unbiased estimator, so it cannot be the case that our angle estimates improve beyond the CRLB as  $SNR_e$  becomes progressively lower.

Instead, as  $SNR_e$  lowers and the CRLB grows larger, the RMSE of the angle estimator does not increase in the same manner. Since angle estimates must fall within the range  $(-\pi, \pi)$ , the RMSE for such angle estimates is eventually bounded once angle estimates are uniformly distributed across the range. In other words, there occurs a threshold above which the RMSE for angle estimates cannot go; no such threshold exists for the CRLB. We can therefore conclude that when  $SNR_e$  drops, the CRLB increases without bound - meanwhile the RMSE of the estimator increases towards a finite number, resulting in the ratio  $RMSE/\sqrt{CRLB_N(\gamma)}$  becoming smaller once this threshold has been reached. As RMSE increases beyond some value, the comparison between RMSE and the  $\sqrt{CRLB_N}$  becomes less valid. We seek to estimate this point.

We wish to determine how many snapshots are needed, when  $SNR_e = 0$  dB, such that we have not yet reached the point where RMSE becomes a poor indicator of the behavior of our velocity estimator. By determining the point of inflection for the RMSE to  $\sqrt{CRLB_N(\gamma)}$  ratio, we can estimate the minimum number of snapshots which are required in order to have a valid comparison between RMSE and  $\sqrt{CRLB_N(\gamma)}$ . The interested reader can refer to [3] for more discussion on this general topic, and on the probability density function which governs the angle estimates which are converted into velocity estimates.

Figure 2.16 shows a ratio (again, RMSE for velocity estimates to  $\sqrt{CRLB_N(\gamma)}$ ) curve which pertains to two of the estimators considered in this thesis: the single ping covariance monopulse and pulse pair VEMs. When the test monopulse is 130 cycles in length, and  $k = 65$ , then  $SNR_e$  is 0 dB; such  $SNR_e$  is also the case when a pulse pair is transmitted. Here we see that the point of inflection is at approximately  $N = 4$  snapshots, corresponding to the case where  $RMSE \approx 1.67$  m/s for the velocity estimate, or  $\approx 52$  degrees for the corresponding angle estimate. We conclude that when estimating the phase change which will

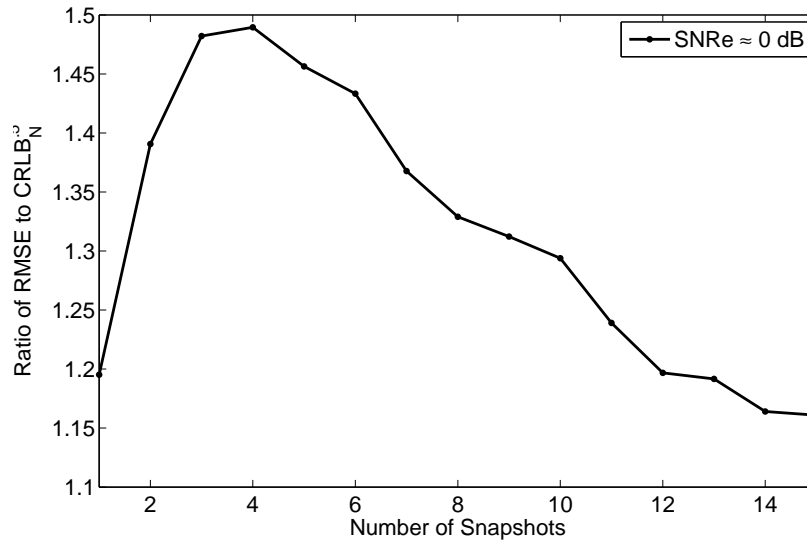


Figure 2.16: Ratio of the RMSE of angle estimates to  $\sqrt{CRLB_N(\gamma)}$  versus the number of snapshots used in pre-estimation averaging  $N$ , for  $SNR_e = 0$  dB. For each number of snapshots, 10,000 trials were performed. A phase angle of  $\pi \cdot .357$  radians and a lag of  $k = 65$  were assumed, corresponding to a 4-knot target.

be used for form a velocity estimate, once the error increases beyond  $RMSE > 52$  degrees we can no longer discuss the performance of our estimator (either the angle estimator, or the velocity estimates which it then produces) by comparing RMSE to the  $\sqrt{CRLB}$ .

In the case of ping pair covariance processing, where  $SNR_e \approx 24$  dB and  $N = 10$  snapshots, we expect this ratio to be much closer to 1. Figure 2.17 shows the behavior of this ratio as the number of snapshots increases, and indeed our predictions are confirmed. At this high  $SNR_e$ , fewer snapshots are required in order for the RMSE of the estimator to be essentially equal to the  $\sqrt{CRLB_N(\gamma)}$ . At ten snapshots ( $N = 10$ ), this ratio is equal to 1.06 and is seen to asymptotically approach a value of 1 as  $N$  increases. Bird and Mullins describe the expected theoretical trend in [3], and close agreement with theory is observed.

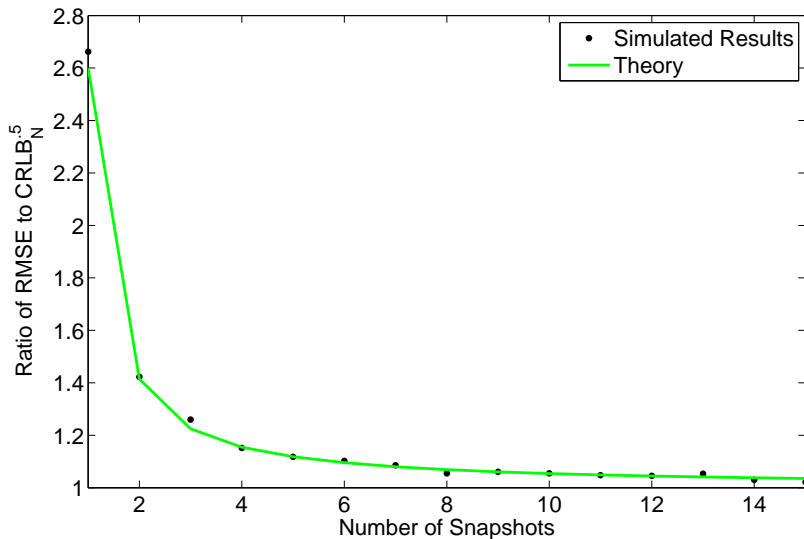


Figure 2.17: Ratio of the RMSE of angle estimates to  $\sqrt{CRLB(\gamma)}$  versus the number of snapshots used in pre-estimation averaging  $N$ , for  $SNR_e \approx 24$  dB. Black dots indicate the simulated results, and the green line indicates the theoretical prediction for any given  $N$  value. For each number of snapshots 10,000 trials were performed. The angle which was being estimated was approximately zero degrees.

We now conclude our discussion of the relevant theory behind velocity estimation, and turn our attention towards simulation. The covariance functions for a range spread target have been developed, have been used to explain each VEM in mathematical terms, and

finally have been used to calculate the theoretical performance limitations for the covariance velocity estimators. Our next task is to leave the realm of theory and to begin demonstrating the performance of these methods in simulation.

## Chapter 3

# Simulation

Having completed our discussion of the relevant theory, we now seek to employ computer simulation to help validate the theoretical models, as well as to provide a glimpse into what sort of performance to expect from each VEM. As is usually the case in modern scientific or engineering endeavors, simulation is employed prior to experimentation as an inexpensive and easy means by which to justify some action or provide proof of concept. We begin by describing the simulator which has been created to model the seafloor and the sonar wave transmission. Next, we prove that this model agrees with the relevant theory outlined in the preceding Chapter. After establishing that the simulation acts in accordance with the theoretical model, we then seek to demonstrate the performance of each estimator with simulated data.

Two simulator programs have been constructed: one which models the transmission and reception of a monopulse, and one which models the transmission and reception of a pulse pair. These simulators mimic the formation and reception of echoes off of the seafloor, and serve to create time series which are later used for processing. The only difference between these two simulators is the manner in which echoes are simulated to arrive back at the receiver (due to the differences in the pulses). Each simulator assumes a flat seafloor which extends 100 m in front of the boat, and assumes that this seafloor is at a constant depth of 20 m below the transducers. The transducer array is tilted at a downward angle,  $\theta = 20$  degrees below the horizontal, and is facing directly ahead (off the bow of the vessel). The transducer array is composed of six elements, each at half-wavelength spacing from adjacent elements, and the carrier frequency is 300 kHz. Although in "real life" the speed of sound in water varies depending upon temperature, depth, and salinity [7] for the simulator we'll

simply assume that the speed of sound in water is constant at 1500 m/s. The monopulse simulator mimics the transmission of both a 130- and 150-cycle monopulse, while the pulse pair simulator mimics the transmission of two 30-cycle pulses, with the tail of the first pulse being separated by 35 cycles of dead time from the head of the second pulse. Ten pings are transmitted for each chosen configuration of boat velocity and SNR.

While many types of pulses are possible, these "test pulses" have been chosen for specific reasons. We have already seen that the CRLB tightens as the length of the pulse grows (assuming that estimation is performed at the optimal lag), and for this reason alone, we would choose far longer pulses. However, as pulse length increases range resolution decreases. Since we are concerned with bathymetric sonar systems (and since we may wish to localize a target in practice) we compromise by selecting a monopulse length of 150 cycles. With both pulses, the usage of a pulse which is too long will either require estimation to be performed at a sub-optimal lag, or will potentially introduce phase wrapping if estimation is performed at too great a lag. It is for these reasons that the relatively short pulse pair and monopulse have been selected.

Figure 3.1 shows a forward-looking sonar array mounted on a forward-moving vessel. The transducer array boresight (101) is tilted at some downward angle  $\theta$  and the transducer array sends out a monopulse (102). This basic physical setup will be frequently referred to throughout the text, and it describes the physical situation which is being modeled.

### 3.1 Confirming Agreement With Theory

We now seek to show that the simulation developed by the author agrees with the theoretical models outlined by Van Trees [25], as well as to show agreement with the correlation functions which have been derived by the author. We begin with the slowly fluctuating point target.

#### 3.1.1 Slowly Fluctuating Point Target

Let us proceed by seeking to simplify Equation 2.21 as much as possible. Our objective is to demonstrate that the simulated received echo returning from a slowly fluctuating point target agrees with the related theory. The expression for a slowly fluctuating point target

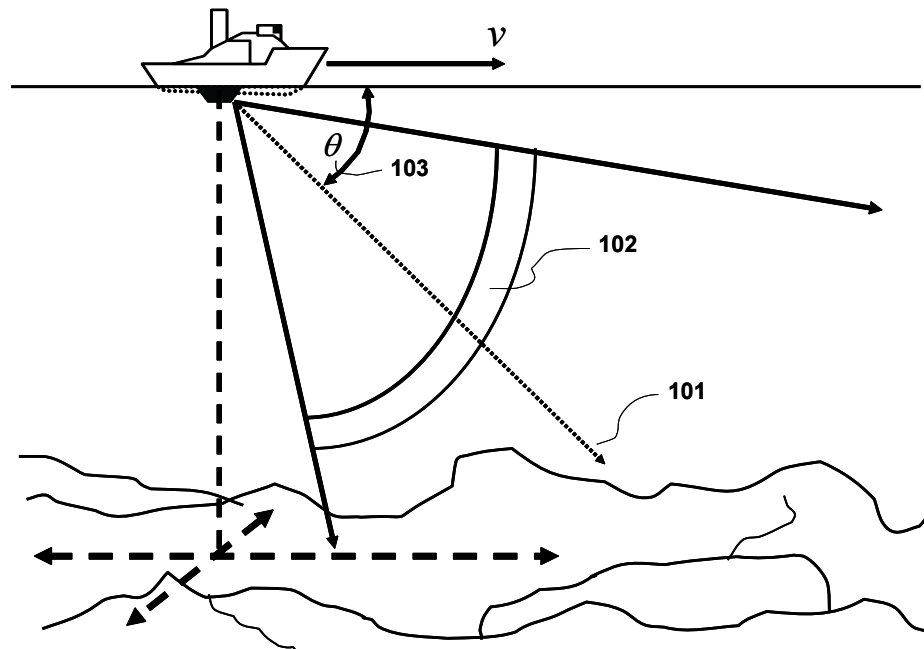


Figure 3.1: Diagram of a typical forward-looking sonar array mounted on a vessel.

is written as:

$$\tilde{s}_r(t) = \tilde{A}\tilde{f}(t - \tau)e^{-jw_c\tau_0}e^{jw_at} + \tilde{n}(t). \quad (3.1)$$

We are now neglecting scaling factors such as signal power, transducer gain, and spreading loss in favor of treating only the complex amplitude  $\tilde{A}$  of the single slowly fluctuating point target. These scaling factors have been dropped because they do not need to be considered in order to validate the performance of the simulator in terms of the theoretical models previously developed, of which phase is certainly the "essence" of the problem at hand. Examining the envelope term,  $\tilde{f}(t - \tau)$  we realize that for present-day URL operations all transmitted pulses are square pulses. Assuming that all square pulses are "ideal" (that their edges are infinitely sharp) then the envelope is a *rect* function which assumes a value of either 0 or 1. In other words, without the addition of noise our received echo is either zero or

$$\tilde{s}_r(t) = \tilde{A}e^{-jw_c\tau_0}e^{jw_Dt}. \quad (3.2)$$

In practice, the carrier frequency would first be modulated with the baseband signal (which, for the URL, would be a monopulse or pulse pair) and then upon reception of the returning echo, the carrier  $e^{jw_ct}$  would be removed - leaving only the baseband signal. In simulation, the carrier is never considered; we are working with the complex baseband signal.

Let us now explore two numerical examples. Consider a two-dimensional plane, within which is located one slowly fluctuating point target and a single transmit and receive transducer. For this numerical example, we seek to simplify the simulation model as much as possible and to add complexity later as necessary. We therefore consider a case which is even simpler than the one outlined in Figure 3.1, since we are considering only a single point scatterer rather than an ensemble of scatterers. Suppose that the receive transducer element is located at the origin and is facing the point scatterer, and that the element and scatterer are separated in range by 45 m at time  $t = 0 \equiv t_0$ . Let's assign the scatterer some complex amplitude such that  $\tilde{A} = \sqrt{E_t}\tilde{b} = 0.4 - j0.3$ .

### Zero-Velocity Boat

In the event that the boat and scatterer are static relative to one-another, the Doppler term  $w_D = 2vw_c/c$  is zero because  $v = 0$ . This means that when the received signal is

non-zero in amplitude, as dictated by the envelope function  $\tilde{f}(t - \tau)$ , our received signal is simply the quantity  $\tilde{A}e^{-jw_c\tau_0}$ . In the case of a transmitted monopulse, the envelope is 150 cycles in duration. The sampling frequency  $f_s$  is chosen to be equivalent to the carrier frequency, such that  $f_s = f_c = 300000$  Hz. This sampling frequency implies that a reflection of the transmitted signal is sampled once per cycle, such that the reflection of a 150 cycle monopulse off of a point target should be present for 150 samples in the received time series. For the present examples, where only one slowly fluctuating point target is simulated, we expect the received time series to be all noise save for 150 samples which contain an echo from the single scatterer.

Aside from just checking that the amplitude and Doppler phase variation of the received signal are correct, let us also check that the signal is received at the theoretically correct moment in time. Since we know that the target is 45 m away from the boat, and that there is no motion between the two, we can predict a round trip of exactly 90 m. With sound traveling at 1500 m/s, the echo should begin to arrive at the transducer at time  $t = 90/1500 = 0.06$  s, and the echo should have a duration equal to the pulse length  $T_p = 150/300000 = 0.5$  ms. Equivalently, the echo should arrive at time sample number  $n = 0.06 * f_s = 18000$  (where  $f_s = 300000$  is the sampling frequency) and should last until time sample number  $n = 18000 + 149 = 18149$ .

If we ensonify this simulated scatterer by sending out a monopulse, we'd expect to see a returning echo (with a duration equal to the length of the pulse) arrive at a time that corresponds to the two-way travel distance of the signal. If, instead, we sent out a pair of pulses then we'd expect to see a pair of echoes with durations equal to the length of the two pulses. These two pulses would arrive at times which correspond to two-way travel times, and would be separated by the time delay between pulses.

Turning now to Figure 3.2 we see that the phase and amplitude of the simulated return echo agree with the phase and amplitude of the theoretically modeled echo. At the time when echoes begin to be received from the scatterer,  $\tau_0$ , we expect the received signal to be equal to

$$\tilde{s}_r(\tau_0) = \tilde{A}e^{-jw_c\tau_0}e^{jw_D\tau_0} \quad (3.3)$$

$$= (0.4 - j0.3)e^{-jw_c*0.06}e^{j*0*\tau_0} \quad (3.4)$$

$$\approx 0.4 - j0.3. \quad (3.5)$$

Examining the simulated time series, the echo is seen to begin at time sample number

$n = 18000$  and ends at time sample number  $n = 18149$ , and agrees with the theoretically predicted phase and amplitude. The simulator produces results which agree with Van Trees' theory, yielding the expected signal phase and amplitude at the expected times, thus proving that the monopulse simulation accurately models physical behavior for a slowly fluctuating (stationary) point target. Note that the theoretically predicted returning echo is modeled as though a continuous wave had been transmitted, and not a pulse. This is done so that the reader may more easily compare simulation with theory on this (and subsequent) plots.

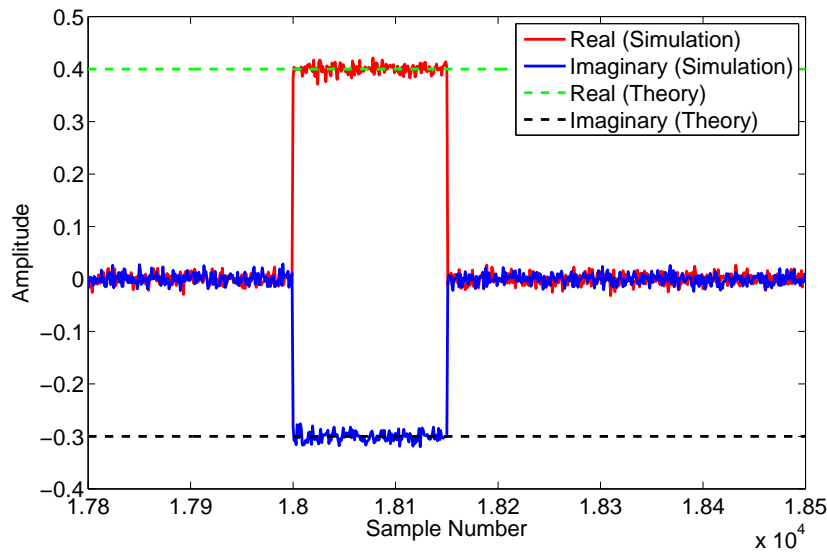


Figure 3.2: Comparison of the received signal predicted by Van Trees' theoretical model [25] and monopulse simulation. A signal-to-thermal noise ratio of 40 dB is modeled.

Let us now turn our attention to the case of a pulse pair. Keeping the simulation similar to the case of the monopulse, but substituting a pulse pair for a monopulse as the transmit waveform, we repeat the experiment. As stated earlier, let us assume that each pulse in the pair is 30 cycles in length and that the two pulses are separated by a dead time of 35 cycles. We'd expect the echo from the scatterer to be observed at exactly the same time it was in the case of the monopulse, but to have two distinct echoes appear in the time series: one from the first pulse, and one from the second pulse. We know that the first pulse arrives at time  $t = 0.06$  s or  $n = 18000$  samples, and lasts 29 cycles until time  $t = 0.0601$  or sample number  $n = 18030$ . Then follow 35 cycles of dead time during which no echo should be received,

with the second echo beginning at time  $t = 0.06021667$  or sample number  $n = 18065$  and ending at time  $t = 0.06031667$  corresponding to sample number  $n = 18095$ .

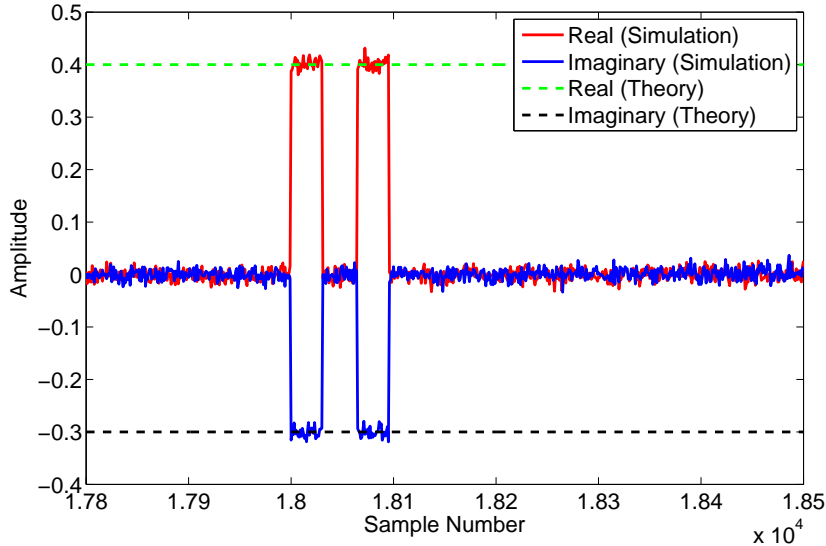


Figure 3.3: Comparison of the received signal predicted by Van Trees' theoretical model [25] and pulse pair simulation.

From Figure 3.3 we can see that the phase and amplitude of the simulated received signal agree with theory. In the simulation, the first observation of the echo is seen to begin at time sample  $n = 18000$  and to last until time sample  $n = 18030$ . Following this first observation are 34 samples which contain only noise and no echo, until the second echo begins at time sample  $n = 18065$  and lasts until time sample  $n = 18095$ . It is now concluded that the pulse pair simulator is also in agreement with Van Trees' theoretical model in the case of a slowly fluctuating (and stationary) point target.

### Non Zero-Velocity Boat

So far we've taken Van Trees' theoretical model for the received echo of a slowly fluctuating point target and represented it as

$$\tilde{s}_r(t) = \tilde{A}\tilde{f}(t - \tau)e^{-jw_c\tau_0}e^{jw_d t} + \tilde{n}(t)$$

considering only the case where both target and source are stationary relative to one-another. We now wish to extend our example to the case where the target and source are no longer static relative to one-another. The Doppler sonar being designed by the URL is designed to be tolerant of no more than a 10 knot relative velocity between source and target. With this limitation in mind, let us verify that the simulation performs in agreement with theory at the limit of its applicability: a sonar system moving with a speed of 10 knots (5.1444 m/s) relative to the target which it is ensonifying. At this speed, the Doppler frequency is no longer zero but is  $w_D = 2vw_c/c = 1.2922 * 10^4$  rad/s.

This non-zero Doppler frequency serves to "rotate" the phase of the received signal as a function of time. When there is no motion between target and source, no phase rotation is observed. However, as the magnitude of this radial velocity between target and source increases, so will the rate of phase rotation. In this case, where the source is approaching the target at a speed of 10 knots, the received echo is:

$$s_r(t) = \tilde{A}\tilde{f}(t - \tau)e^{-jw_c\tau_0}e^{jw_D t} \quad (3.6)$$

$$\approx (0.4 - j0.3)\tilde{f}(t - \tau)e^{j*12922*t}e^{-jw_c*0.06} + \tilde{n}(t). \quad (3.7)$$

Since we assume that the target is stationary, the signal still takes  $t_1 = 45/1500 = 0.03$  s to arrive at the scatterer, but the return time is shortened due to boat motion. When the signal hits the target, the boat has moved from its initial position  $x_0 = 0$  to the position  $x_0 + vt_1 = 0.1543$  m, where in this case  $v = 5.1444$  m/s. On the return trip, both the sound and the boat are acting to close the distance between the target and the source, such that the closing speed is not just the speed of sound 1500 m/s but is instead  $1500 + v_{boat} = 1505.1444$  m/s. The round trip distance of the signal is therefore:

$$\begin{aligned} d_{rt} &= 45 + 1500 * \frac{45 - vt_1}{1500 + v} \\ &= 45 + 1500 * \frac{44.846}{1505.1444} \approx 89.7m \end{aligned} \quad (3.8)$$

which implies that in the case of a monopulse, the echo is observed from time  $t = 0.059795$  s to time  $t = 0.0602946$  s or samples number  $n = 17938$  to  $n = 18087$ . In the case of a pulse pair, we expect the first echo to be observed between times  $t = 0.059795$  s and  $0.05989$  s (or samples 17938 and 17967) while the second echo is observed between times  $0.06001$  s and  $0.06011$  s (samples 18001 and 18030). Note that we have now effectively treated the  $\tilde{f}(t - \tau)$  envelope term, as it causes the received signal to be either zero or one, and we may now drop this term from our consideration.

As shown in Figure 3.4, simulation and theory are again in agreement, this time agreeing in the received echo which corresponds to a non-static source. Dashed green and black lines represent the values of the real and imaginary components (respectively) of the returning signal predicted by Van Trees' theory. Solid red and blue lines represent the simulated value of the real and imaginary components (respectively) of the received echo. Van Trees' theoretical predictions have been shown here to not reflect the envelope of the transmitted signal but instead to represent the return which would be observed if a continuous wave were transmitted. Since the simulation is not modeling the transmission of a continuous wave but rather the transmission of a 150-cycle monopulse, we can see the envelope of the transmitted signal reflected in Figure 3.4. The simulated echo is observed between time samples 17938 and 18087 and agrees with our predictions and with Van Trees' theory.

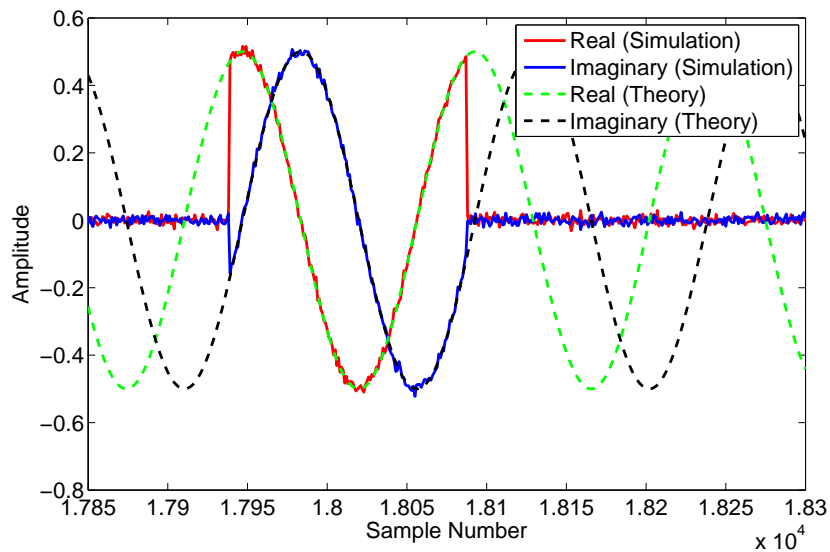


Figure 3.4: Comparison of the received signal predicted by Van Trees' theoretical model [25] the received echo produced via simulation for a monopulse. A signal-to-thermal noise ratio of 40 dB is assumed, and the source is modeled to be moving at 10 knots towards the target.

Referring now to Figure 3.5, it is seen that the simulator also produces results which agree with theory in the case of a pulse pair and moving transmitter. As with Figure 3.4, the dashed green and black lines represent the theoretically obtained values of the real

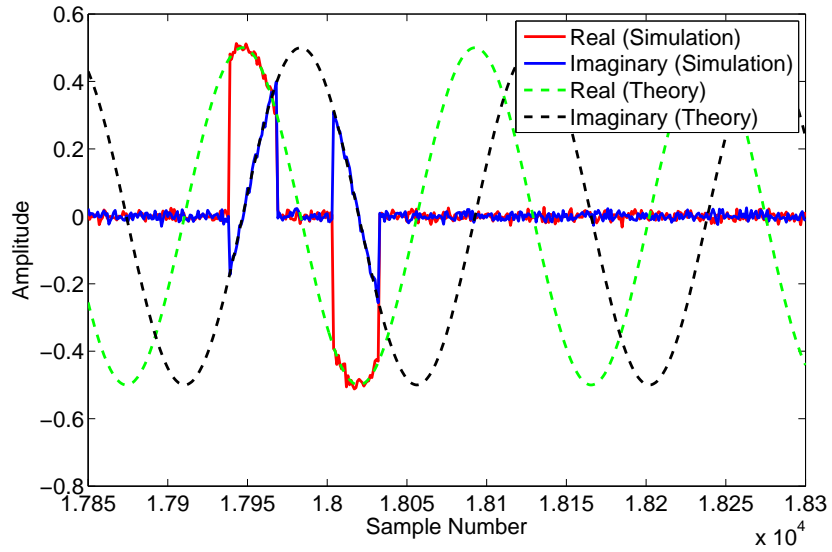


Figure 3.5: Comparison of the received signal predicted by Van Trees' theoretical model [25] and simulation for a pulse pair. A signal-to-thermal noise ratio of 40 dB is assumed, and the source is modeled to be moving at 10 knots towards the target.

and imaginary components of the received signal. This time, it is slightly more difficult to interpret the graph due to the shorter nature of the transmitted pulses which are being compared to their continuous-wave theoretical values. However, it is seen that the first echo begins and ends at  $n = 17938$  and  $n = 17967$ , respectively, and that the second echo begins and ends at  $n = 18001$  and  $n = 18030$ , respectively. As with the case of the stationary target and source, a "dead time" is observed between the two pulses during which no simulated echo appears. This dead time in the echo corresponds directly to the dead time between pulses in the simulator, but has not been included in the theoretical model.

### 3.1.2 Correlation Functions: Range-Spread Target

One further verification is provided: that the theoretically predicted correlation functions are consistent with the correlation functions obtained via simulation for a range-spread target. A range-spread target is assumed in the form of a seafloor that is 50 m long and is composed of random Gaussian scatterers at a uniform density of 100 scatterers per meter of seafloor. To aid in comparison between simulation and theory, and to aid the calculation of the radial velocity of the scatterers, the seafloor is assumed to be at the same level as the transducer. For our purposes we make this assumption purely to make the radial velocity of the seafloor (relative to the transducer) equal to its horizontal velocity.  $SNR_n$  is maintained at 40 dB, while the carrier frequency  $f_c$ , sampling frequency  $f_s$ , and all pulse parameters are unchanged since the previous simulations.

We are seeking to verify the general covariance functions

$$\begin{aligned} K_{\tilde{s}_1 \tilde{s}_1}(kT_k) &= E_t S_R \rho_{c,a}(kT_k) e^{jw_D kT_k} + 2\sigma_n^2 \cdot \rho_n(kT_k) \\ K_{\tilde{s}_1 \tilde{s}_2}(kT_k) &= E_t S_R \rho_{c,c}(kT_k) e^{jw_D(kT_k - T_p)}. \end{aligned}$$

which correspond to an auto and cross covariance, respectively, of the received time series from a range spread target. For easy comparison with simulation, let us assume that the product  $E_t S_R = 1$  and that the noise power  $2\sigma_n^2 \ll 1$  is low compared to the signal power, making the peak of either covariance function have a maximum value of essentially 1. It is now easy to plot and compare both the theoretical and simulated covariance functions in a meaningful way.

We begin by considering the autocovariance and cross covariance (across pings) of a received time series from a source and seafloor which are static relative to one-another, and then continue to the case where they are not static. Figure 3.6 shows that simulator and

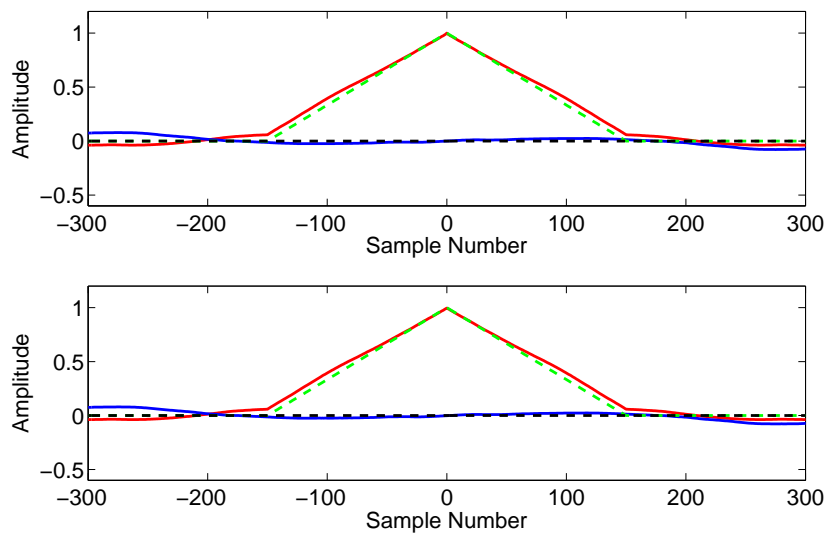


Figure 3.6: Comparison between theory and simulation for the autocovariance (top plot) and cross-covariance (bottom plot) functions, for a monopulse hitting a stationary target. Dashed lines represent the theoretical predictions (green representing the real component, and black representing the imaginary component) while solid lines represent the simulated covariance functions (red lines for the real component, and blue lines for the imaginary component). A signal-to-thermal noise ratio of 40 dB is assumed, and the source is modeled to be stationary relative to the target. 10000 samples of the received time series have been used to form these covariance functions in the simulator.

theory are in agreement with the autocovariance (top plot) and cross covariance (bottom plot, representing the covariance between two pings) for a monopulse. We note that both the top plot and bottom plot appear to be the same - this is because the scatterers contributing to the echo have not moved, so the only difference between an auto- and cross-covariance, in this case, is that the cross covariance includes a second ping which has a noise contribution that is independent from the first ping. Towards the center of the peak (near  $k = 0$ ) agreement between simulation and theory is strong, while this agreement becomes less strong as  $|k|$  moves away from zero. If the contribution of thermal noise is dismissed, then both the upper and lower plots represent an autocovariance of the received time series. Therefore, at lag  $k = 0$ , we expect to find perfect agreement with theory. As  $k$  moves away from this point, we are correlating time samples with other time samples that are increasingly uncorrelated, so we expect to see random behavior begin to dominate the simulated covariance functions.

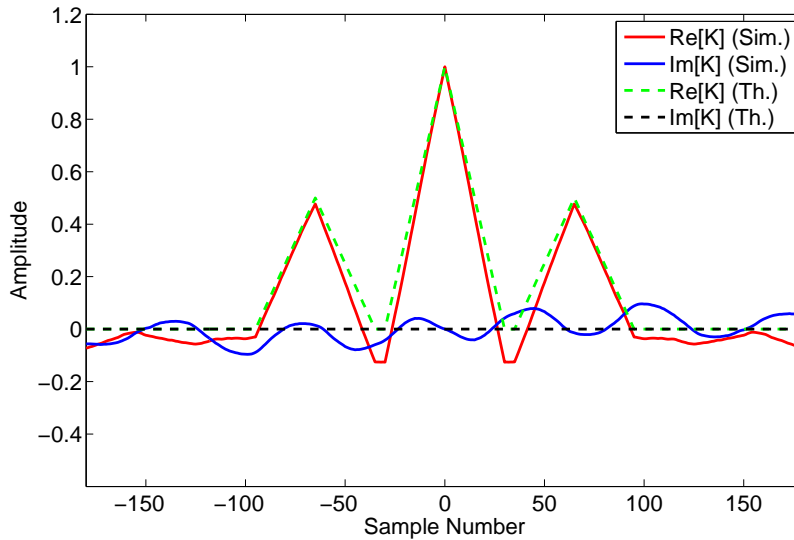


Figure 3.7: Comparison between the theoretically predicted autocovariance function (dashed lines) and the simulator-generated autocovariance function (solid lines) for a pulse pair incident upon a stationary target. A signal-to-thermal noise ratio of 40 dB is assumed, and the source is modeled to be stationary relative to the target. Again, 10000 samples of the received time series have been used to form this covariance function in the simulator.

In Figure 3.7 we see the theoretically predicted autocovariance (dashed lines) compared to the simulated autocovariance (solid lines) for a pulse pair. The cross-correlation is not

considered, because it is not used by any of the velocity estimation methods discussed herein. In this Figure, we again see relatively strong agreement with theory at lag  $k = 0$ , and we see this agreement deteriorate as the magnitude of  $k$  increases from zero. Inside of each side peak we can see some phase variation, but this variation is small in magnitude. Again, were a shorter time series to be used we would see this effect exaggerated, and similarly a longer time series would diminish this effect.

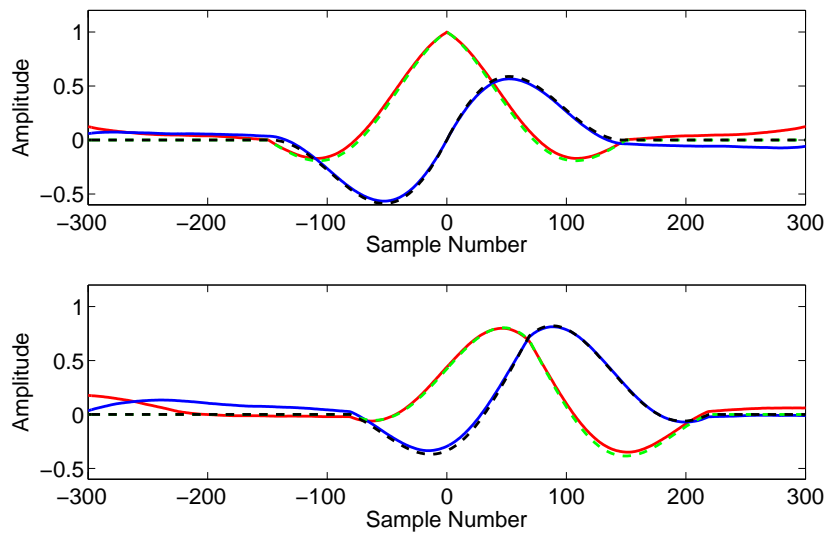


Figure 3.8: Comparison between the theory and simulation for the autocovariance (top plot) and cross-covariance (bottom plot) functions, for a monopulse incident upon a 5-knot target. Dashed lines represent the theoretical predictions (green representing the real component, and black representing the imaginary component) while solid lines represent the simulated covariance functions (red lines for the real component, and blue lines for the imaginary component). A signal-to-thermal noise ratio of 40 dB is assumed, and the source is modeled to be stationary relative to the target. 10000 samples of the received time series have been used to form these covariance functions in the simulator.

In Figure 3.8 we see the auto- and cross-covariances (top and bottom plots, respectively) for the received time series caused by a 5 knot target being ensonified by a monopulse. Again, agreement with theory tapers off as  $k$  progresses to values outside of the main peak, but is fairly strong inside the main peak. We see that the phase at the center of the autocovariance is again zero, but this time we observe what appears to be sinusoidal

behavior of the changing phase. This makes sense, because we have found theoretically that a non-zero velocity scatterer returns a signal influenced by the exponential Doppler term  $e^{j\omega_D k T_k}$  in the case of an autocovariance, or  $e^{j\omega_D (k T_k - T_p)}$  in the case of a cross-covariance. The peak of the autocorrelation still occurs at a lag of zero, and is still twice the width of the pulse. The cross-covariance, on the other hand, has a shifted (magnitude) peak which is now at a lag of approximately  $k \approx 70$  and has a non-zero phase at its center. Since the signal to thermal noise ratio is so high, we expect to see near-perfect agreement with theory at some point on the cross covariance function. This is because the scatterers have not changed amplitude (aspect angle is constant in this simulation) but simply position - therefore, when a lag  $k$  is arrived at which accurately represents the difference in two-way travel times between pings, the two signals are perfectly correlated (if we ignore thermal noise). This example is provided not to suggest that the ping pair covariance method is capable of resolving (at this carrier frequency and  $T_p$ , and without a phase unwrapping algorithm) such velocities, but to illustrate the proper functioning of the simulator.

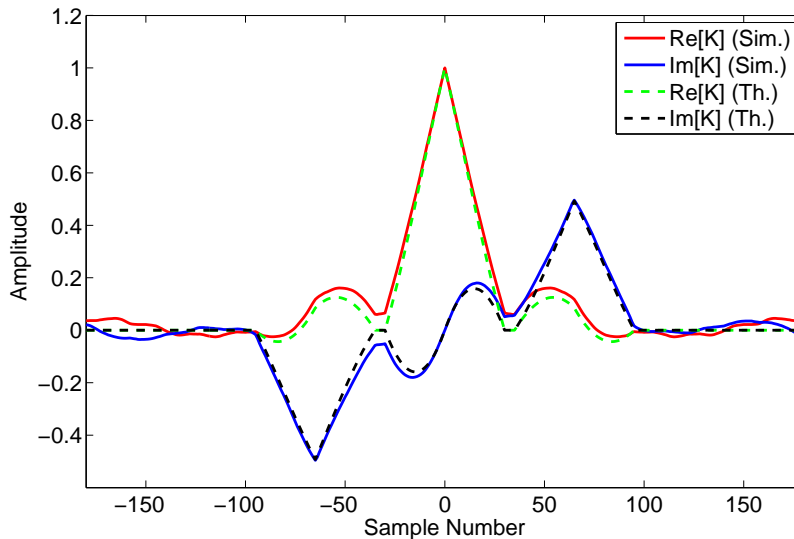


Figure 3.9: Comparison between the theoretically predicted autocovariance function (dashed lines) and the simulator-generated autocovariance function (solid lines) for a pulse pair incident upon a 5-knot target. A signal-to-thermal noise ratio of 40 dB is assumed, and the source is modeled to be stationary relative to the target. Again, 10000 samples of the received time series have been used to form this covariance function in the simulator.

Finally, we confirm agreement with theory in the case of the pulse pair being incident upon a 5 knot target. Figure 3.9 shows that while the three-peaked structure has not shifted from being centered at lag  $k = 0$ , the phase of the covariance function inside each peak is now clearly not constant and is non-zero. This time, due to the boat's motion, we expect the phase inside each side-peak to be non-zero, and we now see how the phase of the side peaks changes in response to target motion and is used to form velocity estimates.

It is concluded that the simulators, for both the monopulse and pulse pair, work in accordance with the theory that was derived in the previous Chapter. We have previously seen the simulators produce results which agree with theory for the received signal from a single scatterer. Now, we have also seen the simulators produce results which agree with the theoretical covariance functions that have been derived. We thus turn our attention to evaluating the velocity estimation methods in simulation, having concluded that such simulations behave in accordance with our theory.

## 3.2 Velocity Estimation

We now begin our analysis of each velocity estimation method in a simulated environment. Since we are presently not concerned with water column targets (such as fish) and seek only to evaluate each method in the simplest of cases, we model the setup outlined in Figure 3.1. Many subsequent Figures in the present Chapter bear the same basic format: they are plots of velocity versus range, with a comparison being made between theory and estimation. The green line always indicates the theoretical radial velocity which the program is seeking to estimate, and all estimates are denoted by blue dots.

For reasons which will become apparent later, a brief review of the concept of radial velocity is provided. From the reference frame of the boat, surface targets which lie in the boat's path are seen to have a closing speed which is equal to the boat's speed. Targets which lie directly behind the boat are seen to move away from the boat, again with a speed equal to the speed of the boat. If an observer were then to look directly below the boat at a flat seafloor, it would be apparent that the flat seafloor was moving underneath the boat but was not closing the distance between them. In other words, a surface target in front of the boat has a positive (closing) radial velocity, a seafloor scatterer directly below the boat has zero radial velocity relative to the boat, and a surface target directly behind the boat has a negative radial velocity equal in magnitude to the speed of the boat. This

implies that when a boat-mounted transducer array sends out a ping and receives echoes from seafloor scatterers, any ensonified scatterers which lie behind the boat are perceived to have negative relative radial velocities while those in front of the boat have positive radial velocities.

If seafloor scatterers are at a depth of 20 m when a ping is transmitted, initial echoes originate from the scatterers which are closest to the boat (i.e. those which are located directly below it, assuming a flat seafloor). The perceived radial velocity from these scatterers is close to zero, with ensonified scatterers in front of the boat appearing to have slightly positive radial velocities and those behind having slightly negative radial velocities. This is what leads to the curve in the green line on all velocity estimation plots which represents the theoretical radial velocity. As the pulse travels to ranges greater than the depth of the seafloor and hits scatterers located further in front or behind the boat, the theoretical radial velocity increases in magnitude. For a forward-looking transducer array, echoes eventually cease to be received from aft of the vessel but continue to be received from ahead of the vessel. Such is the case with the simulations which have contributed to the data reported herein, and therefore all "thick green lines" corresponding to scatterer theoretical radial velocity have a negative component near 20 m which quickly discontinues as echoes from aft of the ship cease to be received by the transducer.

In simulation, it is easy to limit the amount of returns which are received from aft of the vessel. We begin by assuming that in practice, the construction of the transducer and its housing physically prevent echoes from being received which are incident from angles of  $\pm\pi/2$  from the "boresight" of the array. Further, by assuming a cosine beam pattern (in other words, by scaling the scattering amplitude of seafloor scatterers by their angle off of boresight) we can scale the echo which is received from the scatterers.

To quantify the agreement between the theoretical radial velocity of bottom scatterers and between the estimated radial velocity of bottom scatterers at some range, root mean-squared error (RMSE) is calculated. This quantity can then be compared to the  $\sqrt{CRLB}$  values which were calculated in the previous Chapter.

The reader will recall that only two VEMs are capable of directly estimating velocities of up to 10 knots: the ping to ping incoherent VEM, and the single ping covariance VEMs. In this thesis, we assume that no phase unwrapping is performed - hence, the maximum velocity for the ping pair covariance approach that we consider is its maximum *unambiguous* velocity. For completeness, this method is discussed in the present Chapter, and although

it is unable to measure (under our previous assumption about phase wrapping) such macro velocities as a 10-knot target, this method is not quickly dismissed and will "resurface" later in the thesis.

### 3.2.1 Ping Pair Incoherent

We now consider the ping pair incoherent VEM, and evaluate its performance with simulated data. At a boat speed of 5 knots and high  $SNR_n$  (40 dB), the performance of this method is seen to be quite reasonable.

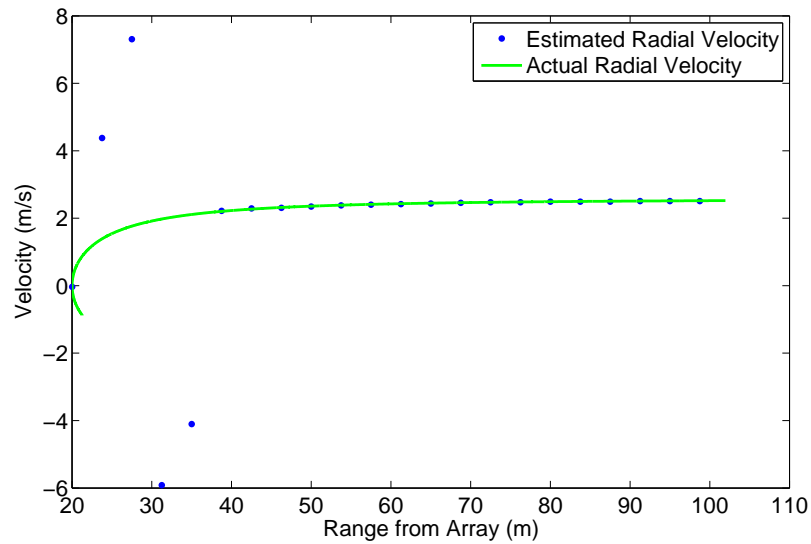


Figure 3.10: The ping pair incoherent VEM with boat speed held at 5 knots ( $\approx 2.57$  m/s) and an  $SNR_n$  of 40 dB (at long range). A 150 cycle monopulse has been assumed, and averaging was performed across 1500 samples.

Figure 3.10 shows the performance of the ping pair incoherent VEM with a high  $SNR_n$  and a moderate boat velocity. The solid green line represents the theoretical radial velocity of the seafloor relative to the transducer array, and the blue dots represent the velocity estimates produced by this VEM. In this and subsequent Figures, radial velocity is plotted as a function of range from the transducer array. With the bottom simulated as being 20 m below the array and with no water column targets (nor anything else in the water which would cause a reflection) it is easy to understand why the first velocity estimates begin to

appear after a range of 20 m when the pulse hits the bottom.

Under such conditions as high  $SNR_n$  and moderate boat speed, it is evident that this VEM is unreliable at close range. "Close range" is a fairly subjective term, and depends upon many factors such as boat speed. In this context, "close range" is where the smallest changes in scatterer position contribute the largest changes to its perceived radial velocity, and where small changes in position may correspond to the greatest changes in aspect angle. At distances of less than 40 m, we see a significant degradation of this VEM.

In practice, a changing aspect angle may change the echo received from any given scatterer by altering its scattering properties. Intuitively, the echoes received from a target such as a rock depend strongly upon the rock's orientation relative to the transducer array. As the target rotates, new scatterers may be introduced while old scatterers move into "shadows", and common scatterers may now be ensonified from a new angle which may cause their scattering properties to change. This behavior is modeled in the simulator.

The RMSE for the entire profile is equal to 3.7 m/s, but if we break up the profile into two segments then we see a clearer picture of the performance of this estimator. Let the first such segment include the first ten velocity estimates (where the scatterers' radial velocity varies strongly with range), with the second segment including the rest of the profile where radial velocity is more constant with range. We calculate that the RMSE of the first segment is equal to 5.5 m/s, and the RMSE of the second segment equal to 0.09 m/s - a large difference.

The incoherent VEM has been shown - via simulation - to be fairly binary in its operation: it appears to either work well, or to work hardly at all.

### 3.2.2 Single Ping Covariance

We now consider both the monopulse and pulse pair single ping covariance VEMs. Theoretically, these methods have been shown to be equivalent under some conditions: namely that  $SNR_e$  and  $k$  must be equal between both techniques. This is achieved by using the test pulse pair, with  $k_p = 30$  and  $k_s = 35$ , and comparing it against a monopulse with  $k_p = 130$  and  $k = 65$ . As such,  $SNR_c = 0$  dB and  $k = 65$  for both cases. Under these conditions, and when  $SNR_n = 40$  dB, we know that the  $\sqrt{CRLB_{10}(v)} \approx 0.71$  m/s for both VEMs. Furthermore, from our previous theoretical analysis, we expect that when using  $N = 10$  snapshots for estimation that we may compare the RMSE of our estimators to the  $\sqrt{CRLB_{10}(v)}$ , and expect the RMSE to be greater than the  $\sqrt{CRLB_{10}(v)}$  by a factor of

$\approx 1.24$ , for an RMSE of  $\approx 0.88$  m/s.

To further our analysis, a slight change to the simulation program is made when indicated. The primary simulator (which was used to analyze the incoherent method, and is used for part of the analysis of the covariance methods) creates a single vector of random Gaussian scatterers at random locations, and retains these same scatterers between pings as their position relative to the boat changes due to boat velocity. A VEM which relies upon ping pairs to produce velocity estimates requires such a simulator, but VEMs that require only a single ping to produce velocity estimates do not place this requirement upon the simulator. Therefore, to enable multiple independent snapshots to be taken from a common range across separate pings, we use a "secondary simulator" which generates entirely new scatterers with each ping.

### Monopulse

Figure 3.11 shows the behavior of the single ping covariance estimator when used in conjunction with a monopulse. We see that the velocity estimates which are produced by this method are much worse than the incoherent method's estimates. When averaging across multiple ranges inside each ping we see weak agreement with theory because we calculate that  $RMSE \approx 0.97$  m/s, or off from the  $\sqrt{CRLB_{10}(v)}$  by a factor of  $\approx 1.36$ . The differences between the theoretically predicted factor of  $\approx 1.24$  and the simulated factor  $\approx 1.36$  which related the achieved RMSE to the  $\sqrt{CRLB_{10}(v)}$  require further examination.

By switching to the secondary simulator, and drawing the  $N = 10$  independent snapshots from across different pings but at a common range (instead of drawing snapshots from the same ping but at different ranges, as we have previously done) we verify that this VEM does attain the predicted RMSE to  $\sqrt{CRLB_{10}(v)}$  ratio of  $\approx 1.24$ . Previously, we have taken the ten snapshots from different ranges, and at close range we expect that this causes velocity estimates to be sub-optimal because each range corresponds to a unique velocity. By averaging across pings we alleviate this problem, and expect that if we conduct a large enough number of experiments that the average RMSE of any sub-segment of the profile would not differ from the entire-profile average.

After transmitting ten pings, we see that our expectations are proven correct. Although a much larger number of pings, say 10,000, would need to be simulated in order to obtain RMSE calculations which do not fluctuate as much when different portions of the profile are included, such a study would require great computing resources (or great patience with

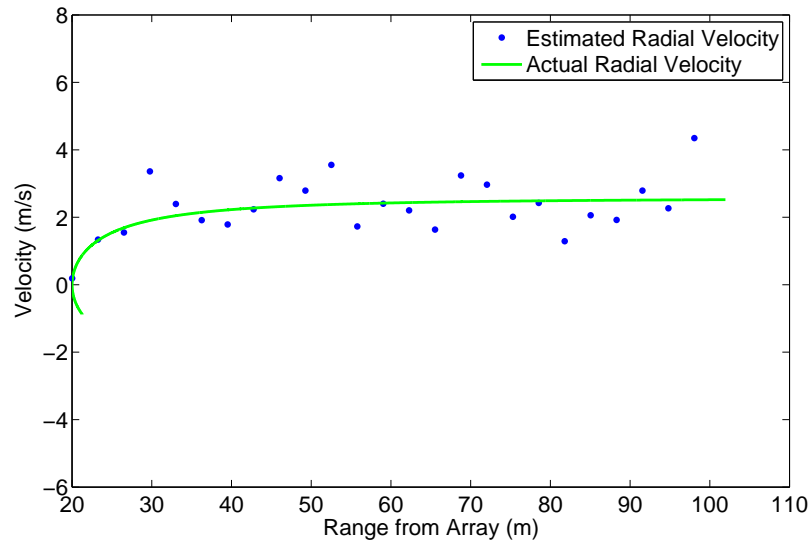


Figure 3.11: The monopulse single ping covariance VEM under high  $SNR_n$  conditions. Boat speed was held at 5 knots ( $\approx 2.57$  m/s), and an  $SNR_n$  of 40 dB (at long range) was simulated with the "primary simulator". The pulse was 130 cycles long, and estimation was performed at lag  $k = 65$ .

the existing computer resources) which are not currently available. Therefore, we conduct our analysis with a lesser number of pings but seek simply to establish the presence of the behavior which we have anticipated. It is assumed that the reader is familiar with the manner in which data are presented graphically, and for this reason we omit additional plots and focus instead on results.

At close range, using the portion of the velocity profile from 20 m to 35 m, we calculate the RMSE to  $\sqrt{CRLB_{10}(v)}$  ratio to be  $\approx 1.07$ , below the expected value of  $\approx 1.24$  although this is a small sample size which is lacking in any "wild" outliers. The rest of the profile yields an RMSE to  $\sqrt{CRLB_{10}(v)}$  ratio of  $\approx 1.31$ , which is slightly higher than expected. If the entire profile is used to determine the RMSE to  $\sqrt{CRLB_{10}(v)}$  ratio, then we calculate a ratio of approximately 1.28 - very close to what we expect. By averaging across pings, rather than averaging inside a given ping but across different ranges, we now see that it is possible to obtain estimate error which is in approximate agreement with the predicted error levels.

### Pulse Pair

Figure 3.12 shows the performance of the pulse pair single ping covariance VEM when no matched filtering is performed. All conditions are identical to those which were specified when evaluating the single ping covariance method with the monopulse, so the CRLB on velocity estimates is equal for both cases. Similarly, we expect the same ratio of RMSE to  $\sqrt{CRLB_{10}(v)}$  of  $\approx 1.24$ . However, the RMSE of this VEM is higher than the corresponding monopulse VEM:  $RMSE \approx 1.03$  m/s, and a subsequent ratio between the RMSE and  $\sqrt{CRLB_{10}(v)}$  of  $\approx 1.44$ . This ratio, much like the monopulse when snapshots are taken from different ranges rather than different pings, is much higher than theory predicts. We note once more that we have not conducted many trials (35 data points, each composed of 10 independent snapshots over 10 pings), and have not yet explored the behavior of the estimator if the averaging is done across pings rather than across different ranges.

Switching now to the secondary simulator, where averaging is performed across pings for a given range, the ratio between the RMSE and  $\sqrt{CRLB_{10}(v)}$  drops to approximately 1.27 for the entire range - very close to the theoretically predicted value. Here we may conduct many more trials (approximately an order of magnitude more) as the averaging across pings frees us from the requirement that each velocity estimate be taken from a time series location which is  $N_{snap} * k_p$  away from the previous estimate's location. We conclude

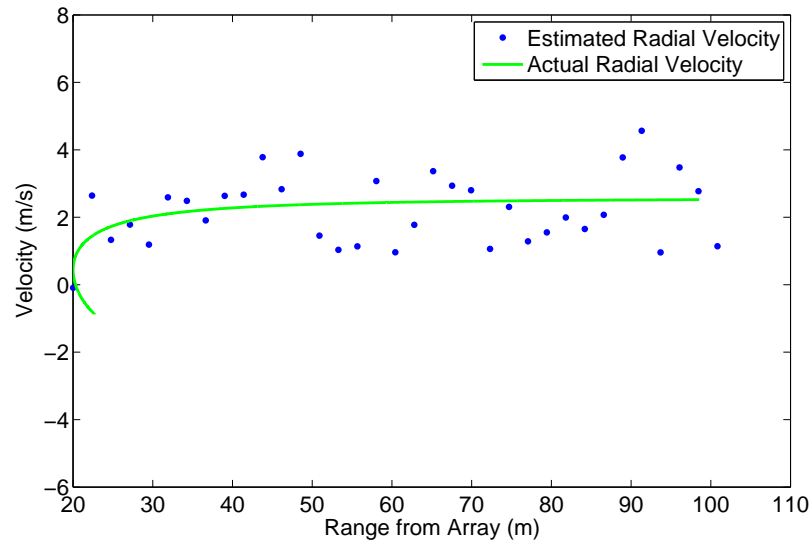


Figure 3.12: The pulse pair single ping covariance VEM under high  $SNR_n$  conditions. Boat speed was held at 5 knots ( $\approx 2.57$  m/s), and an  $SNR_n$  of 40 dB (at long range) was simulated. Each pulse in the pair was  $k_p = 30$  cycles long, and the pair was separated by  $k_s = 35$  cycles of dead time. Estimation was performed at lag  $k = 65$ .

that we have demonstrated the advantage to averaging across pings, rather than across ranges, if one wishes to obtain the estimated "optimal" RMSE to  $\sqrt{CRLB_{10}(v)}$  ratio. Such a procedure will lower the data rate of a system (now, we require more than a single ping in order to produce a velocity profile) and may raise a number of practical considerations, such as decorrelation arising from boat motion between pings, but is necessary if one desires to obtain the optimal RMSE to  $\sqrt{CRLB_{10}(v)}$  ratio.

### 3.2.3 Ping Pair Covariance

We now consider the monopulse ping pair covariance approach to velocity estimation. Theory has shown us that this method is not able to tolerate macro boat velocities when the time between pings is on the order of a tenth of a second, but we seek to test its performance nonetheless. In simulation, we are considering a seafloor which is only 100 m in extent, and is located 20 m below the boat. This results in a time between pings of  $T_p \approx 0.136$ , or just over half of the previous value that we assumed for  $T_p$  in our theoretical calculations. This shorter time between pings raises the maximum unambiguous velocity to  $v_{max} \approx 1/109 = 0.0092$  m/s, or 0.0178 knots. The associated bound is  $\sqrt{CRLB_{10}(v)} \approx 5.92 * 10^{-5}$  m/s, or just under twice the value that was assumed during our theoretical analysis, also arising from the change in  $T_p$ .  $SNR_c$  remains approximately the same as it was for our theoretical analysis, and by repeating the procedure that was outlined in Section 2.5.4, we calculate that the RMSE of this estimator should be approximately 1.06 times greater than the  $\sqrt{CRLB_{10}(v)}$  in this case.

Figure 3.13 shows a plot of the velocity estimates produced via the monopulse ping pair covariance approach for a 0.006-knot boat. We see what appears to be a very strong agreement with the theoretically "correct" or actual velocities which are being estimated. However, when calculating the RMSE, we note that it is surprisingly high. Here,  $RMSE \approx 3.7 * 10^{-4}$  m/s, or approximately 6.3 times the  $\sqrt{CRLB_{10}(v)}$  for this case. While the absolute error in the velocity estimates is very small, this represents a far greater error than expected. Simply by examining Figure 3.13 it is difficult to understand this behavior, but by examining the error of each point along the plot, it is noted that the error of each velocity estimate decreases with range. The ping pair covariance method, relying upon the ensonification of the same scatterers between pings, therefore cannot be used with the secondary simulator.

However, having seen similar behavior in both the monopulse and pulse pair single ping

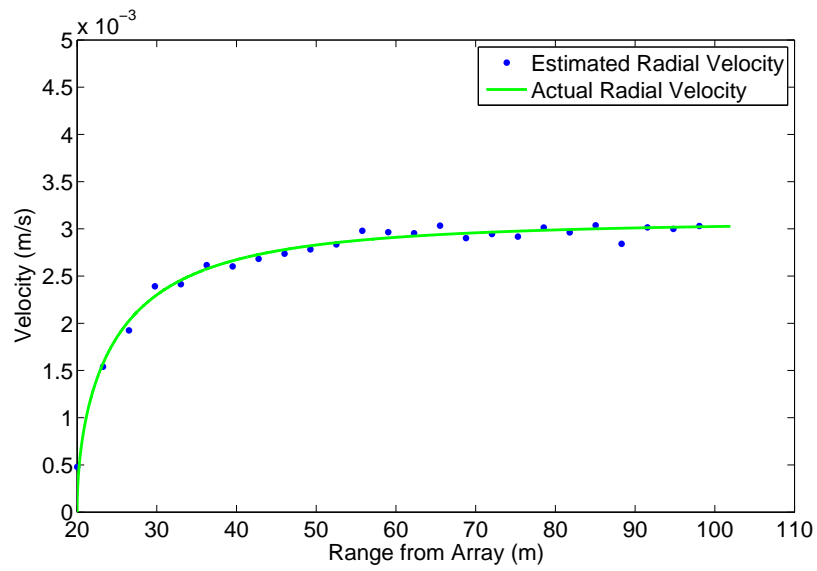


Figure 3.13: The monopulse ping pair covariance VEM under high  $SNR_n$  conditions. Boat speed was held at 0.00309 m/s (0.006 knots), and an  $SNR_n$  of 40 dB (at long range) was simulated. The pulse was again 130 cycles long.

covariance estimators, we can conclude that the cause of this behavior is probably the same. When the  $N$  snapshots are taken from different ranges which have different radial velocities towards the transducer array, the average of these snapshots is not a good velocity estimate at close range. At longer range, when the radial velocity is changing less quickly as a function of range, averaging the individual phase estimates is less damaging to the resulting velocity estimate. The ratio between the RMSE and  $\sqrt{CRLB_{10}(v)}$  is approximately equal to 9.8 at ranges less than 40 m, but this ratio becomes 1.01 at ranges greater than 40 m.

While the latter ratio is better than we predicted it could be, it has been established with only a couple hundred trials (24 data points, repeated for 9 pings), and is prone to fluctuation due to this relatively low number of trials. It is not the aim of this thesis to conduct an exhaustive investigation into this matter, but to instead conduct a foundational investigation. It has been established that the covariance estimators suffer if multiple snapshots, taken from different ranges rather than different pings, are combined into one velocity estimate when radial velocity changes quickly as a function of range.

### 3.2.4 Simulation and the VEM's: Concluding Remarks

We have now finished evaluating the velocity estimation methods in a simulated environment. The monopulse incoherent method was seen to produce the tightest velocity profile (at long range) for macro velocities, but was also seen to produce the worst velocity profiles at close range when the radial velocity was changing most quickly. The single ping covariance methods have been shown to be equivalent under the conditions chosen, where  $SNR_e = 0$  and  $k = 65$  for both cases. Like the single ping covariance methods, which yielded (approximately) the predicted RMSE to  $\sqrt{CRLB_{10}(v)}$  ratios, we have seen the ping pair covariance method yield RMSE values which also behave as predicted.

An important discovery has also been made: that when using multiple snapshots to estimate the velocity of a range-spread target which for one reason or another appears to be a "velocity-spread" target, the usage of multiple snapshots taken from different ranges may adversely affect estimator performance. When combining multiple independent snapshots such estimator RMSEs approach the  $\sqrt{CRLB_N(v)}$  if these snapshots come from portions of the seafloor which are not significantly different in radial velocity from one-another. Otherwise, by attempting to compromise range resolution for the sake of increased velocity resolution (by increasing  $N$ ) it is possible to end up inadvertently increasing the error in subsequent velocity estimates.

The conclusion which we now draw is that caution must be exercised when deciding upon the number of snapshots to use in pre-estimation averaging. In the case of taking snapshots from across pings, more snapshots improve estimate RMSE but reduce data rate. In the case of taking snapshots from inside each ping, too few snapshots result in insufficient averaging such that the CRLB is difficult to attain. By using too many snapshots, excessive averaging is performed, and the velocity estimate RMSE does not approach as closely to the  $\sqrt{CRLB_N(v)}$  as it would if target velocities were more constant over the  $N$  snapshots.

In experimentation, where the seafloor is not as flat and uniform as we have modeled it to be in simulation, and where factors such as water current or wind make it difficult to maintain a constant velocity, we expect these effects to be exaggerated. Many such considerations are likely to affect the velocity estimates which are obtained in practice, and it is considered unlikely that RMSE to  $\sqrt{CRLB_N(v)}$  ratios are as low in practice as they are in simulation.

We now conclude the simulation portion of this thesis. So far, we have developed the relevant foundational mathematics behind the analysis of our chosen velocity estimation methods, we have discussed their theoretical performance limitations in detail, and we have validated these findings via simulation. After concluding that certain aspects (such as the spread of target velocities, and any factors influencing the "decorrelation noise" term  $\tilde{N}$ ) may render our theoretical performance limitations to be unattainable in practice, we turn our attention to experimentation.

## Chapter 4

# Experimental Data

We have now finished characterizing the performance of the VEMs in relation to a simulated seafloor, and we move on to analyzing their performance with "real" data taken experimentally. In simulation, we discovered a practical consideration which may adversely affect the velocity estimates of a range-spread target: averaging multiple snapshots from within a given ping. As we proceed through our experimental analysis, we anticipate that additional practical considerations which affect our velocity estimates may also evidence themselves.

The data which are to be processed were taken using only a monopulse transmit waveform. However, since the single ping covariance approach has been shown through theory and simulation to be equivalent between a pulse pair and a monopulse (when  $SNR_e$ 's and  $k$ -values are equal) the results for the monopulse are taken as indicative of the estimator performance if a pulse pair had been transmitted. We consider only the monopulse incoherent, and monopulse single ping covariance methods.

### 4.1 Defining the Experiment

We now depart from the simulated world and enter the "real" world as we seek to test these velocity estimation methods. In the "real" world the seafloor is not perfect flat, there are frequently surface conditions (such as waves, wind, wake from other boat traffic, or unwanted boat pitch/roll) which disturb the experiment during data collection, and the water column is certainly not as free of suspended scatterers as it was in simulation. All of these experimental concerns need to be remembered when evaluating the VEMs against experimental data, because they introduce many elements which were not present during

simulation and theory which may affect the signal. Although through theory and simulation we have captured the essence of the problem at hand, these additional experimental considerations will likely have an impact on the velocity estimates. Intuitively, it is expected that each estimator will perform slightly worse with experimental data than it did in simulation.

Experimental data were taken in November of 2009 at the Indian Arm inlet during a survey of the salt water fjord. During the experiments which are under consideration presently, the tilt angle on the transducer was approximately 38 degrees below horizontal. The transducer had a carrier frequency of 182 kHz - far lower than the 300 kHz which has been examined thus far, but this change in frequency does not affect the suitability of the signal processing methods discussed herein. A pulse length of 160 cycles was maintained, and it was sampled at a frequency of  $f_s \approx 86$  kHz. At this sampling frequency  $f_s$ , the resulting triangle in the autocovariance function has a width of approximately  $2 * 76$  lags, and therefore our optimal lag is  $k_0 \approx 29$ , and the maximum unambiguous velocity equal to  $\approx 6.1$  m/s (or roughly 12 knots). This is because the lower sampling rate, equal to  $86/182 \approx 0.47$  times the carrier frequency, shortens (by this same factor) the width of the autocorrelation peak. So that we can equate the resulting velocity profile to that which would have been obtained if a pulse pair had been transmitted where  $k_p + k_s = 38$ , we perform estimations at lag  $k = 38$ , or half the pulse width. At this lag, we expect a maximum unambiguous velocity of  $\approx 4.7$  m/s (roughly equal to 9 knots). As a result of the lower frequency and long pulse, the surveying range is extended out to approximately 200 m.

We now process data taken during data file 017 on Nov 12, 2009. The data file contains hundreds of separate pings, and in this analysis we use only pings 15 and 16 to test the VEMs. The transducer was facing forward, while the ship was traveling at a known forward speed of approximately 4 knots (earth-referenced) as estimated by GPS. This particular data file was taken in Bedwell Bay (located inside the Indian Arm fjord), which has a fairly flat seafloor.

## 4.2 Results

Because we observed surprisingly accurate results from the incoherent method in simulation, we begin our analysis there. We have previously found the incoherent method to be almost binary in its operation: it either fails completely, or appears to work surprisingly well. It

was found to have a weakness when range bins may encompass a portion of the seafloor which is spread in radial velocity, such as directly underneath the boat. Once this method has been considered, we turn our attention to single ping covariance processing. Ping pair covariance processing is not considered.

### 4.2.1 Incoherent Processing

Figure 4.1 shows the performance of the incoherent estimator as it attempts to estimate boat velocity in Indian Arm between pings 15 and 16, where the averaging interval was 1500 samples wide. We use different colors which denote the degree of correlation between the two pings. The bright copper dots indicate a low degree of correlation, and the dark copper dots indicate a high degree of correlation between pings. The darker colors correspond to correlation peaks of (normalized) height approximately 0.7 to 0.85, while the lighter colors correspond to peaks with a height which is closer to 0.4 or 0.5. Data are plotted for ranges where seafloor returns will be present in the received signal (beyond approximately 40 m).

Let us examine the individual estimates in the profile. We see that the least degree of correlation occurs at close range (between approximately 50 m and 80 m). In this region, the pulse has only begun to hit the bottom, and is traveling along the region where the smallest change in position corresponds to the largest change in radial velocity. Such behavior (poor estimates inside this region) is anticipated, as discussed in the preceding Simulation Chapter.

Strong correlation is seen from ranges of approximately 80 m to 200 m. This behavior is also anticipated, as the radial velocity at greater distances (assuming a flat seafloor) varies more slowly than it does at lesser distances. Although the "true" radial velocity in this region does not change rapidly with varying range, it does increase slightly as range increases. This behavior is also seen in Figure 4.1. RMSE in this region is equal to  $\approx 0.07$  m/s, while from 40 m onwards the RMSE is much higher:  $\approx 0.93$  m/s.

### 4.2.2 Single Ping Covariance Processing

Figure 4.2 shows the velocity profile which was produced via the single ping covariance method over ping 15 alone. With approximately  $T_p = 0.267$  s as the time between pings, we expect that the boat's "true" earth-referenced velocity was essentially unchanged until the end of ping 16. By making this assumption, we may compare the velocity profile which is generated by this method with the profile that was generated by the incoherent method.

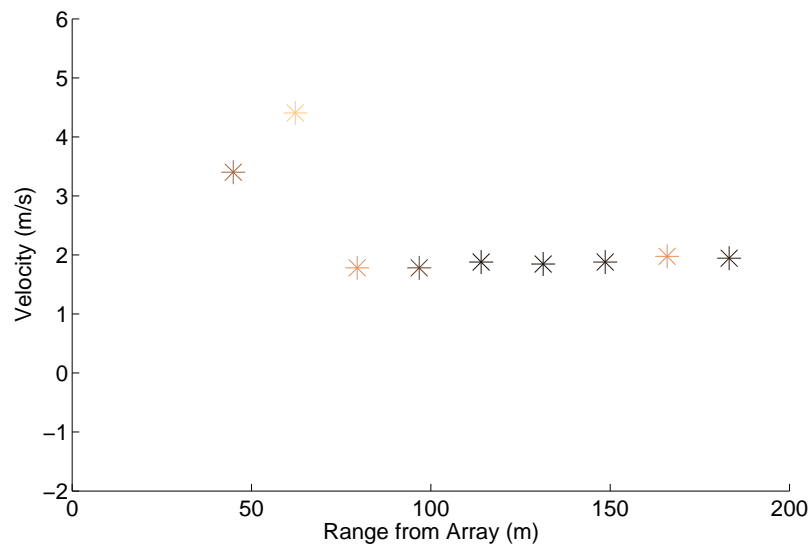


Figure 4.1: Incoherent velocity estimates corresponding to a boat with an earth-referenced velocity of 4 knots (2 m/s) plotted in color to denote the degree of correlation at each range. These data were taken in the Indian Arm fjord, and range bins of 1500 samples were used to incoherently process pings 15 and 16. Here, a dark copper color indicates a high degree of correlation, whereas lighter colors indicate lesser degrees of correlation.

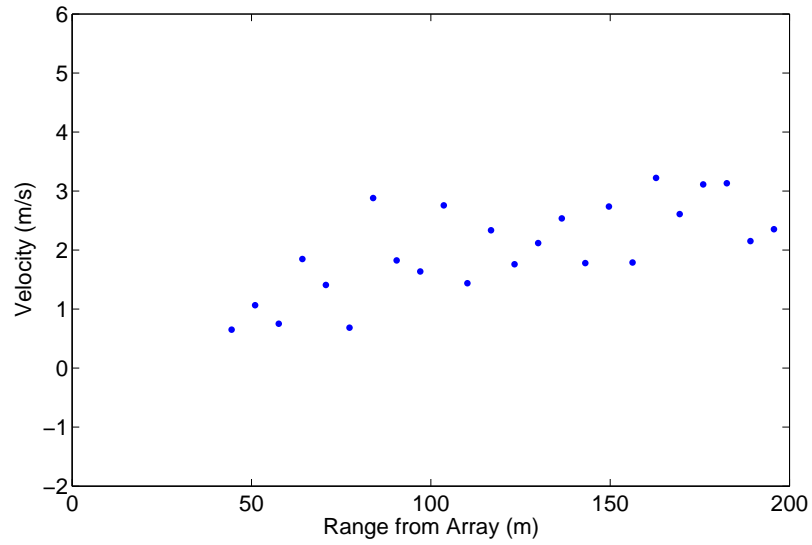


Figure 4.2: Single ping covariance velocity estimates taken in Indian Arm, with the boat moving at 4 knots (approximately 2 m/s) relative to the seafloor.  $N = 10$  snapshots were used, and  $k = 38$  for this pulse.

Again, we see our velocity estimates agree roughly with what we are taking to be the "true" earth-referenced velocity of the boat (the recorded GPS velocity) and are plotted for ranges which include seafloor returns. The covariance method is shown to produce consistently noisy velocity estimates which center around (approximately) the GPS-estimated earth-referenced velocity of 4 knots (2 m/s). If we disregard the first 40 m of the profile, the remaining profile has an RMSE of  $\approx 0.77$  m/s.

It is concluded that the single ping covariance method is also providing results that are in approximate agreement with the expected result, as well as being in agreement with the trend that was produced via the incoherent method. While the incoherent method is seen to produce a more precise velocity profile at long ranges, the covariance method seems to perform better than the incoherent method at close range, having fewer "wild outlier" estimates. Because we are working at lag  $k = 38$  (corresponding to half of  $k_p = 160 * f_s / f_c \approx 76$ ), we may assume that these results are consistent with those that would be obtained if a pulse pair had been transmitted, where  $k_s + k_p = 160$  and a similar filtering scheme were used.

### 4.2.3 Validation

We now attempt to validate - to the best of our ability - the velocity estimates which have been yielded by the two estimators. Firstly, we seek to show agreement between the two VEMs by plotting them together on the same Figure. We observe the trend shown in Figure 4.3, and can see that the covariance and incoherent VEMs appear to be in agreement that the boat's earth-referenced velocity was in the vicinity of 2 m/s, although there is some disagreement between the methods.

We also estimate  $SNR_n$ , and compare the RMSE of the covariance method to the  $\sqrt{CRLB_{10}(v)}$  for this method. The combined signal and noise have a level of approximately 74 dB at close range (when the pulse is just beginning to strike the bottom) and a level of  $\approx 30$  dB at long range. Immediately after transmission of the ping sequence, used above, followed another ping sequence where no signal was transmitted (only the receive transducers were active). From this data file, the noise level is estimated at  $\approx 16$  dB, indicating that at close range  $SNR_n \approx 58$  dB while at long range  $SNR_n \approx 14$  dB. At these  $SNR_n$ s, the  $\sqrt{CRLB_{10}(v)}$  for the covariance method is  $\approx 0.71$  m/s and  $\approx 0.75$  m/s, respectively. The covariance velocity profile is seen to have an RMSE ( $\approx 0.77$  m/s, disregarding the first 40 m of the profile) which is approximately equal to the theoretical limit for this estimator at

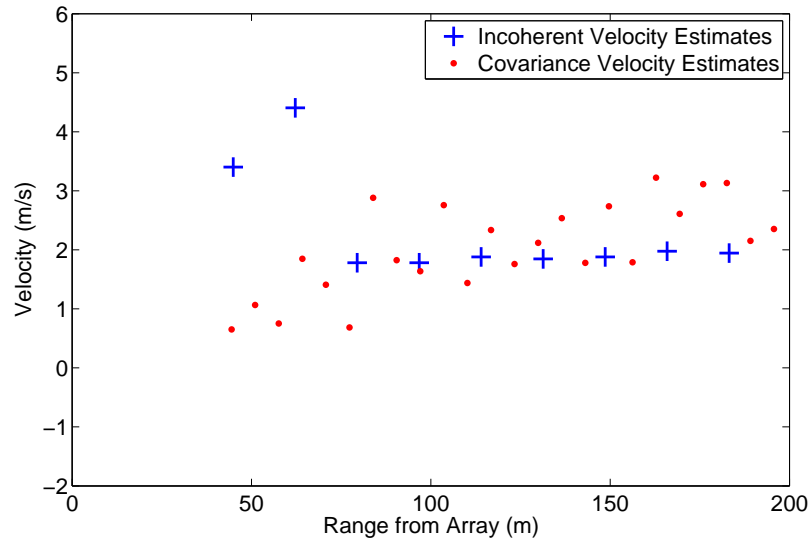


Figure 4.3: Covariance (red dots) and incoherent (blue dots) velocity estimates taken in Indian Arm, with the boat moving an estimated 4 knots ( $\approx 2$  m/s) relative to the seafloor. Results from the previous two Figures have been superimposed to allow for easy comparison between the VEMs.

these  $SNR_n$ s.

### Side-Scan Image

One more method may be employed to verify the boat's earth-referenced velocity. By taking part of this ping set (say, 500 pings) and producing an image similar to a typical "side scan" image, except that the transducer was pointed forwards instead of athwart the boat, it is possible to estimate the earth-referenced velocity. Assuming that the narrow beam of the sonar system strikes the same scatterers with each successive ping, we see these scatterers approach the boat as time passes. When patterns in a given ping of the "side scan" image reappear in subsequent pings, they are at a lesser range for a forward-moving boat. It is therefore possible to estimate the velocity of a boat when the boat-mounted transducer is pointed parallel to the direction of motion, and if the transducer's beam is continually ensonifying the same scatterers.

The side-scan image shown here in Figure 4.4 plots the intensity of the received signal versus range (x-axis) for each ping number (y-axis). The first ping is represented by a series of pixels across the bottom line of the image (with subsequent pings occurring incrementally higher along the y-axis), where substantial echoes are only received after approximately 50 m. For any given ping, the lighter colors correspond to stronger (more intense) echoes while the darker colors correspond to weaker echoes. From this Figure, we can clearly see that as the ping number increases (corresponding to an increase in the absolute time at which the ping was taken) certain patterns in the echo intensity appear at closer ranges. The seafloor is assumed to be located at a depth of approximately 50 m, corresponding to the range at which the first substantial echoes are received. As patterns in the seafloor approach this depth, they depart from the more linear behavior at longer ranges and appear to begin to describe some sort of curve.

This curve-like behavior at closer ranges is simple to explain. A scatterer which begins at a great horizontal distance and at some depth from the boat, and progresses towards it at a constant horizontal - but not radial - velocity, its motion is only changing in one of two dimensions; its depth remains constant. Hence, the seafloor scatterer can only approach to a range equal to the depth of the seafloor - and can go no closer. When a scatterer's range is approximately equal to its depth, we know that its perceived radial velocity tends towards zero. We therefore expect to see this trend manifest itself in such forward-looking images as Figure 4.4.

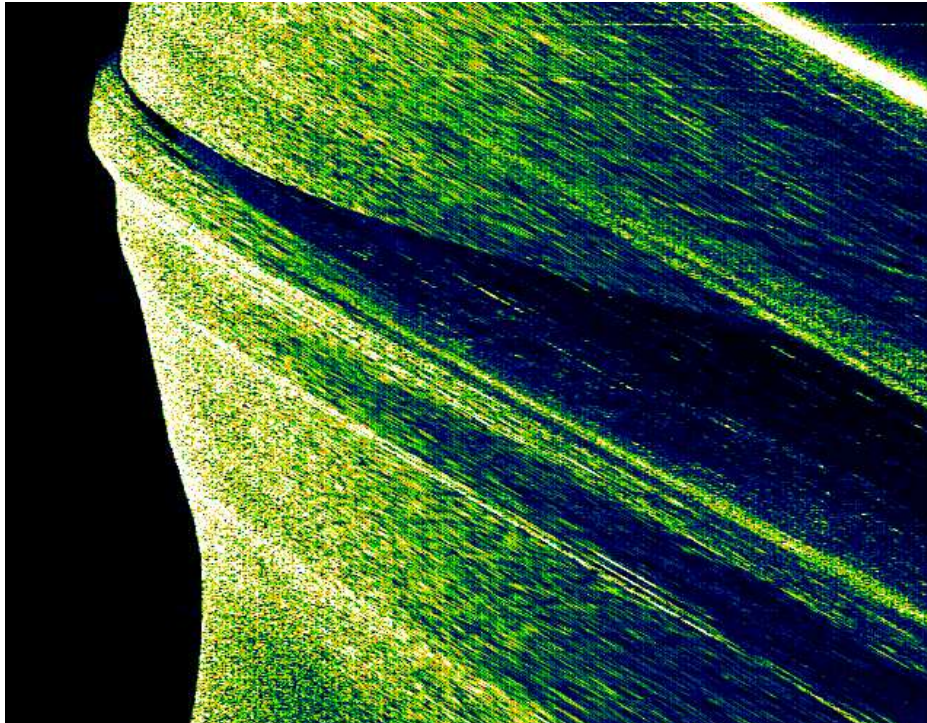


Figure 4.4: "Side-scan" image taken from pings 1 to 500 of the November 12th, 2009 data. Intensity is plotted for each ping number as a function of range, with dark colors representing low-intensity echoes and lighter colors representing more-intense echoes. The y-axis represents ping number, increasing from ping 1 to ping 500 from the lower left corner of the plot. The x-axis represents range, where range increases from 0 m towards 200 m, moving from left to right across the Figure.

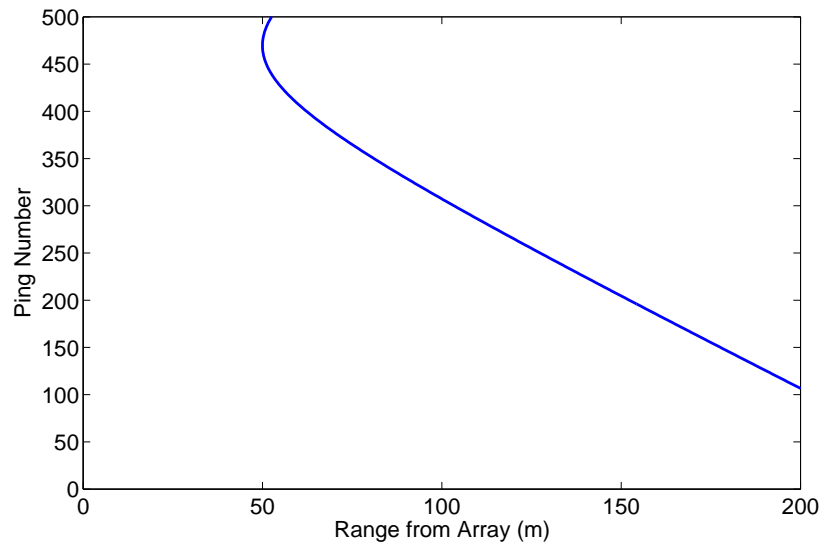


Figure 4.5: Simulated reproduction of behavior shown in Figure 4.4, where trends in the ensonified seafloor are seen to approach the transducer array in subsequent pings. The resulting trend appears linear at long distance, but then gives way to a noticeable curve as the range approaches the depth of the seafloor.

We confirm this behavior with a quick calculation. Figure 4.5 shows a plot of a scatterer's range changing with ping number. In this simple simulation, the scatterer began at a range of 250 m and depth of 50 m at ping 1. The scatterer moved towards the boat at a horizontal speed of 2 m/s, and each ping was assumed to last  $T_p = 0.2667$  seconds. After 500 pings, we can confirm through simulation that the behavior seen in Figure 4.4 is indeed what we expect it to be.

We now seek to determine the speed of the seafloor from Figure 4.4 by estimating the slope of any given "line" created by a set of scatterers as they move towards the boat. The velocity calculation is simple: by knowing the initial and final positions of the scatterers at two separate pings, and by knowing the absolute time difference between these pings (recorded by the sonar system) we divide distance by time to estimate the boat's velocity.

Let us consider two separate "lines" in the data, and average the results of each velocity estimate. The first such line begins on ping 1 at a distance of approximately 185 m and ends on ping 270 at a distance of approximately 45 m. The elapsed time between these pings is approximately 72 s, making the estimated velocity equal to 1.95 m/s. Tracing our second line, we begin at a distance of 194 m on ping 83 and end on ping 322 at a distance of approximately 58 m. The elapsed time in this case is equal to approximately 64 s, and results in a velocity estimate of approximately 2.1 m/s. These velocity estimates yield a mean velocity estimate of approximately 2.03 m/s, and are highly consistent with those produced via both the covariance and incoherent VEM, as well being in close proximity to the value recorded by the vessel herself (2.06 m/s, or 4 knots) for earth-referenced velocity.

We conclude this Chapter by noting that the incoherent and single ping covariance VEMs have been demonstrated to produce reliable velocity estimates in an experimental setting. Their respective velocity profiles bear a close resemblance with those which were demonstrated in simulation, and we have anticipated the locations of their most erroneous estimates (close range) and their "best" estimates (long range). We have seen that the velocity estimates produced by either estimation method (incoherent or covariance) are clustered into clear trends, although close-range estimates lack precision as predicted.

RMSE values for the coherent estimator are close to the calculated theoretical performance limits, although the calculated RMSE value for the experimental profile is simply a measure of the profile's precision, and does not address its accuracy. Whereas in simulation, RMSE values were calculated based on estimate deviation from the "true" value (which changes as a function of range), when working with experimental data RMSE is calculated

directly from the data - no "true" values are considered. Since we no longer know the geometry of the seafloor, we cannot be certain about the radial velocity of any portion of the seafloor. Under more controlled experimental settings, such as in a large test tank where the seafloor shape and transducer position could be much more controlled, such a calculation (where the "true" value is subtracted from the estimated value for radial velocity) would be possible.

Our attention is now turned to one final area before concluding the thesis: the micro-Doppler technique.

## Chapter 5

# Micro-Doppler

This final analysis arises as a result of the research which has been described in this thesis, and is presented as an observation and as a suggestion for future work. Although the concept of micro-Doppler has been discussed in radar literature [1, 31, 2] for uses such as target identification, it has yet to be explored in the context which is considered presently. An important problem in many sonar applications is target detection by a nearly-stationary monostatic array, for instance if one wishes to detect the presence of underwater divers approaching a naval base. The micro-Doppler method, when applied as described thusly, provides a solution to this problem.

### 5.1 Theory

The mathematical theory behind this approach has already been presented, and provides a convenient foundation for the present discussion after a brief introduction has first been presented. We are considering the physical setup where the transmitter and receiver are co-located (a monostatic array), are constrained to remain in approximately that same location, and are pointed in the same direction for each ping. Furthermore, we assume that a target enters the view of the transducer at some point in its operation.

In practice, it can be difficult keep the transducer completely stationary between pings: even a transducer that is attached to a concrete pylon may move slightly in the presence of strong currents or surface turbulence which shakes the pylon. It is therefore desirable to develop a system that can tolerate and account for small-scale motions between pings, while still remaining effective at detecting the presence of any incoming targets. While the

ping pair covariance method has been shown to experience phase wrapping at low target speeds, ping pair processing can be employed to compensate for ping-to-ping motion of an almost-stationary transducer array, allowing for the presence of incoming targets to be immediately evidenced.

Recall that with the ping pair covariance method, a comparison across pings is made (see Equation 2.38). We model the signal which is received from the first ping as

$$\tilde{s}_1(t) = \sqrt{E_t} \int_{\Omega} \tilde{f}(t - \lambda) \tilde{b}_R(\lambda) e^{j(w_D t - w_c \lambda)} d\lambda + \tilde{n}_1(t) \quad (5.1)$$

while the signal received from the second ping is

$$\tilde{s}_2(t) = \sqrt{E_t} \int_{\Omega} \tilde{f}(t - \lambda_1) \tilde{B}_R(\lambda_1) e^{j(w_D t - w_c \lambda_1)} d\lambda_1 + \tilde{n}_2(t) \quad (5.2)$$

where we are integrating over the range ( $\lambda$ , in units of seconds) of the sonar system. The complex Gaussian process  $\tilde{b}$  describes the reflection of the signal off of a given portion of the seafloor, which is divided up into sections of  $\lambda$ , corresponding to the location (in units of time) of the section. The use of a lowercase  $\tilde{b}_R(\lambda)$  and uppercase  $\tilde{B}_R(\lambda)$  signify that the scattering parameters of one section of seafloor are not necessarily the same across multiple pings. Recall that  $E_t$  is the transmitted energy,  $\Omega$  signifies the time ranges over which we integrate,  $\tilde{f}$  is the envelope function, and  $\tilde{n}(t)$  is the additive noise term.

In our previous analysis, we assumed that the scattering parameters of these seafloor scatterers will not change between pings and are constant throughout all ranges, and thus  $\tilde{b} = \tilde{B}$  and is no longer a function of  $\lambda$ , such that the expectation  $E[\tilde{b}_R \tilde{b}_R^*] = 2\sigma_b^2$ . Under these assumptions, we then defined the range-scattering function as  $S_R(\lambda) \equiv E[\tilde{b}_R(\lambda) \tilde{b}_R^*(\lambda)] = S_R$  (since we assume  $S_R$  is not a function of range) and later inserted it into our expression for the covariance. The cross covariance of the signals  $\tilde{s}_1(t)$  and  $\tilde{s}_2(t)$  is expressed as

$$K_{\tilde{s}_1 \tilde{s}_2}(t, u) = E \left[ E_t \int_{\Omega_L} d\lambda \tilde{f}(t - \lambda) \tilde{b}_R(\lambda) e^{j(w_D t - w_c \lambda)} \cdot \int_{\Omega_L} d\lambda_1 \tilde{f}^*(u - \lambda_1) \tilde{B}_R^*(\lambda_1) e^{-j(w_D u - w_c \lambda_1)} \right], \quad (5.3)$$

and assuming that no new target enters the view of the transducer array between pings the resulting covariance function is simplified to

$$K_{\tilde{s}_1 \tilde{s}_2}(kT_k) = E_t S_R \rho_{c,c}(kT_k) e^{jw_D(kT_k - T_p)} \quad (5.4)$$

as previously determined in Chapter II (Equation 2.87). Recall that  $\rho_{c,c}(kT_k)$  represents the value of the *tri* function at the lag  $kT_k$  ( $k$  being an integer, and  $T_k$  being the sampling frequency), and  $T_p$  is the time between pings.

The small scale motion of the transducer between pings will manifest itself in the exponential term  $e^{jw_D(kT_k - T_p)}$  of Equation 5.4, however the introduction of entirely new scatterers will manifest itself differently. If new scatterers are introduced at a given range, then the scattering function for that range changes as a result. Thus, we cannot simplify Equation 5.3 into Equation 5.4 because the presence of new scatterers at location  $\lambda_x$  implies that  $\tilde{b}_R(\lambda_x) \neq \tilde{B}_R(\lambda_x)$ . The expectation  $E[\tilde{b}_R(\lambda_x)\tilde{B}_R^*(\lambda_x)]$  then evaluates to a complex quantity which results in a new (random) amplitude and phase for the signal that is received from location  $\lambda_x$ .

To develop a clear picture of this behavior, we first consider the case where there is no motion between pings and no new targets enter the view of the transducer. In such a case, for a given range bin the Doppler term evaluates to zero at the center of the covariance function, leaving  $K_{\tilde{s}_1\tilde{s}_2}(0) = E_t S_R$ . Next, we consider the case where no targets enter the field of view, but where some small-scale motion (small enough to not cause phase wrapping) occurs between pings. The result is that the covariance function now evaluates to

$$K_{\tilde{s}_1\tilde{s}_2}(0) = E_t S_R e^{-jw_D T_p}, \quad (5.5)$$

where the phase change between pings is  $e^{-jw_D T_p}$ . Assuming that no phase wrapping occurs, it is possible to track this phase change as a function of range over a number of pings, thus developing a "picture" of the typical motion of the array over time.  $S_R$  will remain unaffected by this micro-motion.

Finally, we consider the case where motion does exist between pings and where a target enters into the field of view at range  $\lambda_x$  in the second of the two pings under comparison. The motion of the sonar system at any given range bin results in gradual phase changes which are tracked across many pings, but does not affect the magnitude of the received signal. However, the introduction of new scatterers at a particular range will alter both the amplitude and phase of the signal received from that range in a significant way. Simply accounting for the motion between pings no longer explains the phase discrepancy between the two pings in the ping pair.

If the target is localized, and does not occupy the entire field of view, then the change in the signal which results from its presence is also localized in the received signal time

series. If this target moves in relation to the transducer, then its motion will cause the location of this "time series anomaly" to change accordingly. To summarize, if we monitor the micro-motions of the transducer array between pings then we are developing a "picture" of these phase changes as a function of range. The introduction of a target into one such range will constitute an anomaly at that range, and we may then track the location at which the anomaly is present. By tracking the location of this anomaly, we indirectly estimate its velocity - even if that velocity is a macro velocity.

## 5.2 Experimentation

Proof of concept is now provided in the form of experimental data, which show that it is possible to achieve the "phase tracking" which has been discussed. Although certainly a useful next step in the analysis of the micro-Doppler method, in the introduction of this method it is unnecessary to demonstrate that the presence of a new target at a given range will change the scattering parameters corresponding to that range. Intuitively, the introduction of new random scatterers at some range will markedly alter the signal returning from that range.

Data were collected on September 25th 2006 in Pavilion Lake, located in the interior of British Columbia. The transducer was fixed to the side of the boat, prior to a side scan survey which would be conducted later, and the boat remained tied to a dock while the data file was collected. The carrier frequency was  $f_c = 280$  kHz, maximum range was set to 210 m, and a 20 cycle pulse was used. Because the transducer was mounted on a small moored boat, rather than fixed to a permanent structure like a concrete pylon, we expect some motion between pings as the crew of the boat moved around and as the boat gently pulled at her mooring lines. The calm lake surface and lack of wind kept this motion to a minimum.

Figure 5.1 shows a representative plot of the phase change between pings as a function of range. Here, we are using 25-sample range bins (which makes them approximately 0.5 m wide, due to the lowered sampling rate of the received signal at one complex sample per eight carrier cycles) and are considering the phase difference between pings 15 and 16. A clear trend is seen, and the gradual slope and consistent nature of this trend indicate that boat motion is responsible for this phase difference. The relatively low rate of phase change between pings throughout the entire range illustrates that the moored boat was

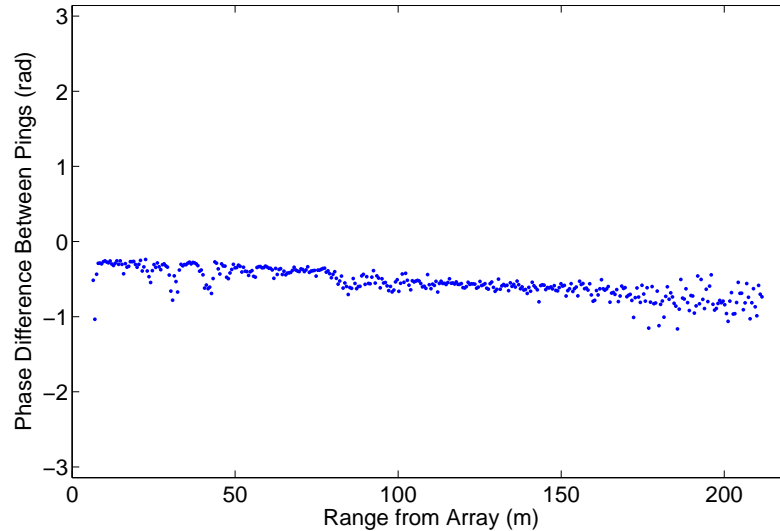


Figure 5.1: Phase difference between pings 15 and 16 as a function of range. Range bins were 25 samples (or approximately 0.5 m) in size.

experiencing little acceleration and maintained a very low velocity at this time (such that no phase wrapping is observed). As range increases  $SNR_n$  lowers, dropping significantly around a range of 200 m, leading to a reduced precision of the phase change estimates. This Figure is used to illustrate that it is possible to track the phase change between pings resulting from transducer motion, and that this change is small and predictable under the correct set of circumstances (in this case, a calm surface leading to minimal boat motion between pings, and a high  $SNR_n$ ).

Figure 5.2 displays the observed phase (red dots) at sample number 832 of transducer element 3 across all fifty pings in the data set. This sample number is chosen because it is representative of the average phase changes seen at other sample numbers where  $SNR_n$  was high. From Figure 5.1 we can see that the phase difference between subsequent pings can - when the sonar platform is nearly stationary - assume a smooth and predictable trend, implying that an incoming target would be detectable as it would result in a significant phase difference between pings which did not follow such a smooth trend. The slow phase variation across multiple pings in the data file (at a given range), shown in Figure 5.2, implies that a target could then also be tracked across multiple pings as the range of the

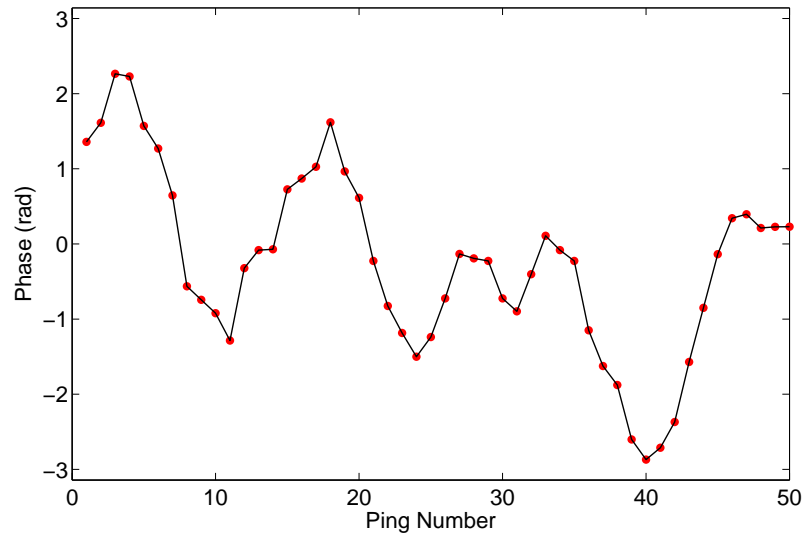


Figure 5.2: Phase observed at sample number 832 on transducer element 3 throughout the entire 50-ping data set. The red dots indicate the observed phase values, and the black line represents the extrapolated phase between observations. This extrapolated value is added to aid the reader in understanding the (assumed) trend in the data.  $SNR_n$  at this sample number is estimated to be approximately 40 dB throughout the data set.

resulting phase anomaly is determined in each ping.

### 5.3 Micro-Doppler: Summary

Target detection and tracking are achievable via the micro-Doppler method in the context of a nearly-stationary monostatic array. It has been shown that, in practice, the motion of a near-stationary transducer may be tracked between pings as the exponential term  $e^{-jw_D T_p}$  in the cross-covariance function varies as a result of this motion. Under calm seas and with minimal wind, a moored boat is seen to provide a suitable platform for such an experiment, indicating that more stable platforms (such as oil rigs) would provide similarly suitable platforms under more turbulent sea/wind conditions. The micro-motion of the transducer inside each ping results in a small phase difference between pings (for each range cell). Were a target to have entered the view of the transducer during a subsequent ping, its presence would introduce a significant phase change at the corresponding range.

## Chapter 6

# Conclusion

In this thesis, a thorough discussion concerning two-point velocity estimation in the context of range spread targets has been provided. The analysis addresses a number of large gaps in the present-day understanding of related velocity estimation methods, and provides a substantial theoretical foundation for future work in many related fields where the velocity estimation of a range-spread target is of interest. Through simulation and theory the theoretical foundation has been verified, and a novel velocity estimation and target detection technique has been discovered.

### 6.1 Contributions of the Thesis

The present analysis picked up where the existing theoretical foundation left off: with the work of Harry Van Trees and the formulation for the received signal and covariance functions for range-spread targets. The existing theory has been extended, such that expressions for the covariance functions of moving range-spread targets were developed. Common velocity estimation methods - the incoherent, and the covariance method - were described mathematically in terms of these covariance functions. Both the monopulse and pulse pair transmit waveforms have been considered.

The Cramer-Rao lower bound was used as an analysis tool with which to examine these velocity estimation methods, and theoretical limitations on their performance were calculated and explored. The existence of an optimal lag  $k_0$ , where estimation of the covariance function results in the lowest bound on velocity estimator root mean-squared error, was discovered and described mathematically. It was proven that the minimization of the CRLB

for velocity estimates is more quickly achieved by lengthening the transmitted pulse, rather than increasing the number of snapshots which are used in estimation. The performance of the coherent velocity estimation techniques was analyzed for varying levels of signal-to-thermal noise, and these results were later verified through simulation and experimentation. The CRLB of the pulse pair covariance estimator has been shown to tighten when matched filtering is employed (when compared to a wide bandpass filter), where the matched filter assumes the shape of one of the pulses in the pulse pair. Simulation was used to estimate the practically-achievable ratio between the velocity estimator RMSE and the  $\sqrt{CRLB_N(v)}$  for varying signal to noise ratios.

Each velocity estimation method was then tested using simulated data. It was found that the incoherent estimator is quite possibly the optimal estimator of macro velocities, although the incoherent estimator was shown to be fairly binary in its operation: it either produces a remarkably accurate profile, or it instead produces a collection of "wild outlier" estimates. Regardless of this flaw, the precision of the incoherent method at estimating macro velocities was shown to be unparalleled at long range, when the radial velocity of scatterers changes little with varying range. The monopulse and pulse pair covariance velocity estimators were shown through theory and simulation to be equivalent, and the ping pair covariance estimator has been shown to be extremely precise, having the lowest Cramer-Rao bound of the coherent estimators which were considered. When assembling multiple snapshots to use in averaging, it was proven that velocity estimates will suffer if they are composed of a number of snapshots taken from areas where the radial velocity is changing rapidly as a function of range. In the context of a hull-mounted sonar system, this implies that velocity estimates at close-range should - assuming minimal pitch/roll or sideways vessel motion - incorporate snapshots from adjacent pings, rather than from adjacent ranges.

Experimental data were used to probe the performance of the incoherent and covariance velocity estimators. The incoherent estimator behaved as expected and was shown to produce accurate and precise velocity estimates at long range, and highly inaccurate and imprecise velocity estimates at close range. The single ping covariance estimator was shown to produce velocity estimates at both long- and close-range which approach the associated  $\sqrt{CRLB_N(v)}$  and nearly attained the predicted RMSE to  $\sqrt{CRLB_N(v)}$  ratio, even though such estimates are markedly more noisy than those formed by the incoherent method at long range. Because the error of the covariance velocity estimates was seen to be in such close proximity to the associated Cramer-Rao bound, and the incoherent method behaved

as expected, it was concluded that single ping covariance velocity estimates are limited to a lower precision than that which is experimentally attainable by the ping pair incoherent method.

A novel approach to two-point velocity estimation in the context of underwater acoustic systems was introduced as a variation on an existing technique: the micro-Doppler method. A foundational discussion of the theory and practical application of this method was provided, and the ability of this method to track phase changes between pings - corresponding to micro velocities - has been demonstrated. By successfully tracking these small phase changes, the introduction of a target - potentially traveling at a macro velocity - results in a significant change in the phase at a given range, which can then be used to detect and/or track the target. It was concluded that the micro-Doppler method provides an innovative and new approach to target detection and velocity estimation in the context of a monostatic array.

## 6.2 Recommendations for Future Work

The micro-Doppler method should be investigated in greater detail as a means by which to provide target detection and macro velocity estimation capabilities to a nearly-stationary sonar system. Simulations and experiments which may provide useful tools in the analysis of this method would introduce a moving target at some range, and would then characterize the performance of the estimator in determining target location and velocity. An investigation into the feasibility of using the micro-Doppler method for simultaneous target detection, macro-velocity estimation, and target classification should also be conducted.

A theoretical investigation into N-point velocity estimation should be conducted as well. At present, the existing theory is built upon the foundation of two-point velocity estimation, but N-point estimation may provide a superior means by which to estimate target velocity. Theoretical work in this area could include the development of the  $N \times N$  covariance matrix for velocity estimates from a moving range-spread target, and the subsequent calculation of the Cramer-Rao bounds for velocity estimators.

## Appendix A

### List of Symbols

Symbols Commonly Used in the Thesis	
Symbol	Description
$\tilde{A}$	complex amplitude of scatterer
$BW$	bandwidth
$\tilde{b}$	complex Gaussian random variable modeling reflection from a point target
$\tilde{b}(\lambda)$	complex Gaussian process modeling reflection from a range-spread target
$CRLB$	Cramer-Rao lower bound
$c$	speed of sound in water
$d, \vec{d}, \mathbf{d}$	subsequent state(s)/observation(s) of system
$E_t$	transmitted energy
$E\{x\}$	ensemble expectation of $x$
$\tilde{f}$	envelope function
$f$	frequency
$f_0$	transmitted frequency
$f'$	Doppler-shifted frequency
$f_c$	carrier frequency
$f_s$	sampling frequency
$G$	functional relationship between CRLBs
$\hat{\gamma}$	phase shift estimate
$h[kT_k]$	impulse response of linear filter
$\mathbf{J}$	Fisher information matrix

Symbols Commonly Used in the Thesis, Cont.	
Symbol	Description
$j$	$\sqrt{-1}$
$K_{\tilde{s}_1\tilde{s}_2}(kT_k)$	covariance of signals $\tilde{s}_1$ and $\tilde{s}_2$ , expressed as a function of lag $kT_k$
$k$	lag of the covariance function
$k_0$	optimal lag for velocity estimation
$k_p$	pulse length in carrier cycles
$k_s$	dead time separating two pulses, expressed in carrier cycles
$L$	time-location of target
$\lambda$	wavelength of carrier
$\tilde{N}$	uncorrelated signal component
$N$	number of independent snapshots
$N_0$	thermal noise level
$\tilde{n}$	additive white Gaussian noise (thermal noise term)
$P_t$	transmitted power
$p$	filter width
$\phi$	arrival angle of signal
$R$	range
$RMSE$	root mean-square error
$\hat{\rho}$	linear prediction estimate of weight $\hat{w}$ amplitude
$\rho$	correlation coefficient
$\rho_c$	coherent correlation coefficient
$\rho_{c,a}$	coherent correlation coefficient, autocovariance
$\rho_{c,c}$	coherent correlation coefficient, cross covariance
$\rho_e$	effective correlation coefficient
$\rho_n$	correlation coefficient associated with thermal noise
$S_R(\lambda)$	range-scattering function
$SNR$	signal-to-noise ratio, expressed in dB
$snr$	signal-to-noise power ratio (unitless)
$\tilde{s}(t)$	complex signal
$\sigma^2$	variance
$T_k$	sampling period

Symbols Commonly Used in the Thesis, Cont.	
Symbol	Description
$T_p$	time between pings
$T_s$	period of the carrier
$t$	time
$\tau$	two-way travel time of signal
$\theta$	transducer tilt angle
$\hat{v}$	velocity estimate
$v$	velocity
$\hat{w}$	linear prediction estimate of $w$
$w$	linear prediction weight which transforms $x$ into $d$
$w_c$	carrier angular frequency
$w_D$	Doppler angular frequency
$x, \vec{x}, \mathbf{x}$	initial state(s)/observation(s) of system

# Bibliography

- [1] Z. Banjanin, J.R. Cruz, and D.S. Zrnic. Linear prediction approach to doppler estimation of radar signals in the presence of ground clutter. In *Acoustics, Speech, and Signal Processing. ICASSP Conference Proceedings*, volume 4, pages 2361–2364, May 1989.
- [2] Z. Banjanin, D.S. Zrinc, and J.R. Cruz. A linear prediction approach to doppler mean frequency retrieval in the presence of ground clutter. *IEEE Transactions on Aerospace and Electronic Systems*, 29(3):1050–1058, 1993.
- [3] John S. Bird and Geoff K. Mullins. Analysis of swath bathymetry sonar accuracy. *IEEE Journal of Oceanic Engineering*, 30(2):372–390, 2005.
- [4] J.S. Bird. Signal processing for masb sonar: Technology transfer document. October 2007.
- [5] S.E. Bradley, K.L. Deines, and F.D. Rowe. Acoustic correlation current profiler. *IEEE Journal of Oceanic Engineering*, 16(4):408–414, 1991.
- [6] B.H. Brumley, R.G. Cabrera, K.L. Deines, and E.A. Terray. Performance of a broad-band acoustic doppler current profiler. *IEEE Journal of Oceanic Engineering*, 16(4):402–407, 1991.
- [7] William S. Burdic. *Underwater Acoustic System Analysis*. Prentice Hall Signal Processing Series. Prentice Hall: New Jersey, second edition, 1991.
- [8] L.W. Couch II. *Digital and Analog Communication Systems*. Macmillan Publishing Company: New York, 1987.
- [9] K.L. et al. Deines. Bottom tracking system. In *U.S. Patent 5122990*.
- [10] Philip N. Denbigh. Swath bathymetry: Principles of operation and an analysis of errors. *IEEE Journal of Oceanic Engineering*, 14(4):289–298, 1989.
- [11] Kraeutner et al. Imaging methods and apparatus using model-based array signal processing. In *U.S. Patent 6130641*.
- [12] G. Griffiths, S.E. Bradley, G. Watson, and B. Dupee. An acoustic correlation sonar for vertical profiling of ocean currents to a range of 1 km.

- [13] A.E. Hay and J. Sheng. Vertical profiles of suspended sand concentration and size from multifrequency acoustic backscatter. *J. Geophys. Res.*, 97:15,661–15,677, 1992.
- [14] A.E. Hay, L. Zedel, R. Craig, and W. Paul. Multi-frequency, pulse-to-pulse coherent doppler sonar profiler. In *Proc. IEEE/OES/CMTC 9th Working Conf. on Current Measurement Tech.*, pages 25–29, 2008.
- [15] P.H. Kraeutner and J.S. Bird. Principle components array processing for swath acoustic mapping. In *OCEANS '97. MTS/IEEE Conference Proceedings*, volume 2, pages 815–819, October 1997.
- [16] B.R. Mahafza. *Radar Systems Analysis and Design Using MATLAB*. Chapman and Hall/CRC: Florida, 2005.
- [17] R.L. Mitchell. *Radar Signal Simulation*. Artech House: Massachusetts, 1976.
- [18] Athanasios Papoulis and S. Unnikrishna Pilai. *Probability, Random Variables and Stochastic Processes*. McGraw-Hill Series in Electrical and Computer Engineering. McGraw Hill: New York, fourth edition, 2002.
- [19] M.A. Richards. *Fundamentals of Radar Signal Processing*. McGraw-Hill: New York, 2005.
- [20] Ali H. Sayed. *Fundamentals of Adaptive Filtering*. John Wiley and Sons, Inc.: New Jersey, 2003.
- [21] C. Smyth, L. Zedel, and A.E. Hay. Coherent doppler profiler measurements of near-bed suspended sediment fluxes and the influence of bed forms. *J. Geophys. Res.*, 107, 2002.
- [22] T. Thayaparan, S. Abrol, E. Riseborough, L. Stankovic, D. Lamothe, and G. Duff. Analysis of radra micro-doppler signatures from experimental helicopter and human data. *IET Radar Sonar Navig.*, 1(4):289–299, 2007.
- [23] K.B. Theriault. Incoherent multibeam doppler current profiler performance: Part i-estimate variance. *IEEE J. Ocean. Eng.*, 11(1), 1986.
- [24] Paul A. Tipler. *Physics for Scientists and Engineers*, volume 1. W.H. Freeman and Company: New York, 4 edition, 1999.
- [25] H.L. Van Trees. *Detection, Estimation, and Modulation Theory, Part III: Radar-Sonar Signal Processing and Gaussian Signals in Noise*. John Wiley and Sons, Inc: New York, 2001.
- [26] H.L. Van Trees. *Detection, Estimation, and Modulation Theory, Part IV: Optimum Array Processing*. John Wiley and Sons, Inc: New York, 2002.

- [27] L. Zedel, R. Cabrera, A. Lohrmann, and A. Hay. Single beam, high resolution pulse-to-pulse coherent doppler profiler. In *Proc. IEEE 5th Working Conf. on Current Measurement*, pages 199–204, 1995.
- [28] L. Zedel and A.E. Hay. A coherent doppler profiler for high-resolution particle velocimetry in the ocean: laboratory measurements of turbulence and particle flux. *IEEE J. Atmos. Ocean Technol.*, 16:1102–1117, 1996.
- [29] L. Zedel and A.E. Hay. A three-component bistatic coherent doppler velocity profiler: error sensitivity and system accuracy. *IEEE J. Ocean. Eng.*, 27(3), 2002.
- [30] L. Zedel, A.E. Hay, R. Cabrera, and A. Lohrmann. Performance of a single-beam pulse-to-pulse coherent doppler profiler. *IEEE Journal of Oceanic Engineering*, 21(3):290–297, 1996.
- [31] D.S. Zrinc. Estimation of spectral moments for weather echoes. *IEEE Transactions on Geoscience Electronics*, 17(4):113–128, 1979.